

CHEMICAL REACTION MODELING IN A SUBSURFACE FLOW
SIMULATOR WITH APPLICATION TO IN-SITU UPGRADING
AND CO₂ MINERALIZATION

A DISSERTATION
SUBMITTED TO THE
DEPARTMENT OF ENERGY RESOURCES ENGINEERING
AND THE COMMITTEE ON GRADUATE STUDIES
OF STANFORD UNIVERSITY
IN PARTIAL FULFILLMENT OF THE REQUIREMENTS
FOR THE DEGREE OF
DOCTOR OF PHILOSOPHY

Yaqing Fan
May 2010

© Copyright by Yaqing Fan 2010
All Rights Reserved

I certify that I have read this dissertation and that, in my opinion, it is fully adequate in scope and quality as a dissertation for the degree of Doctor of Philosophy.

(Louis J. Durlofsky) Principal Co-Adviser

I certify that I have read this dissertation and that, in my opinion, it is fully adequate in scope and quality as a dissertation for the degree of Doctor of Philosophy.

(Hamdi A. Tchelepi) Principal Co-Adviser

I certify that I have read this dissertation and that, in my opinion, it is fully adequate in scope and quality as a dissertation for the degree of Doctor of Philosophy.

(Anthony R. Kavscek)

Approved for the University Committee on Graduate Studies.

Abstract

Chemical reactions occur in a number of subsurface flow processes. Numerical modeling is an essential tool for understanding and optimizing complex reactive flows in a variety of application areas. In this work, we propose and implement chemical reaction modeling capabilities in Stanford’s General Purpose Research Simulator (GPRS). The formulations developed include a procedure based on species conservation equations and an approach based on element conservation equations. The species-based formulation is suitable for solving reactive flow problems characterized by kinetic reactions only. In the element-based formulation, by contrast, both equilibrium and kinetic reactions can be treated consistently in the fully coupled system. This procedure represents a new treatment for reactive flow modeling. Additionally, in both formulations, a new generic representation of reaction terms is developed, which allows simultaneous modeling of homogeneous and heterogeneous reactions within or among phases (i.e., gas, liquid, water and solid phases).

We apply the species-based formulation to model the in-situ upgrading of oil shale. Oil shale is a highly abundant but difficult to produce energy resource. The in-situ upgrading process entails heating the oil shale to about 700 °F, at which point the kerogens decompose to gas and liquid hydrocarbons through a series of chemical reactions. After adjusting a few uncertain parameters (within physical ranges), our

simulation results show relatively close agreement with available field data. The other application considered in this work is the modeling of carbon storage in deep saline aquifers. Detailed results are presented for a fine-grid model of a benchmark study. For this case, chemical reactions are not considered. Carbon mineralization reactions are then modeled using the element-based reactive flow formulation. Coarse-grid models are used for these simulations. Because the chemistry data relevant to carbon mineralization are, to date, not fully defined, we provide simulation results using available chemistry parameters. We discuss the remaining challenges that must be overcome before mineralization reactions can be simulated on fine-grid models. We note finally that the chemical reaction modeling capabilities in GPRS can be extended to other subsurface reactive flow processes (e.g., enhanced coalbed methane recovery).

Acknowledgements

I would like to express my sincere and deepest gratitude to my advisors Professor Louis J. Durlofsky and Professor Hamdi A. Tchelepi for their guidance and support during my work. I feel it a privilege to be co-advised by them. Throughout my research, over more than five years, they have been very knowledgeable and available to discuss issues from the high-level planning all the way to the specific model characterizations. I really appreciate their help in guiding me in my both Master's and PhD programs, for attending to all of the details, and for encouraging me to keep exploring.

I would like to thank the other members of my committee. Professor Andrew Spakowitz from the Chemical Engineering Department attended my proposal two years ago and kindly chaired my oral defense this year. I would like to also thank Professor Anthony R. Kavscek for reading my thesis. I am grateful to Professor Tapan Mukerji for being my defense committee member. Finally, I would also like to thank Professor Khalid Aziz, who has provided valuable comments in my research and also supported me in some of my work with the Society of Petroleum Engineers.

I would also like to extend my thanks to all of the faculty, staff and students in the Department of Energy Resources Engineering. I am especially grateful to Dr.

Huanquan Pan, who manages the simulator GPRS and was always ready to answer research questions. My work could not have been done without his help. I also thank Professor Adam Brandt for valuable suggestions and for pointing me to useful references. I am also grateful to Karyn Borella for setting up my oral defense. Thanks are also due to former and current graduate students, specially to Jianbing Wu, who helped me a lot in my first few years. With them, my work and life at Stanford has been colorful and truly rewarding.

Financial support from the Stanford University Petroleum Research Institute Program on Reservoir Simulation (SUPRI-B) and from Stanford’s Global Climate and Energy Project (GCEP) is gratefully acknowledged. I also would like to express thanks to Dr. Long Nghiem from the Computer Modelling Group who provided some of the chemical reaction data used in this thesis.

Special thanks are due to my wife Ying Cao and to my parents. Their love and support are the very momentum for my work. Their living with me in the last months as I am writing this thesis truly freed me from many concerns.

Contents

Abstract	iv
Acknowledgements	vi
1 Introduction and Literature Review	1
1.1 Reactive transport modeling	2
1.1.1 General overview of reactive-transport simulators	2
1.1.2 Species-based reactive-transport formulation	6
1.1.3 Element-based formulation	8
1.1.4 Decoupling of the governing equations	10
1.1.5 Scope of this work	12
1.2 In-situ upgrading modeling	13
1.3 Modeling geologic carbon sequestration	16
1.4 Dissertation outline	19
2 Chemical Reaction Modeling	21
2.1 Governing equations and numerical formulation	22
2.1.1 Species and element conservation equations	23
2.1.2 Reaction characterization	28

2.1.3	Phase equilibrium calculation	32
2.1.4	Summary of governing equations	33
2.2	Generalized reaction implementation	34
2.2.1	Generic nonlinear reaction terms	35
2.2.2	Concentration type reaction	36
2.2.3	Activity type reactions	38
2.3	Numerical solution techniques	41
2.3.1	Application of Newton’s method	41
2.3.2	Reduction of the problem size	43
2.3.3	Solution strategies	52
2.3.4	Computational complexity of coupled and decoupled formulations	53
2.4	Numerical examples	55
2.4.1	Kinetic versus equilibrium reactions	55
2.4.2	Application to carbon mineralization	58
2.5	Concluding remarks	70
3	Modeling the In-situ Upgrading	72
3.1	Modeling techniques	73
3.1.1	Mass and energy balance equations	73
3.1.2	Phase equilibrium and properties	75
3.1.3	Kinetic reactions	76
3.1.4	Reaction stoichiometry	77
3.1.5	Heat injection	79
3.1.6	Solution method	80
3.2	Modeling the MDP-S project	81

3.2.1	Mahogany Demonstration Project-South	82
3.2.2	Description of MDP-S model	82
3.2.3	Model components, reactions and other parameters	85
3.2.4	Simulation results	92
3.3	Sensitivity analysis	95
3.3.1	Temperature effect	97
3.3.2	Heater pattern effect	99
3.3.3	Heater spacing effect	101
3.3.4	Energy ratios for the various scenarios	103
3.4	Concluding remarks	105
4	Modeling Carbon Storage	107
4.1	Modeling techniques	108
4.1.1	EOS based compositional simulation	108
4.1.2	Hysteresis models	110
4.1.3	Geochemical modeling	112
4.2	Geochemical model verification	113
4.3	Simulation results of a benchmark case	115
4.3.1	Model description	116
4.3.2	Fine-grid results without geochemistry	119
4.3.3	Coarse-grid results with carbon mineralization	121
4.4	Concluding remarks	128
5	Conclusions and Future Work	130
5.1	Summary and conclusions	130

5.2 Recommendations for future work	131
Bibliography	140

List of Tables

1.1	Species and element-based formulations implemented in GPRS	13
2.1	Summary of governing equations	34
2.2	Primary and secondary equations for the two approaches	45
2.3	Chemical reactions for CO ₂ mineralization	61
2.4	Mineral formula, precipitation and dissolution parameters	61
2.5	Performance summary for carbon mineralization base case runs . . .	66
2.6	Final carbon distribution in various phases at 500 years	70
2.7	Impact of mineral selection on simulator performance	71
3.1	Example of stoichiometric coefficient input	79
3.2	Suggested values for time step control parameters	82
3.3	Kinetic reactions in MDP-S case (adapted from [64])	87
3.4	Compositions and properties – Green River oil shale pyrolysis components (from [7])	88
3.5	Green River oil shale pyrolysis components and lumped components .	89
3.6	Interaction coefficients for components	89
3.7	Enthalpy coefficients for components	89
3.8	Summary of input parameters used in MDP-S model	90

3.9	Energy ratios for the sensitivity study cases (at 90% recovery efficiency)	105
4.1	Properties of CO ₂ and H ₂ O for equation of state (EOS) calculations .	109
4.2	B-dot model parameters from the EQ3/6 database [67]	112
4.3	Summary of input parameters for the verification case	114
4.4	Input parameters for each ion for the verification case	114
4.5	Summary of input parameters for benchmark model	118
4.6	Chemical reactions for CO ₂ mineralization in the benchmark study .	123

List of Figures

1.1	Simplified flow chart of TOUGHREACT program (adapted from [71]).	4
2.1	Dimensionless component concentrations for different values of Da .	31
2.2	Flow chart for the solution of the fully coupled multiphase flow and reactive problems.	42
2.3	Illustration of one connection involving blocks a and b and one interface.	47
2.4	$\text{CO}_2(\text{g})$ and $\text{CO}_2(\text{s})$ variation with time for different runs. Lines with symbols are results if the reaction (2.86) is modeled as an equilibrium reaction. Lines without symbols are the cases when (2.86) is modeled as a kinetic reaction.	58
2.5	Time step sizes and cumulative Newton iterations for various runs.	59
2.6	Total CPU time for various runs with BILU(0) preconditioners. Total CPU time plotted is the sum of linear solver time, Jacobian construction time, and property calculation time. Actual total CPU time includes overhead due to input and output.	64

2.7	CPU time breakdown for 500 year runs with CPR preconditioner. Total CPU time plotted is the sum of solver time, Jacobian construction time, and property calculation time. Actual total CPU time includes overhead due to input and output.	65
2.8	Gas saturations and dissolved CO ₂ mole fractions in aqueous phase at 5 and 500 years.	67
2.9	Selected mineral molar density changes at 500 years (mol/m ³). Positive values indicate precipitation, and negative values indicate dissolution.	67
2.10	Mineral net molar changes and evolution of CO ₂ in time.	68
2.11	CO ₂ evolution in time.	70
3.1	Model area for Mahogany Demonstration Project-South.	85
3.2	Heater positions and gridding of the simulation model for Mahogany Demonstration Project-South.	86
3.3	Hydrocarbon production results for the MDP-S project. Solid lines are simulation results from our model. Symbols are MDP-S field test results from [62].	93
3.4	Cross-sectional view of temperature (°F) at 500 days (region between CC' in Figure 3.1(b) shown).	94
3.5	Temperature (°F) for MDP-S simulation over region BB' (shown in Figure 3.1(b)).	95
3.6	Remaining kerogen (lbmol/ft ³) for MDP-S simulation over region BB'	95
3.7	Oil saturation for MDP-S simulation over region BB'	96
3.8	Hydrocarbon component production rates from MDP-S model.	96
3.9	Top view of heaters and producers for sensitivity analysis.	97

3.10	Temperature variation for repeated hexagon pattern (heater temperature is 700 °F, heater spacing is 8 ft). This model represents the base case.	98
3.11	Temperature variation for repeated hexagon pattern (heater temperature is 650 °F, heater spacing is 8 ft).	98
3.12	Temperature variation for repeated hexagon pattern (heater temperature is 600 °F, heater spacing is 8 ft).	99
3.13	Effect of heater temperature on hydrocarbon production.	99
3.14	Temperature variation for repeated square pattern (heater temperature is 700 °F, heater spacing is 13 ft).	100
3.15	Temperature variation for repeated triangle pattern (heater temperature is 700 °F, heater spacing is 20 ft).	101
3.16	Effect of heating pattern on hydrocarbon production.	101
3.17	Temperature variation for repeated hexagon pattern (heater temperature is 700 °F, heater spacing is 10 ft).	102
3.18	Temperature variation for repeated hexagon pattern (heater temperature is 700 °F, heater spacing is 12 ft).	102
3.19	Effect of heater spacing on hydrocarbon production.	103
4.1	Illustration of gas-brine relative permeabilities and residual trapping.	111
4.2	Comparison of ion molalities (mol/kg) from GPRS and GEM-GHG for 1-D case at 50 days. Symbols represent GPRS results, lines represent GEM-GHG results.	115

4.3	Comparison of mineral changes (mol/m^3) from GPRS and GEM-GHG for 1-D case at 50 days. Symbols represent GPRS results, lines repre- sent GEM-GHG results.	116
4.4	Schematic of model adapted from [14].	118
4.5	Gas phase saturation variation over time for the benchmark model. .	119
4.6	Residually trapped gas over time.	120
4.7	Solubility trapping of CO_2 . Values shown are molar fraction of dis- solved CO_2 in the aqueous phase.	121
4.8	Aqueous phase density (g/cm^3) variation with time.	122
4.9	Carbon distribution in the fine-grid model of the benchmark study. .	122
4.10	Evolution of the molar density change (mol/m^3) of anorthite in the coarse-grid model.	124
4.11	Evolution of the molar density change (mol/m^3) for calcite in the coarse-grid model.	124
4.12	Evolution of the molar density change (mol/m^3) for kaolinite in the coarse-grid model.	125
4.13	Distribution of injected carbon CO_2 over time.	126

Chapter 1

Introduction and Literature Review

A wide variety of chemical reactions take place between fluids and minerals in reservoirs. In a number of subsurface processes, such as the in-situ upgrading of oil shale and the long term geologic storage of carbon, chemical reactions are among the key physical effects. Reservoir simulation can be used to understand these coupled flow and reaction processes. Eventually, it may also be used to assess the uncertainty and optimize subsurface flow processes that involve chemical reactions.

Chemical reactions occur among species. Simulation of the coupled reactive flow processes requires simultaneous modeling of the transport and reactions of each species of interest. In multiphase flow problems, the phase behavior may also be tightly coupled with the transport and reactions. These aspects together lead to systems involving multiple nonlinear equations that must be solved for each grid block. Our goal in this work is to solve the flow (including phase behavior) and reactions in a fully coupled manner. This will result in formulations that are more robust than

those that apply iterative coupling.

1.1 Reactive transport modeling

1.1.1 General overview of reactive-transport simulators

The numerical simulation of coupled subsurface flow and chemical reactions has been an active area in the hydrology community, and a number of formulations have been implemented into hydrological codes. In recent years, there has been growing interest in this area within the reservoir simulation community, in part because of the application of chemical methods for hydrocarbon extraction and also as a result of research on geological carbon sequestration. We now discuss the recent efforts from both communities.

In the hydrology applications, numerous efforts have been directed toward in modeling coupled water flow and (bio)geochemical reactions. Tebes-Stevens *et al.* [60] simulated coupled biogeochemical reactions with steady-state groundwater flow using FEREACT. Steefel *et al.* [57] developed a model for reactive flow with kinetic precipitation and dissolution in single-phase hydrologic systems. Recently, Steefel *et al.* [59] developed CrunchFlow, a software package that models multicomponent reactive flow problems in groundwater systems. In a recent paper, Yeh *et al.* [72] described the evolution of HYDROGEOCHEM (also named LEHGC), a software package that currently includes thermal effects in the coupled groundwater flow and biogeochemical problems. TOUGHREACT [70, 71] is another well known reactive-transport simulator developed and constantly updated by Lawrence Berkeley National Laboratory. Interactions between gas, minerals, and water are modeled. Other code packages

featuring reactive-transport capabilities include, but not are limited to, GWB [4], MIN3P [35], NUFT [44] and RETRASO [56].

The codes noted above can be roughly divided into two groups based on their solution approach. In the first group of simulators, the transport and reactions are solved iteratively. This approach is referred to as the sequential iterative approach (SIA). To exemplify this treatment, a simplified flow chart of TOUGHREACT [71] is shown in Figure 1.1. At each time step, the flow equation (without reaction terms) is solved first. With the updated phase velocities and mole fractions, the chemical submodel is called to update the concentrations block by block. Some other simulators apply a similar approach, such as FERREACT [60], HYDROGEOCHEM [72], and GWB [4]. This sequentially coupled reaction-transport formulation can provide accurate results for many problems. However, the nested chemical reaction calculation that must be performed at each time step may result in large computational times for complex models. Additionally, the SIA method may be numerically unstable and the iterative procedure may display convergence problems in some cases [58].

The second group of simulators substitute the chemical reactions into the transport equations and solve the full system simultaneously. This approach is often referred to as the direct substitution approach (DSA) or global implicit approach (GIA). The GIA method is believed to be more numerically stable than the SIA method. However, it requires much more computational resources per time step than SIA. In fact, because it is very memory intensive, the GIA method has not been applied as widely as the SIA method [58]. A recently developed simulator that uses GIA is RETROSO [56], which can simulate gas-water-mineral systems with both kinetic and equilibrium reactions.

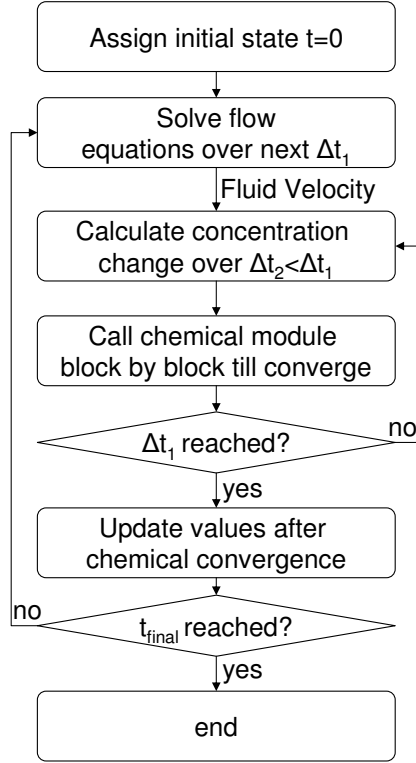


Figure 1.1: Simplified flow chart of TOUGHREACT program (adapted from [71]).

Reactive-transport simulation in hydrologic systems has evolved into a relatively mature set of techniques for modeling a variety of subsurface phenomena. However, most of these developments not directly applicable to oil production because they do not treat hydrocarbons. For example, the complex phase behavior of mixed hydrocarbon systems is not addressed in these simulators.

Chemical reaction modeling in the context of oil reservoir simulation has been studied by several research groups in recent years. Two representative simulators are STARS [37] and ECLIPSE 300 [21]. STARS is a K-value based (in contrast to

equation of state-based) thermal-compositional simulator developed by the Computer Modelling Group. ECLIPSE 300 is another equation of state-based compositional simulator developed by Schlumberger. The Computer Modelling Group is also developing chemical reaction modeling capabilities in another simulator, GEM, which is based on generalized equations of state. Extensions were introduced to model the chemical reactions related to asphaltene precipitation and greenhouse gas (GHG) sequestration. Specifically, Nghiem *et al.* [43] enhanced GEM to include mineral dissolution and precipitation kinetics. UTCHEM [39], a simulator developed at The University of Texas at Austin, includes reactive-transport with chemical and biological reactions. Recently, the same group added some chemical flooding capabilities (e.g., surfactant phase behavior) to a fully coupled equation-of-state compositional simulator GPAS [27].

In the reservoir simulators mentioned above, only UTCHEM applies a sequential iterative approach. The other simulators solve the fully coupled system simultaneously. In STARS, ECLIPSE 300 and GEM, various implicit schemes can be used. UTCHEM has a relatively complete treatment of chemical reactions in multiphase flow. It is, however, expected to have the same drawbacks as the SIA method described above. The other simulators, by contrast, do not have comprehensive chemical reaction modeling implementations. Specifically, only kinetic reactions can be modeled by STARS and ECLIPSE 300. GEM treats all of the aqueous phase reactions as equilibrium reactions and all of the mineral reactions as kinetic reactions. GEM does not model chemical reactions involving hydrocarbons. Thus a fully general GIA implementation does not yet exist.

In summary, hydro-geochemical simulators typically do not model hydrocarbons.

The equation-of-state compositional simulators designed for reservoir simulation have limited capabilities in modeling chemical reactions. There is thus a need to develop a unified formulation that provides a general treatment of chemical reactions within an equation-of-state compositional simulation framework. Additionally, the GIA method is preferred over the SIA method in order to gain better numerical stability. Our proposed method, described in the next section, will address these issues.

1.1.2 Species-based reactive-transport formulation

To gain insight into previous reactive-transport simulators, and to understand their limitations, we now discuss the model formulations in some detail. We first consider the species mass balance equation, which represents the basis of all of the simulators mentioned above. The mass balance equation for a species i over a grid block is represented as follows:

$$F_i = \frac{\partial N_i}{\partial t} + L_i - \left(\sum_{k=1}^{n_k} \nu_{i,k} r_k + \sum_{q=n_k+1}^{n_r} \nu_{i,q} r_q \right) = 0, \quad (1.1)$$

where $\partial N_i / \partial t$ is the accumulation term, L_i is the flow term, $\nu_{i,k}$ is the stoichiometric coefficient of species i in kinetic reaction k , $\nu_{i,q}$ is the stoichiometric coefficient of species i in equilibrium reaction q , r_k is the rate of the kinetic reaction k , r_q is the rate of the equilibrium reaction q , n_k is the number of kinetic reactions, n_r is the total number of reactions, and F_i is the residual that we seek to drive to zero (these terms will be discussed in full detail in Chapter 2). From the modeling point of view, chemical reactions can be divided into two classes, specifically, equilibrium reactions and kinetic reactions [17], which is why the reaction source terms are written in two separate parts. By conventions we define equilibrium reactions as chemical reactions

that are sufficiently fast and reversible, and kinetic reactions as those that are slow or irreversible.

All of the simulators discussed in Section 1.1.1 are based on species balance equations equivalent to (1.1). The accumulation and flux terms are essentially the same for the various simulators. However, the treatments of the reaction terms are different. We now discuss the treatments of r_k and r_q in detail. The discussion below holds for both SIA and GIA methods, and for both groundwater and oil reservoir applications.

If the reactions considered are all kinetic reactions, a rate equation can be formulated for each reaction. Each reaction rate r_k can be expressed explicitly as a function of the unknown variables. Substituting the reaction rates prescribed by specific rate laws into (1.1) eliminates r_k and thus does not incur additional unknowns. If there are equilibrium reactions in the system, the term r_q must be addressed. In contrast to kinetic rates, the equilibrium reaction is typically expressed by an algebraic equation. There is not an explicit function for equilibrium reaction rates. It is possible to treat each equilibrium reaction rate as an additional unknown and add the algebraic equation to the governing equation set. This method incurs additional and unnecessary computational complexity, as the equations can become difficult to solve due to the fast equilibrium reaction rates [34].

In hydrogeochemical applications, the concept of a “component” not only eliminates equilibrium reaction rates in the aqueous phase, but also reduces the number of conservation equations to be solved. Nearly all hydrologic simulators apply this or an equivalent approach. A component is a linear combination of species not affected by intra-aqueous equilibrium reactions [41]. For example, if M_1 is in equilibrium with

M_2 , then $M_1 + M_2$ is considered as a component (note this “component” is different than the definition of component used in reservoir simulation). A conservation equation is then written for the component $M_1 + M_2$ [41]. If there are n_{qa} intra-aqueous equilibrium reactions in the system, the number of conservation equations can be reduced by n_{qa} . The intra-equilibrium rates do not appear in the new equations. The simulator GEM applies a very similar approach referred to as equilibrium rate annihilation (ERA) [42]. Using the component concept to reduce the number of conservation equations is, however, difficult to apply in a complex multiphase (e.g., gas-water-mineral) system with various cross-phase equilibrium reactions. In the next section, we propose an element-based formulation that treats r_k and r_q in the same manner regardless of whether the reaction is homogeneous or heterogeneous.

1.1.3 Element-based formulation

In contrast to the simulators discussed above, we formulate the problem based on elements. The potential use of elements as the basis for defining chemical systems and for conservation equations has been noted previously (e.g., [4], [56]), though extensive development or implementation within the context of multiphase flow simulations has not, to our knowledge, been reported. Instead of solving the species conservation equations in (1.1), we solve the conservation equations for each element:

$$F_e = \frac{\partial N_e}{\partial t} + L_e = 0, \quad (1.2)$$

where F_e , $\partial N_e / \partial t$ and L_e are the residual term, accumulation term and flux term of element e , respectively. Equation (1.2) states that the total mass of element e over the modeling domain is conserved. This is true regardless of whether the reactions are

equilibrium or kinetic. The advantage of element balances over species balances is due to the fact that the reaction terms r_k and r_q do not appear in the element conservation equations. Because the total mass of element e is summed over all phases and all species, we do not need special treatments for heterogeneous equilibrium reactions (e.g., gas-water, gas-rock, or water-rock equilibrium reactions).

Within the element-balance context, the set of governing equations is closed by adding n_r reaction relations. For kinetic reactions, these relations are characterized by differential equations. For equilibrium reactions, the reaction relations are algebraic. In order to model a wide range of chemical reactions, a novel generic representation of chemical reaction terms is developed, which allows us to define homogeneous and heterogeneous reactions in a consistent manner. The characterization of different types of reactions will be described in detail in Chapter 2.

In cases when the elements in the system are not balanced (e.g., some of the elements are not of interest and thus not tracked), we use species conservation equations. We note that, in such cases, the limitations that arises as a result of the treatment of r_q (described earlier) apply.

In this work, we implement both element and species-based formulations within Stanford’s General Purpose Research Simulator (GPRS). GPRS was initially developed by Cao [10] in the Department of Petroleum Engineering at Stanford University and was further extended by Jiang [26]. Because of the special treatment required for r_q in the species-based formulation, we will not incorporate equilibrium reactions in our species-based formulation. The element-based formulation, by contrast, has a complete treatment of kinetic and equilibrium reactions. The chemical reaction modeling capability is compatible with most of the advanced features in GPRS (e.g.,

fully compositional simulation, unstructured model, CPR preconditioned GMRES solver). We apply a fully implicit method (equivalent to the GIA method) for both the element and species-based formulations in GPRS.

1.1.4 Decoupling of the governing equations

We now discuss procedure for problem size reduction in the reactive-transport formulation. The full set of nonlinear governing equations include (species or element) conservation equations, reaction relations, and phase equilibrium relations. The system is solved using Newton's method. Simultaneous solution of these equations (in the GIA method) is generally CPU and memory intensive. Properly decoupling them can reduce the number of equations to be solved simultaneously. The reduced set of equations is referred to as the set of primary equations.

In compositional reservoir simulation, the phase equilibrium relations can be decoupled from the set of governing equations under the local equilibrium assumption [10]. At the implementation level, this decoupling is equivalent to building a Schur complement to the Jacobian matrix (the Jacobian is required for the Newton's method). Because the decoupling of the phase equilibrium relations is readily accomplished, nearly all compositional reservoir simulators adopt this (or an equivalent) procedure. Applying only this decoupling, the number of primary variables in each block is equal to n_c , where n_c is the number of species (including n_f fluid species and n_s solid species). For a problem with n_c species and n_b grid blocks, the size of the linear system that must be solved is $n_c n_b \times n_c n_b$ (note that the total number of unknowns is $n_f n_p + 2n_p + n_s$, and the numbers of primary and secondary unknowns are n_c and $n_f(n_p - 1) + 2n_p$, respectively, where n_p is the number of fluid phases).

In hydrogeochemical simulators, because full hydrocarbon phase behavior is not generally modeled, there have been a number of other approaches suggested for decoupling. We now describe a recent and representative scheme. Molins *et al.* [41] proposed an advanced decoupling scheme for reactive-transport problems. In [41], the decoupling is based on component matrices in a water-rock system. Through algebraic considerations, the authors proved the existence of a formulation in which the number of coupled nonlinear equations is $n_c - n_q - n_{ki}$, where n_q is the number of equilibrium reactions and n_{ki} is the number of kinetic reactions involving one immobile (solid) species. The method proposed in [41] is an effective decoupling approach that can reduce the number of primary components. This approach is not, however, directly applicable for our formulation. This is because the method assumes that each kinetic reaction with minerals only involves one mineral. Thus reactions involving more than one solid are not considered. In addition, the method emphasizes mobile species and only solves fluid conservation equations. For cases in which we are interested in both fluid and solid concentrations, this approach may not be suitable. Furthermore, the complex component matrices introduced in [41] may be very difficult to implement for multiphase systems (note that in [41] a full implementation is not presented).

In this work, we propose a two-step decoupling scheme. The first step is to decouple the phase equilibrium relations. This step follows the same procedure as in most compositional simulators, and is applied for both species and element-based formulations GPRS. In the second step, we decouple all the localized reaction relations from the conservation equations. This decoupling, described below, proceeds very naturally with the element-based formulation.

The second decoupling is based on the nature of each reaction. In the element-based formulation, the conservation equations do not have any reaction terms, and each reaction is described by a separate equation. If the reaction is a localized reaction (either an equilibrium reaction or a kinetic reaction involving minerals), the equation describing this reaction does not have a flux term. As a result, this equation can be mathematically decoupled from the element conservation equations. If, however, the reaction is a kinetic reaction that involves purely fluid (i.e., flowing) species, the equation describing it will have a flux term. In this case, this equation must be solved along with the conservation equations. We denote n_{ks} to be the number of kinetic reactions involving minerals, and n_{kf} to be the number of kinetic reactions involving purely fluid species. Applying this decoupling, the number of primary equations becomes $n_c - n_q - n_{ks}$. We note that, if every mineral kinetic reaction involves only one mineral, this decoupling yields the same number of primary variables as in [41]. In the species-based formulation, if all reactions are kinetic, the number of primary equations after the second decoupling is $n_c - n_{ks}$.

Finally, it is worth noting that the procedure to decouple the localized reactions incurs extra CPU cost. However, because $n_c - n_q - n_{ks}$ can be much smaller than n_c in complex problems, the reduction in linear solution time more than compensate for the extra time used in the decoupling.

1.1.5 Scope of this work

Table 1.1 summarizes the various treatments described above and indicates the methods that have been implemented in GPRS in this work. There are two types of formulations available when modeling a specific problem. If the reactions in the system

are all kinetic reactions, we can apply either the species or element-based formulation. If the elements in these reactions are not balanced, however, we must apply the species-based formulation. If there are both kinetic reactions and equilibrium reactions, then the element-based formulation should be used. In this case, we assume all of the elements are balanced. It is possible to formulate an element-based approach, though it is not considered here. In both the species and element-based approaches, the phase equilibrium relations are decoupled from the conservation equations. The localized reaction relations can also be decoupled.

We apply both the species and element-based formulations to model problems of practical interest. Specifically, as an application of the species-based formulation, we model the in-situ upgrading of oil shale. We also apply the element-based formulation to model long-term carbon mineralization resulting from CO_2 injection in deep saline aquifers. These applications are described in more detail in the two sections that follow.

Table 1.1: Species and element-based formulations implemented in GPRS

Formulation	Species-based	Element-based
Kinetic reactions	Yes ¹	Yes
Equilibrium reactions	—	Yes
Phase equilibrium decoupling	Yes	Yes
Localized relation decoupling	Optional	Optional

¹ Elements in reactions can be unbalanced.

1.2 In-situ upgrading modeling

Oil shales are organic-rich sedimentary rocks that contain significant amounts of kerogen and generate oil upon pyrolysis or retorting [50]. Oil shale deposits are found in many parts of the world, and the kerogen in oil shales is recognized as one of the most abundant energy resources. A conservative estimate suggests that the total worldwide oil shale resources are equivalent to around 3×10^{12} barrels of oil [15]. The Green River formation in the western US is the largest known oil shale deposit in the world, containing approximately 1.5×10^{12} barrels of shale oil [15]. Although technologies for oil shale processing have been actively investigated in past decades [5], there has been renewed interest in recent years, due to both high oil prices and the promising field test results of Shell's In-situ Conversion Process [13]. Assuming oil shale production technologies are able to successfully address issues related to water use and carbon dioxide emissions [6], it is quite possible that oil shales may contribute to the future oil supply.

Kerogen in oil shales is believed to originate from the same types of organic matter that generated existing oil and gas accumulations. In the case of the oil shales, however, the natural maturation process, which would eventually lead to oil and gas, is at a very early stage and may still require millions of years. This process can be accelerated through either surface retorting or in-situ upgrading. Surface retorting requires that the oil shale be mined, followed by surface pyrolysis and further processing. This method is only suitable for shallow formations that can be mined economically. In-situ upgrading, by contrast, entails heating the oil shale in-situ using downhole heaters. Once the temperature reaches the appropriate window, chemical reactions occur and high quality products (with chemical composition resembling that

of light oil) can be produced. Since the in-situ upgrading process does not require mining, it is applicable for deeper oil shale deposits.

There are many technical, environmental and economic challenges associated with the in-situ upgrading and production of oil shales. In order to better understand these issues, and to design optimal production processes that minimize environmental impact, it is essential that we develop an accurate and efficient modeling capability. This represents a challenge, however, as the model must, at a minimum, entail a fully-compositional formulation that includes thermal effects and chemical reactions. Additional capabilities, such as thermal well models and geomechanical models, may also be required.

There have been a number of previous studies that are relevant to this work. A single-block kinetic model for oil shale pyrolysis was developed by Burnham and Braun [8]. This model provides predictions for oil generation given the pressure-temperature history. In later work, Braun *et al.* [7] presented a general chemical reaction model for oil and gas generation and compared model results to pyrolysis data. This model was a general chemical kinetic formulation that included 83 species and 100 reactions and was coupled with the Redlich-Kwong-Soave equation of state. Later, Burnham *et al.* [9] developed a simpler model consisting of 13 chemical species and ten chemical reactions to simulate the oil generation and expulsion from petroleum source rocks. This model was mainly applied to the oil generation process at geologic conditions. To our knowledge, it has not been implemented into a flow simulator for modeling coupled in-situ upgrading and flow processes.

Shell has applied the commercial thermal reservoir simulator STARS to model their in-situ upgrading field tests [62]. STARS is a generalized thermal-compositional

simulator coupled with chemical kinetics [37]. The phase equilibrium calculations in STARS are based on K-values and thus require a significant amount of experimental data if the number of species is large. Our formulation, by contrast, uses an equation of state (EOS) to calculate phase behavior. By assuring full consistency between the K-values and the EOS description, it is in principle possible to compare the results from STARS against our model. However, because much of Shell's work on in-situ upgrading is proprietary, detailed descriptions of their use of STARS for this problem are not available. Thus we will not attempt to compare our simulation predictions with theirs.

We apply our species-based formulation to simulate the Mahogany Demonstration Project-South, conducted by Shell [18]. This field test entails the use of 16 downhole electrical heaters placed in a pattern along with three production wells. Data for the kerogen and the kerogen decomposition products are taken from measurements of the pyrolysis of Green River oil shales reported by [7]. After tuning of uncertain input parameters constrained to fall within physical ranges, our simulations provide results for oil and gas production that are in reasonably close agreement with the Mahogany Demonstration Project-South. This provides a degree of validation for our chemical reaction modeling capability. We then perform a sensitivity analysis to study the impact of heater temperature, pattern type, and pattern spacing on oil and gas production. Such assessments will be essential for the optimization of this process in practice.

1.3 Modeling geologic carbon sequestration

We apply the element-based formulation to model the geochemical reactions relevant to geologic CO₂ sequestration in deep saline aquifers. Because the chemical reactions between dissolved CO₂ and the solid phase are mostly localized reactions, the element-based formulation with the localized reactions decoupled is well-suited for this application. However, the mineralization of CO₂ represents only one trapping mechanism. We now briefly review the various CO₂ trapping mechanisms in saline aquifers.

Deep saline aquifers are being actively studied for use in CO₂ sequestration because of their large storage capacity. After the CO₂ is injected into saline aquifers, the carbon is confined through a series of trapping mechanisms. In the order of increasing storage security, these mechanisms are (a) structural trapping, (b) residual trapping, (c) solubility trapping and (d) mineral trapping [23]. At early time, because most of the CO₂ remains in the gaseous (typically supercritical) phase, the major trapping mechanism is structural trapping. Due to buoyancy effects, the gas plume migrates upwards, resulting a certain percentage of CO₂ that is residually trapped. Within the same time frame, CO₂ dissolves into the water, which is referred to as solubility trapping. Over long times, significant amounts of carbon is stored in the minerals. This mineralization is described by CO₂-water-mineral reactions.

There are a number of numerical simulators that handle the first three trapping mechanisms. Class *et al.* conducted a benchmark study on the CO₂ sequestration in saline aquifers [12]. The simulators represented in the benchmark study are indicative of the capabilities of current simulation tools. The third problem in [12] is a model of a large heterogeneous reservoir with a fault. For simulations in which hysteresis is not

included (only structural and solubility trapping are modeled), the results from GPRS can be compared to those from COORES [32], ECLIPSE [21], GEM [36], MUFTE [1], TOUGH2 [52], VESA [19], and IPARS-CO2 [65]. The simulators yielded results that were in fairly close agreement. Only four of the simulators, GPRS, ECLIPSE, GEM, and VESA, include hysteresis (and thus residual trapping). It is interesting to note that the results from GPRS fall in the middle of the curves generated by these four simulators (see Figure 10 in [12]). This provides a degree of verification of the modeling capabilities for the first three trapping mechanisms in GPRS.

To quantify the long-term fate of CO_2 due to mineral trapping, geochemical reactions must also be included. Historically, simulations were mostly performed for batch reactions (single grid block) or for 1D reservoir models with detailed water-rock interactions (e.g., [66], [68], [69]). An ideal approach would be to model a field-sized aquifer with realistic minerals and reactions, though this will be very CPU intensive.

Accurate carbon mineralization requires sufficient knowledge of the underlying reaction laws. There are many challenges associated with quantifying the reaction laws for CO_2 mineralization. In high-salinity aquifers when the traditional activity models (e.g., ideal solution model, B-dot model [22]) no longer hold, the Pitzer model [51] should be used. However, because of absence of data for temperatures beyond room temperature, this approach has rarely been applied except for simple chemical systems [4]. In addition, the kinetic parameters associated with precipitation and dissolution of each mineral are subject to a wide range of uncertainty. Both the kinetic rate constant and the surface reactive area can vary over one to three orders of magnitude under reasonable assumptions [20]. Because the rate law generally includes the product of the kinetic rate and the surface area, the estimated reaction

rate can vary over six orders of magnitude. Thus it is important that the uncertainty associated with these parameters be reduced considerably.

Nevertheless, using available geochemical parameters, a few groups have succeeded in modeling the coupled reactive-transport processes for CO₂ mineral trapping. Nghiem *et al.* [42] modeled a 3D homogeneous reservoir containing $20 \times 20 \times 5 = 2,000$ grid blocks with six reactions using the commercial simulator GEM [36]. Their results show that the dissolved CO₂ in the aqueous phase promotes calcite dissolution. Audigane *et al.* [2] presented a 2D model (with $22 \times 52 \times 1 = 1,144$ blocks) that is representative of the Sleipner aquifer. The model in [2] contains three equilibrium minerals and six kinetic minerals. This model was simulated with TOUGHREACT for 10,000 years, and the results did not show much geochemical reactivity. Thus the authors concluded that mineral trapping was a minor effect.

In this work, we intend to provide a simulation tool for modeling model CO₂ storage in deep saline aquifers. Fine grid simulations can be achieved when modeling the structural, residual, and solubility trapping mechanisms without geochemical reactions. The element-based formulation can be applied to additionally model mineral trapping, though this is currently possible only for coarse-grid models. Much of the required data, though highly uncertain, are taken from available sources. This type of modeling capability will be essential for the eventual understanding and design of the CO₂ storage operations.

1.4 Dissertation outline

This dissertation proceeds as follows. In Chapter 2, the full set of governing equations is presented. Starting from the species-based conservation equations, we describe in

detail how the element-based formulation is achieved. In order to model a wide range of chemical reactions, a novel generalized reaction term is implemented. Then, numerical solution techniques are described, and two numerical examples are presented.

In Chapter 3, we apply the species-based reactive-transport formulation to model the in-situ upgrading of oil shale. The energy equation is also included in the system. We present detailed simulation results of a representative model based on Shell's Mahogany Demonstration Project-South. Then a sensitivity study is performed to assess the effects of heater temperature and heater locations on hydrocarbon production. The work presented in Chapter 3 will appear in *SPE Journal*.

In Chapter 4, we present simulation results from GPRS for a fine-grid benchmark study. The mechanisms considered in the fine-grid simulation include structural, residual and solubility trapping. We then apply the element-based approach to simulate geochemical reactions on a coarse grid. Verification of the geochemical modeling capability is accomplished by comparing our results to those of CMG's GEM simulator [36]. Because of the difficulties described in Section 1.3, the field scale reactive-transport modeling of CO_2 mineralization is not yet possible. We provide some explanation of the remaining difficulties.

Finally, in Chapter 5, we provide detailed conclusions and recommendations for future research directions.

Chapter 2

Chemical Reaction Modeling

In this chapter, we propose and implement a novel formulation for modeling coupled subsurface flow and chemical reactions. This formulation entails solving element conservation equations and includes treatment of kinetic and equilibrium reactions. We also develop a generalized scheme for implementing reaction laws within the context of a general purpose flow simulator. We apply Newton's method to solve the linear system derived from the governing equations. The size of the linear system is reduced using local constraint equations, including phase equilibrium relations, and in some cases, localized reaction relations. The resulting linear system is then solved with an iterative solver with proper preconditioners. Two examples are present to demonstrate the capabilities of this new formulation.

2.1 Governing equations and numerical formulation

The full set of governing equations consists of conservation equations, reaction relations, phase equilibrium relations and phase constraint equations. When the reactions are all kinetic reactions, we can write the conservation equations based purely on species (e.g., components). In such cases, the reaction rates expressed by the reaction relations are substituted into the conservation equations. We then solve the full set of governing equations in a manner similar to traditional compositional simulations without chemical reactions. We refer to this formulation as a species-based formulation.

When there are both kinetic and equilibrium reactions, we propose a new formulation that entails writing the conservation equations based on elements. The system is closed by adding one reaction relation for each chemical reaction. The element conservation equations are obtained from a matrix transformation of the existing species conservation equations. It is also possible to formulate the element conservation equations directly. This new formulation represents a unified framework for handling kinetic and equilibrium reactions. It can be applied as long as the elements in the reactions are balanced, which is the case if the full set of reactions is included in the model. Formulations exist in which one or more elements can be unbalanced. This is permissible when certain species do not need to be tracked. If the elements are not balanced, the formulation becomes equivalent to the species-based formulation. In the following sections, we assume all of the reactions are balanced.

2.1.1 Species and element conservation equations

We consider n_c species, including n_f fluid (or mobile) species and n_s solid (or immobile) species. We denote the unknown variable set by \mathbf{x} . In this dissertation, we consistently use the natural variable set as the unknowns:

$$\mathbf{x} = (p_j, S_j, C_s, X_{ij})^T, \quad (2.1)$$

where p_j is pressure of phase j , S_j is the saturation of fluid phase j , C_s is the volumetric concentration of solid species s in the rock phase, and X_{ij} is the mole fraction of fluid species i in fluid phase j . Usually the pressure for one phase is solved together with the other unknowns, and the pressure of the other phases are calculated by capillary relations. Therefore, we use p to represent the pressure of the target phase. The transport of all fluid species is determined based on the Darcy flow field, and local phase equilibrium is assumed throughout the entire computational domain.

We now suppose the model includes n_r reactions, of which n_q reactions are treated as equilibrium reactions and n_k reactions are treated as kinetic reactions ($n_r = n_k + n_q$). This mixed set of reactions can be represented by:

$$\sum_{i=1}^{n_f} \nu_{i,k} M_i + \sum_{s=1}^{n_s} \bar{\nu}_{s,k} M_s \xrightarrow{r_k} 0, \quad (k = 1, \dots, n_k), \quad (2.2)$$

$$\sum_{i=1}^{n_f} \nu_{i,q} M_i + \sum_{s=1}^{n_s} \bar{\nu}_{s,q} M_s \xrightarrow{r_q} 0, \quad (q = n_k + 1, \dots, n_r), \quad (2.3)$$

where M_i and M_s are the chemical symbols for fluid species i and solid species s , $\nu_{i,k}$ and $\bar{\nu}_{s,k}$ are stoichiometric coefficients of fluid species i and solid species s in kinetic reaction k , and $\nu_{i,q}$ and $\bar{\nu}_{s,q}$ are stoichiometric coefficients in equilibrium reaction q .

We use r_k and r_q to represent the rates for kinetic reactions and equilibrium reactions.

The generalized mass balance equations for a multiphase reactive-transport problem are represented by (adapted from [30]):

$$\frac{\partial N_i}{\partial t} + L_i = \sum_{k=1}^{n_k} \nu_{i,k} r_k + \sum_{q=n_k+1}^{n_r} \nu_{i,q} r_q, \quad (2.4)$$

$$\frac{\partial C_s}{\partial t} = \sum_{k=1}^{n_k} \bar{\nu}_{s,k} r_k + \sum_{q=n_k+1}^{n_r} \bar{\nu}_{s,q} r_q. \quad (2.5)$$

In (2.4), N_i is the total molar mass of fluid species i in each block:

$$N_i = \sum_{j=1}^{n_p} (\rho_j \phi S_j X_{ij}), \quad (2.6)$$

where n_p is the number of fluid phases, ρ_j is the density of phase j (which is a function of pressure, temperature, and molar fractions,) and ϕ is porosity. The flux term L_i includes advective flux, diffusive and dispersive flux, and the well source term:

$$L_i = \nabla \cdot \sum_{j=1}^{n_p} (\rho_j X_{ij} \mathbf{u}_j - \rho_j \phi S_j \mathbf{D}_{ij} \nabla X_{ij}) + q_i^W, \quad (2.7)$$

where \mathbf{u}_j is the Darcy velocity for phase j , \mathbf{D}_{ij} is the dispersivity tensor for fluid species i in phase j , and q_i^W is the well rate of species i . The units of all of the terms and the reaction rates are $[\text{mol}][\text{m}]^{-3}[\text{s}]^{-1}$ (in field units, $[\text{lb mol}][\text{ft}]^{-3}[\text{day}]^{-1}$). The units of the dispersivity tensor are $[\text{m}][\text{s}]^{-1}$ (in field units, $[\text{ft}][\text{day}]^{-1}$).

For the sake of simplicity, we now write (2.4) and (2.5) in matrix-vector form:

$$\frac{\partial \mathbf{N}}{\partial t} + \mathbf{L} = \mathbf{S}\mathbf{R}. \quad (2.8)$$

In (2.8), the vector \mathbf{N} consists of the total molar mass of both fluid species and solid species; i.e., $\mathbf{N} = (N_1, \dots, N_{n_f}, C_1, \dots, C_{n_s})^T$. The flux vector \mathbf{L} has non-zero values for fluid species and zeros for solid species, i.e., $\mathbf{L} = (L_1, \dots, L_{n_f}, 0, \dots, 0)^T$. The dimensions of both \mathbf{N} and \mathbf{L} are $(n_f + n_s) = n_c$, where n_c is the total number of species. The reaction term vector \mathbf{R} consists of the kinetics term \mathbf{r}_k and the equilibrium term \mathbf{r}_q :

$$\mathbf{R} = \begin{pmatrix} \mathbf{r}_k \\ \mathbf{r}_q \end{pmatrix} = (r_1, \dots, r_{n_k}, r_{n_k+1}, \dots, r_{n_r})^T. \quad (2.9)$$

The stoichiometric matrix \mathbf{S} has $n_c \times n_r$ stoichiometric coefficients for each species in each reaction:

$$\mathbf{S}_{n_c \times n_r} = \begin{bmatrix} \mathbf{S}_k & \mathbf{S}_q \end{bmatrix} = \begin{bmatrix} \mathbf{S}_{fk} & \mathbf{S}_{fq} \\ \mathbf{S}_{sk} & \mathbf{S}_{sq} \end{bmatrix}, \quad (2.10)$$

where the stoichiometric submatrix \mathbf{S}_k corresponds to kinetic reactions and \mathbf{S}_q to equilibrium reactions. Further, \mathbf{S}_{fk} corresponds to fluid species in kinetic reactions, \mathbf{S}_{fq} to fluid species in equilibrium reactions, \mathbf{S}_{sk} to solid species in kinetic reactions, and \mathbf{S}_{sq} to solid species in equilibrium reactions:

$$\mathbf{S}_{fk} = \begin{bmatrix} \nu_{1,1} & \cdots & \nu_{1,n_k} \\ \cdots & \cdots & \cdots \\ \nu_{n_f,1} & \cdots & \nu_{n_f,n_k} \end{bmatrix}, \quad \mathbf{S}_{fq} = \begin{bmatrix} \nu_{1,n_k+1} & \cdots & \nu_{1,n_r} \\ \cdots & \cdots & \cdots \\ \nu_{n_f,n_k+1} & \cdots & \nu_{n_f,n_r} \end{bmatrix}, \quad (2.11)$$

$$\mathbf{S}_{sk} = \begin{bmatrix} \bar{\nu}_{1,1} & \cdots & \bar{\nu}_{1,n_k} \\ \cdots & \cdots & \cdots \\ \bar{\nu}_{n_s,1} & \cdots & \bar{\nu}_{n_s,n_k} \end{bmatrix}, \quad \mathbf{S}_{sq} = \begin{bmatrix} \bar{\nu}_{1,n_k+1} & \cdots & \bar{\nu}_{1,n_r} \\ \cdots & \cdots & \cdots \\ \bar{\nu}_{n_s,n_k+1} & \cdots & \bar{\nu}_{n_s,n_r} \end{bmatrix}. \quad (2.12)$$

Without loss of generality, we now assume that the set of reactions is linearly independent. In fact, if a reaction can be expressed by a combination of other reactions, this reaction becomes redundant and should be eliminated [41]. We further assume that all of the elements involved in the reactions are balanced. For n_r independent reactions involving n_c species and n_e elements, it can be shown that $n_c = n_e + n_r$. If all the elements in the reactions are balanced, it can be further shown that

$$\mathbf{E}_{n_e \times n_c} \mathbf{S}_{n_c \times n_r} = \mathbf{0}_{n_e \times n_r}, \quad (2.13)$$

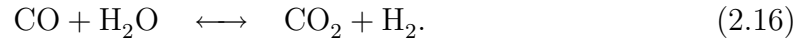
where \mathbf{E} is the element stoichiometric matrix consisting of all the stoichiometric values for each element in each species:

$$\mathbf{E} = \begin{bmatrix} E_{1,1} & \cdots & E_{1,n_c} \\ \cdots & E_{ei} & \cdots \\ E_{n_e,1} & \cdots & E_{n_e,n_c} \end{bmatrix}. \quad (2.14)$$

Here E_{ei} represents the number of atoms of element e in species i . Equation (2.13) holds for both fluid and solid species and for both kinetic and equilibrium reactions. We now illustrate (2.13) with an example.

Consider the reaction network involving five species, CO, H₂O, H₂, CO₂, and O₂,

and two independent balanced reactions:



These two reactions can be either kinetic or equilibrium reactions. The elements involved are C, H, and O. The element stoichiometric and reaction stoichiometric matrices are:

$$\mathbf{E} = \begin{bmatrix} 1 & 0 & 0 & 1 & 0 \\ 0 & 2 & 2 & 0 & 0 \\ 1 & 1 & 0 & 2 & 2 \end{bmatrix}, \quad \mathbf{S} = \begin{bmatrix} -2 & -1 \\ 0 & -1 \\ 0 & 1 \\ 2 & 1 \\ -1 & 0 \end{bmatrix} \Rightarrow \mathbf{ES} = \begin{bmatrix} 0 & 0 \\ 0 & 0 \\ 0 & 0 \end{bmatrix}. \quad (2.17)$$

The fact that $\mathbf{ES} = \mathbf{0}$ means that, in general, we can project the n_c species conservation equations in (2.8) to n_e element conservation equations. This eliminates the reaction terms from the right hand side of (2.8); i.e.,:

$$\frac{\partial(\mathbf{EN})}{\partial t} + \mathbf{EL} = \mathbf{ESR} \quad (2.18)$$

$$\Rightarrow \frac{\partial(\mathbf{EN})}{\partial t} + \mathbf{EL} = \mathbf{0}. \quad (2.19)$$

Equation (2.19) is in effect the system of conservation equations for each element involved in the reactions. The dimension of the new accumulation term $\partial(\mathbf{EN})/\partial t$

and flux term \mathbf{EL} are $n_e \times 1$. In our element-based approach, instead of solving (2.8), we solve (2.19) plus n_r reaction relations, which will be described next.

2.1.2 Reaction characterization

As shown in the previous section, the n_c species conservation equations may have both kinetic or equilibrium terms r_k or r_q . The new element conservation equations, by contrast, do not have any reaction terms. The system is fully defined by adding n_r relations, one for each independent reaction. Each relation is written as a function of the unknown variable set \mathbf{x} .

For n_c species involving n_k independent kinetic reactions, it can be shown that a canonical stoichiometric matrix $\bar{\mathbf{S}}_k$ can be defined [42]:

$$\bar{\mathbf{S}}_k = \begin{bmatrix} -\mathbf{I}_{n_k \times n_k} \\ \tilde{\mathbf{S}}_{(n_c - n_k) \times n_k} \end{bmatrix}, \quad (2.20)$$

where \mathbf{I} is the identity matrix and $\tilde{\mathbf{S}}$ contains the remaining stoichiometric kinetic coefficients. When the kinetic stoichiometric matrix is written in this form, each of the first n_k species can be expressed in terms of the remaining $(n_c - n_k)$ species; i.e.,

$$M_\varsigma \xrightarrow{r_k} \sum_{\xi=n_k+1}^{n_c} \tilde{\nu}_{\xi,k} M_\xi, \quad (\varsigma = 1, \dots, n_k), \quad (2.21)$$

where ς is the species index for the first n_k species and ξ is the species index for the remaining species.

The canonical stoichiometric matrix $\bar{\mathbf{S}}_k$ is equivalent to \mathbf{S}_k in (2.10). For a given chemical system, \mathbf{S}_k can be written in the form of (2.20) by appropriate ordering of

the species and through linear combination of reactions [41]. For example, consider the reaction network defined by (2.15) and (2.16), with both reactions assumed to be kinetic reactions. When the species are ordered as CO, H₂O, H₂, CO₂, and O₂, the kinetic stoichiometric matrix \mathbf{S}_k is given in (2.17), with each column representing a reaction. The canonical form can be obtained in this simple case by reordering the species as O₂, H₂O, H₂, CO₂, and CO:

$$\mathbf{S}_k = \begin{bmatrix} -2 & -1 \\ 0 & -1 \\ 0 & 1 \\ 2 & 1 \\ -1 & 0 \end{bmatrix} \Rightarrow \bar{\mathbf{S}}_k = \begin{bmatrix} -1 & 0 \\ 0 & -1 \\ 0 & 1 \\ 2 & 1 \\ -2 & 1 \end{bmatrix}. \quad (2.22)$$

Because $\bar{\mathbf{S}}_k$ and \mathbf{S}_k are equivalent, from here on we assume that the kinetic stoichiometric matrix is in canonical form. The reaction relations corresponding to the kinetic reactions (2.21) are essentially the mass conservation equations for each species ς . The kinetic rate r_k is a function of the unknowns; i.e., $r_k = r_k(\mathbf{x})$. We note that species ς can either be a fluid species or a solid species. If species ς is a fluid species, this reaction relation is a partial differential equation (PDE):

$$r_k(\mathbf{x}) = \frac{\partial N_\varsigma(\mathbf{x})}{\partial t} + L_\varsigma(\mathbf{x}). \quad (2.23)$$

We refer to this type of reaction as a “fluid kinetic reaction” and denote n_{kf} as the number of fluid kinetic reactions. In the reaction network given by (2.15) and (2.16) with the stoichiometry given in canonical form in (2.22), we can write (2.23) for both

reactions in terms of O_2 and H_2O :

$$r_1(\mathbf{x}) = \frac{\partial N_{O_2}(\mathbf{x})}{\partial t} + L_{O_2}(\mathbf{x}), \quad r_2(\mathbf{x}) = \frac{\partial N_{H_2O}(\mathbf{x})}{\partial t} + L_{H_2O}(\mathbf{x}). \quad (2.24)$$

In contrast to (2.23), if species ς is a solid species, the relation for this reaction is an ordinary differential equation (ODE):

$$r_k(\mathbf{x}) = \frac{dC_\varsigma(\mathbf{x})}{dt}. \quad (2.25)$$

We refer to the reaction described by (2.25) as a “solid kinetic reaction,” and denote n_{ks} to be the number of solid kinetic reactions. The solid kinetic reaction is an ODE rather than a PDE because the solid phase does not have a flux term associated with it.

For equilibrium reactions, we can write n_q algebraic equations (AE) to describe the equilibrium reactions:

$$Q_q(\mathbf{x}) - K_q = 0, \quad (2.26)$$

where Q_q is the product of species concentrations or activities and K_q is the equilibrium constant that may depend on temperature or pressure.

We note that the reactions described in (2.25) and (2.26) are localized relations. When solving fully coupled reactive-transport problems, all localized reactions can be solved separately. Thus the problem size of the system will be significantly reduced if most or all of the reactions are equilibrium or mineral kinetic reactions.

A useful way to differentiate equilibrium and kinetic reactions in transport problems is through the dimensionless Damköhler number Da , which measures the ratio of the characteristic timescale for transport to that of chemical kinetics. Here we define a block Damköhler number as $Da = K\Delta x/u$, where K is the kinetic reaction rate constant in units of 1/day, Δx is the characteristic block length in ft, and u is the Darcy velocity in ft/day. Figure 2.1 shows a set of simulation results for one-dimensional single-phase flow at constant u , with a reversible reaction, $A \leftrightarrow B$, where A and B are passive-tracer components which are fully dissolved in the water phase. The simulation with $Da = 0$ corresponds to a pure tracer flow scenario and $K = 0$. Figure 2.1 also shows four scenarios in which the kinetic rates are nonzero. For these runs the values of Da are 0.1, 1, 10 and 100.

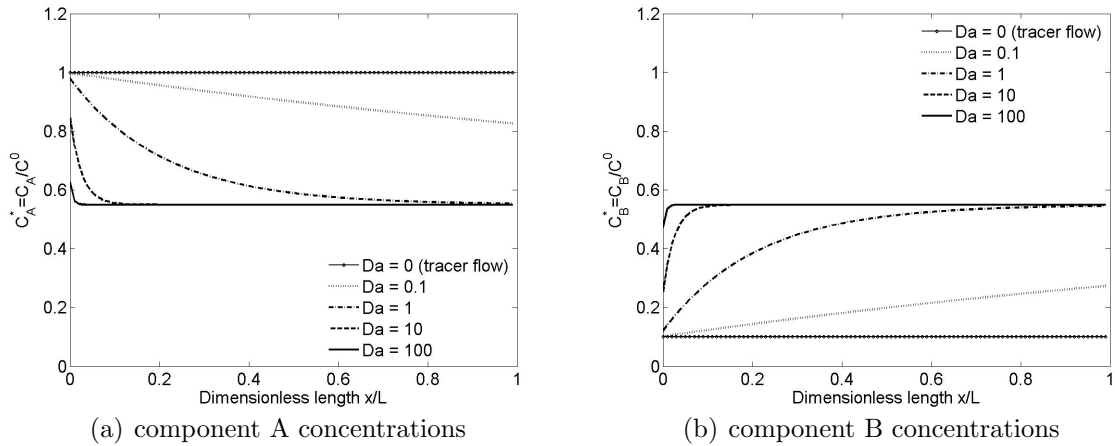


Figure 2.1: Dimensionless component concentrations for different values of Da .

We can see from Figure 2.1 that the Damköhler number is a good indicator of kinetic rates compared to transport rates. When $Da > 100$, the concentrations of components A and B are identical over almost the entire domain, suggesting that the reaction may be treated as an equilibrium reaction. In contrast, when $Da < 100$, the

reaction should be treated as a kinetic reaction.

Although the Damköhler number does provide a means for classifying reactions, the critical value (100 in this case) will depend on the particular scenario. In addition, for a heterogeneous reservoir under transient flow conditions, it is usually difficult to define a unique critical value of Da . In Section 2.4.2, we will show a transient flow case in which the Damköhler number varies in space and time; such a case cannot be classified in terms of a single Damköhler number. Therefore, in this work, rather than classify reactions as kinetic or equilibrium based on Da , we adopt the practice common in groundwater modeling of treating all of the intra-aqueous reactions as equilibrium and all others as kinetic reactions.

2.1.3 Phase equilibrium calculation

Phase equilibrium calculations are the same as in traditional compositional modeling. Local phase equilibrium is assumed throughout this formulation. The phase equilibrium is calculated using an equation of state (EOS). The phase equilibrium relation for each fluid species is expressed as:

$$f_i^g - f_i^l = 0, \quad (2.27)$$

where f_i^g and f_i^l are the fugacities of fluid species i in the gaseous and liquid phases. We apply the Peng-Robinson EOS to compute the thermodynamic equilibrium state.

If all of the fluid species can exist in both the gaseous and liquid phases, the number of equations in (2.27) is n_f . If some fluid species can exist in only one phase, the number of equations in (2.27) will be less than n_f . In such cases, the number of unknowns corresponding to X_{ij} will also decrease so that the total number

of equations is always equal to the total number of unknowns. In addition to the equations above, n_p composition constraints are added to the governing equation set as follows:

$$\sum_i X_{ij} = 1, \text{ for each } j. \quad (2.28)$$

For systems consisting of n_p fluid phases, there are $(n_p - 1)$ independent capillary pressure relations. For example, in a system composed of oil and gas phases, the capillary relation is

$$p_o - p_g = P_{c,og}, \quad (2.29)$$

where p_o and p_g are pressures for the oil and gas phases and $P_{c,og}$ is the gas-oil capillary pressure. One saturation constraint equation should be added when $n_p > 1$:

$$\sum_j S_j = 1. \quad (2.30)$$

2.1.4 Summary of governing equations

In summary, the governing equations in our method include (2.19), (2.23), (2.25), (2.26), (2.27), (2.28), (2.29) and (2.30). If wells are also modeled, the governing equations for each well will also appear. The well equations are described in detail in [10] and [26]. The major difference between this element-based method and other formulations is that the element conservation equations developed here do not have reaction terms. As a result, the localized reactions (i.e., solid kinetic reactions and equilibrium reactions) decouple. In addition, the equilibrium reaction rates r_q do not

appear in any equations.

According to (2.1), the total number of unknowns for isothermal simulations is $2n_p + n_s + n_p n_f$, where n_p is the number of fluid phases, n_s is the number of solid species, and n_f is the number of fluid species. The set of governing equations is summarized in Table 2.1. Given that $n_r = n_{kf} + n_{ks} + n_q$, the total number of equations is $n_e + n_r + (n_p - 1)n_f + 2n_p$. We note that in a fully characterized system, $n_c = n_f + n_s = n_e + n_r$. Therefore, the total number of equations becomes $2n_p + n_s + n_p n_f$, which is equal to the number of unknowns.

Table 2.1: Summary of governing equations

Description	Equation	Number
Element balance equations	(2.19)	n_e
Fluid kinetics reactions	(2.23)	n_{kf}
Solid kinetic reactions	(2.25)	n_{ks}
Equilibrium reactions	(2.26)	n_q
Phase equilibriums	(2.27)	$(n_p - 1)n_f$
Mole fraction constraints	(2.28)	n_p
Capillary equations	(2.29)	$n_p - 1$
Saturation constraint	(2.30)	1

2.2 Generalized reaction implementation

Scientists and engineers have used several different conventions to describe components in mixtures when proposing reaction laws. Concentrations or partial pressures are the most commonly used variables in reaction laws (for both kinetic and equilibrium reactions). However, when describing solution mixtures, especially aqueous solutions involving electrolytes, activities are often used instead of concentrations.

Though activity is a measure of the “effective concentration” of a given component in a mixture, it is often inconvenient to convert activities to concentrations. In our formulation, generic representations of reaction terms are used in order to model a wide range of problems. With this approach, both concentration and activity of fluid species and solid species are included in the fully coupled algorithm. All of the nonlinear reaction terms are taken to be functions of the unknown variable set described in (2.1).

2.2.1 Generic nonlinear reaction terms

The unknown variable set \mathbf{x} consists of one pressure p , saturations S_j , mole fractions X_{ij} , and mineral concentrations C_s . In our global implicit scheme, we apply Newton’s method. Thus, the derivatives of the nonlinear reaction terms (r_k or Q_q) with respect to the unknowns are required. The reaction terms can be represented in the following generalized form

$$r_k = r_k(\sigma_{ij}, \sigma_s), \quad (2.31)$$

$$Q_q = Q_q(\sigma_{ij}, \sigma_s), \quad (2.32)$$

where σ_{ij} represents either the concentration or the activity of fluid species i in phase j and σ_s represents either the concentration or the activity of mineral species s . We use C to represent concentration and a to represent activity; e.g., C_{ij} is the concentration of fluid species i in phase j . The derivatives of r_k and Q_q with respect to the unknowns

are calculated using the chain rule:

$$\frac{\partial r_k}{\partial \mathbf{x}} = \sum_{j=1}^{n_p} \sum_{i=1}^{n_f} \left[\frac{\partial r_k}{\partial \sigma_{ij}} \frac{\partial \sigma_{ij}}{\partial \mathbf{x}} \right] + \sum_{s=1}^{n_s} \left[\frac{\partial r_k}{\partial \sigma_s} \frac{\partial \sigma_s}{\partial \mathbf{x}} \right], \quad (2.33)$$

$$\frac{\partial Q_q}{\partial \mathbf{x}} = \sum_{j=1}^{n_p} \sum_{i=1}^{n_f} \left[\frac{\partial Q_q}{\partial \sigma_{ij}} \frac{\partial \sigma_{ij}}{\partial \mathbf{x}} \right] + \sum_{s=1}^{n_s} \left[\frac{\partial Q_q}{\partial \sigma_s} \frac{\partial \sigma_s}{\partial \mathbf{x}} \right]. \quad (2.34)$$

Equations (2.33) and (2.34) have been implemented using object-oriented programming techniques. This provides a unified platform to assemble all the derivatives regardless of the specific reaction type or the reaction law. This representation can also handle heterogeneous reactions characterized by a combination of concentrations or activities; e.g., the species in the gaseous phase can be described by activities and the species in the liquid phase by concentrations. In a given application, only non-zero derivatives in (2.33) and (2.34) need to be calculated and assembled.

We now illustrate the assembly procedure with two examples. The first example entails chemical reactions that are characterized by fluid and solid concentrations. The second example, by contrast, involves fluid and solid activities.

2.2.2 Concentration type reaction

If a reaction is characterized in terms of both fluid and solid concentrations, we take σ_{ij} as C_{ij} and σ_s as C_s . Thus (2.33) and (2.34) are treated as

$$\frac{\partial r_k}{\partial \mathbf{x}} = \sum_{j=1}^{n_p} \sum_{i=1}^{n_f} \left[\frac{\partial r_k}{\partial C_{ij}} \frac{\partial C_{ij}}{\partial \mathbf{x}} \right] + \sum_{s=1}^{n_s} \left[\frac{\partial r_k}{\partial C_s} \frac{\partial C_s}{\partial \mathbf{x}} \right], \quad (2.35)$$

$$\frac{\partial Q_q}{\partial \mathbf{x}} = \sum_{j=1}^{n_p} \sum_{i=1}^{n_f} \left[\frac{\partial Q_q}{\partial C_{ij}} \frac{\partial C_{ij}}{\partial \mathbf{x}} \right] + \sum_{s=1}^{n_s} \left[\frac{\partial Q_q}{\partial C_s} \frac{\partial C_s}{\partial \mathbf{x}} \right]. \quad (2.36)$$

If the reaction is a kinetic reaction, (2.35) should be used; if the reaction is an equilibrium reaction, (2.36) should be used. We now provide an example involving r_k . The specific forms of the derivatives $\partial r_k / \partial C_{ij}$ and $\partial r_k / \partial C_s$ depend on the expression for r_k . For example, if the reaction follows the law of mass action, the reaction rate can be represented by

$$r_k = K_k \prod_{i,j} C_{ij}^{\nu_{ij,k}} \prod_s C_s^{\nu_{s,k}}, \quad (2.37)$$

where K_k is the reaction rate constant. The derivatives of r_k with respect to C_{ij} and C_s in this case are represented by

$$\frac{\partial r_k}{\partial C_{ij}} = \frac{\nu_{ij,k} r_k}{C_{ij}}, \quad \frac{\partial r_k}{\partial C_s} = \frac{\nu_{s,k} r_k}{C_s}. \quad (2.38)$$

Since the fluid concentration C_{ij} is related to the unknown variable set by

$$C_{ij} = \rho_j S_j \phi X_{ij}, \quad (2.39)$$

it is straightforward for us to obtain the derivatives of fluid concentration with respect to the unknown variable set:

$$\frac{\partial C_{ij}}{\partial p} = \frac{\partial \rho_j}{\partial p} S_j \phi X_{ij} + \rho_j \frac{\partial \phi}{\partial p} S_j X_{ij}, \quad (2.40)$$

$$\frac{\partial C_{ij}}{\partial S_\beta} = \rho_j \delta_{j\beta} \phi X_{ij}, \quad (2.41)$$

$$\frac{\partial C_{ij}}{\partial X_{\alpha\beta}} = \frac{\partial \rho_j}{\partial X_{\alpha\beta}} S_j \phi X_{ij} + \rho_j \phi S_j \delta_{i\alpha} \delta_{j\beta}, \quad (2.42)$$

where α and β are target phase and species derivative indices and δ is the Kronecker delta function.

We now calculate the derivatives of C_s with respect to the unknown set \mathbf{x} . We note that because C_s is taken as one of the unknown variables, only the derivatives of C_s with respect to itself are nonzero; i.e.,

$$\frac{\partial C_s}{\partial p} = 0, \quad \frac{\partial C_s}{\partial S_j} = 0, \quad \frac{\partial C_s}{\partial C_\chi} = \delta_{s\chi}, \quad \frac{\partial C_s}{\partial X_{ij}} = 0, \quad (2.43)$$

where χ is a mineral component index.

Substituting equations (2.38), (2.40)-(2.42) and (2.43) into (2.35), we can obtain all required derivatives of the reaction term r_k . A similar procedure can be followed to obtain the derivatives of Q_q in (2.36).

2.2.3 Activity type reactions

As stated above, the derivatives of r_k and Q_q depend on the specific form of the reaction law. For activity type reaction laws, equations (2.33) and (2.34) are taken as:

$$\frac{\partial r_k}{\partial \mathbf{x}} = \sum_{j=1}^{n_p} \sum_{i=1}^{n_f} \left[\frac{\partial r_k}{\partial a_{ij}} \frac{\partial a_{ij}}{\partial \mathbf{x}} \right] + \sum_{s=1}^{n_s} \left[\frac{\partial r_k}{\partial a_s} \frac{\partial a_s}{\partial \mathbf{x}} \right], \quad (2.44)$$

$$\frac{\partial Q_q}{\partial \mathbf{x}} = \sum_{j=1}^{n_p} \sum_{i=1}^{n_f} \left[\frac{\partial Q_q}{\partial a_{ij}} \frac{\partial a_{ij}}{\partial \mathbf{x}} \right] + \sum_{s=1}^{n_s} \left[\frac{\partial Q_q}{\partial a_s} \frac{\partial a_s}{\partial \mathbf{x}} \right]. \quad (2.45)$$

We now use a mineral precipitation and dissolution rate law as an example. In this example, the activities of minerals are set to unity by convention. Thus $\partial a_s / \partial \mathbf{x} = 0$.

The kinetic law of mineral precipitation and dissolution is represented by:

$$r_k = K_k A_k \left(1 - \frac{\prod_{i,j} a_{ij}^{\nu_{ij,k}}}{K_{eq,k}} \right), \quad (2.46)$$

where K_k is the kinetic rate constant, A_k is the reactive surface area used for reaction k , and $K_{eq,k}$ is the equilibrium constant for reaction k . The derivative of r_k with respect to a_{ij} can be obtained from equation (2.46):

$$\frac{\partial r_k}{\partial a_{ij}} = -K_k A_k \left(\frac{\nu_{ij,k} \prod_{i,j} a_{ij}^{\nu_{ij,k}}}{a_{ij} K_{eq,k}} \right). \quad (2.47)$$

The derivatives $\partial a_{ij}/\partial \mathbf{x}$ depend on the specific definition of activity. Heterogeneous reactions involving more than one phase may have different definitions of activity in each phase. By convention, the activity of gaseous species is often represented by fugacity:

$$a_{ig} = \frac{f_{ig}}{P^0} = \frac{\phi_{ig} X_{ig} P}{P^0}, \quad (2.48)$$

where f_{ig} is the fugacity of species i in the gaseous phase, P^0 is standard pressure (often taken as 1 bar), and ϕ_{ig} is the dimensionless fugacity coefficient for species i . If the gas species behaves ideally, then $\phi_{ig} = 1$.

In contrast to the gaseous phase, the activity of aqueous species is often written in terms of molality: $a_{iw} = \gamma_{iw}(m_{iw}/m^0)$, where γ_{iw} is the activity coefficient for species i in the aqueous phase, m_{iw} is the molality of species i in the aqueous phase, and m^0 is standard molality. Both activity and activity coefficients are dimensionless. Since the standard molality of solute species m^0 is often taken as $1 \text{ mol}\cdot\text{kg}^{-1}$, it is common

to drop m^0 from the activity definition. The molality m_{iw} is further related to molar fractions by $m_{iw} = 55.508X_{iw}/X_{ww}$, where the value 55.508 is the number of moles of H₂O per kilogram, X_{iw} is the mole fraction of each solute species, and X_{ww} is the molar fraction of H₂O in the aqueous phase. Therefore, we can write the activity of aqueous species (except water) as:

$$a_{iw} = 55.508 \left(\frac{\gamma_{iw}X_{iw}}{X_{ww}} \right), \quad (i \neq w). \quad (2.49)$$

Various models can be applied to calculate the activity coefficients γ_{iw} (e.g., ideal, B-dot [22], or Pitzer [51] models). The results shown below were obtained from the B-dot model:

$$\log \gamma_{iw} = -\frac{Az_i^2\sqrt{I}}{1 + \hat{a}_iB\sqrt{I}} + \dot{B}I, \quad (2.50)$$

where A , B , and \dot{B} are temperature-dependent constants, z_i is the ion electrical charge for species i , I is the ionic strength of the aqueous phase, and \hat{a}_i is the ion size of species i .

Following these definitions, we can write the non-zero derivatives of the activities as:

$$\frac{\partial a_{ig}}{\partial p} = \frac{1}{P^0} \left(\frac{\partial \phi_{ig}}{\partial p} X_{ig}p + \phi_{ig}X_{ig} \right), \quad (2.51)$$

$$\frac{\partial a_{ig}}{\partial X_{\alpha g}} = \frac{1}{P^0} \left(\frac{\partial \phi_{ig}}{\partial X_{\alpha g}} X_{ig}p + \phi_{ig}\delta_{i\alpha}p \right), \quad (2.52)$$

$$\frac{\partial a_{iw}}{\partial X_{\alpha w}} = \frac{a_{iw}\delta_{i\alpha}}{X_{ww}}, \quad (i \neq w, \alpha \neq w), \quad (2.53)$$

$$\frac{\partial a_{iw}}{\partial X_{ww}} = -\frac{a_{iw}}{X_{ww}}, \quad (i \neq w). \quad (2.54)$$

Substituting (2.47) and (2.51)-(2.54) into equation (2.44) completes the specification of the derivatives of r_k for activity type reactions. A similar procedure is followed to calculate the derivatives in equation (2.45).

2.3 Numerical solution techniques

We apply Newton's method to solve the coupled equations. Figure 2.2 shows the flow chart for solving the coupled multiphase flow and reaction problems. The fully coupled system requires calculation of the derivatives of the residuals of all of the governing equations with respect to the unknown variables. The resulting derivatives are inserted into the Jacobian matrix. We then reduce the number of equations and variables to a set that is solved simultaneously. This reduction procedure is performed at the Jacobian level. The first step of the reduction procedure is to build a Schur complement of the full Jacobian matrix using the phase equilibrium relations. The second step is optional. When there are localized reactions in the system, we can decouple the localized reaction relations from the conservation equations. The reduced set of equations (variables) are referred to as primary equations (variables). In general, advanced linear solvers are required to solve the primary equations. The remaining secondary variables are recovered after each Newton iteration.

2.3.1 Application of Newton's method

The full set of governing equations (2.19)-(2.28) is solved in time using Newton's method at each time step. A fully implicit scheme is applied. We denote \mathbf{F} to be the residual vector of all of the governing equations. Given the variables at time t , we

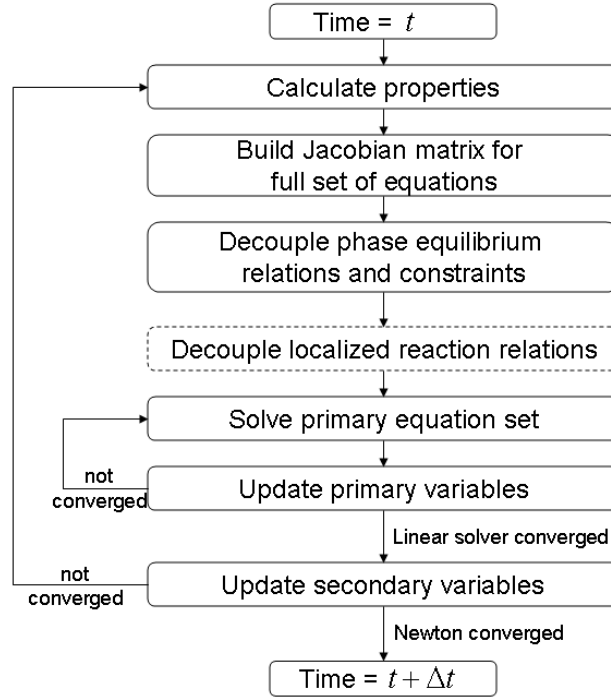


Figure 2.2: Flow chart for the solution of the fully coupled multiphase flow and reactive problems.

now proceed to calculate the unknowns at time $t + \Delta t$. The nonlinear equation set can be expressed as:

$$\mathbf{F}(\mathbf{x}^{t+\Delta t}) = \mathbf{0}. \quad (2.55)$$

In most cases, an appropriate initial guess for Newton's method is the solution at the previous time step, which we designate as \mathbf{x}^t :

$$\mathbf{x}^0 = \mathbf{x}^t. \quad (2.56)$$

Here we view the initial guess \mathbf{x}^0 as the value of \mathbf{x} at 0-th Newton iteration. We denote $\delta\mathbf{x}$ to be the difference in \mathbf{x} at iteration $v + 1$ from \mathbf{x} at the previous iteration v : $\delta\mathbf{x} = \mathbf{x}^{v+1} - \mathbf{x}^v$. At iteration v , we calculate the derivatives of \mathbf{F} with respect to the unknowns, which gives the Jacobian matrix \mathbf{J} :

$$\mathbf{J} = \left(\frac{\partial \mathbf{F}}{\partial \mathbf{x}} \right)^v. \quad (2.57)$$

Newton's method requires the solution of the following linear equation:

$$\mathbf{J}\delta\mathbf{x} = -\mathbf{F}(\mathbf{x}^v), \quad (2.58)$$

which gives $\delta\mathbf{x}$ and thus \mathbf{x}^{v+1} by:

$$\mathbf{x}^{v+1} = \mathbf{x}^v + \delta\mathbf{x}. \quad (2.59)$$

Once equation (2.55) converges, we set \mathbf{x}^{v+1} to $\mathbf{x}^{t+\Delta t}$, and proceed to the next time step.

2.3.2 Reduction of the problem size

The representation of the governing equations in terms of primary and secondary equations reduces the total number of variables in the linear solution. In a typical compositional simulation, a significant amount of CPU time is required for the (typically iterative) linear solution of the primary equations in (2.58). It is thus desirable to solve the problem with the minimum number of primary equations.

The selection of primary equations depends on the nature of the governing equation set. By solving the primary equations, we obtain the values for the primary unknowns at the specific Newton iteration. The secondary equations are then applied to calculate the remaining unknowns. The governing equations being solved are the same for any selection of primary versus secondary equations, so the solution is the same for any selection. However, although the solution accuracy is not affected by different choices of primary equations, the simulator performance can be significantly impacted by the selection of primary equations.

Selection of primary equations

We now illustrate how we select primary equations from the full set of equations. As will be shown in the next section, the governing equations without flux terms can be treated as secondary equations. For our element-based method, there are two ways to split the full set of equations. The first approach treats element conservation equations (2.19) and reaction relations (2.23)-(2.26) as primary equations, and the phase equilibrium relations (2.27) and constraints (2.28) as secondary equations. The benefit of this treatment is that its implementation is easier to accomplish, because most compositional reservoir simulators already separate the phase equilibrium and constraints into secondary equations. Thus a developer only needs to properly define element conservation equations and reaction relations as primary equations. We refer to this approach as “reactions coupled,” because all the reactions are coupled with the conservation equations.

The second approach further differentiates reaction relations based on flux terms.

Because mineral kinetic reactions and equilibrium reactions are localized, their reaction relations described by (2.25) and (2.26) can be classified as secondary equations. Therefore, the primary equations now only have element conservation equations (2.19) and fluid kinetic relations (2.23). We will refer to this approach as the “local reactions decoupled” method. The benefit of decoupling local reactions is that the linear system is further reduced. Table 2.2 summarizes the selection of primary equations for the two approaches.

Table 2.2: Primary and secondary equations for the two approaches

Description	Reactions coupled	Local reactions decoupled
Primary equations	(2.19), (2.23), (2.25), (2.26)	(2.19), (2.23)
Secondary equations	(2.27), (2.28)	(2.25), (2.26), (2.27), (2.28)

When there are two fluid phases present, in the “reactions coupled” method, the number of primary equations (or variables) is $n_e + n_r$, and the number of secondary equations (or variables) is $n_f + 2$. In the “local reactions decoupled” method, the number of primary equations (or variables) is $n_e + n_{kf}$, and the number of secondary equations (or variables) is $n_{ks} + n_q + n_f + 2$. Recall that n_e is the number of elements, n_{kf} is the number of fluid kinetic reactions, n_{ks} is the number of solid kinetic reactions, n_q is the number of equilibrium reactions, and that there are $n_e + n_f + 2$ total equations and unknowns. It is of interest to note that when all reactions are local reactions, the second method will only have n_e primary variables. In some cases, n_e can be much smaller than $n_e + n_r$. As a result, the linear solution in the second approach will be much less expensive than in the first approach.

Implementation procedure

The reduction of the full set of equations to primary equations is performed at the Jacobian level. In order to minimize the code complexity, the two approaches described above are implemented in the same work flow, as shown in Figure 2.2. In both approaches, we first decouple the phase equilibrium and constraint equations and construct a Schur complement of the full Jacobian matrix \mathbf{J} in (2.58). This step treats (2.19), (2.23), (2.25) and (2.26) as primary equations and (2.27) and (2.28) as secondary equations. Only in the second (“local reactions decoupled”) approach do we perform an additional Schur complement construction procedure. The second step is essentially the same as the first step except we now treat (2.19) and (2.23) as primary equations, and (2.25) and (2.26) as secondary equations. Thus, these two steps share the same code and reduction procedures, which we now describe.

The set of equations to be reduced is divided into primary equations \mathbf{F}_p and secondary equations \mathbf{F}_s :

$$\mathbf{F}(\mathbf{x}) = \begin{bmatrix} \mathbf{F}_p(\mathbf{x}) \\ \mathbf{F}_s(\mathbf{x}) \end{bmatrix} = \mathbf{0}. \quad (2.60)$$

Correspondingly, we can split the unknowns into primary variables and secondary variables:

$$\mathbf{x} = \begin{bmatrix} \mathbf{x}_p \\ \mathbf{x}_s \end{bmatrix}. \quad (2.61)$$

In the simulator, the transport terms are treated using a connection list. In the two-point flux approach, which is applied here, each connection involves two blocks, and

the transmissibility at the block interface. The benefit of using a connection list is that one can treat structured or unstructured grids, in 1-D, 2-D or 3-D problems, in a consistent manner. An example of a connection is shown in Figure 2.3.

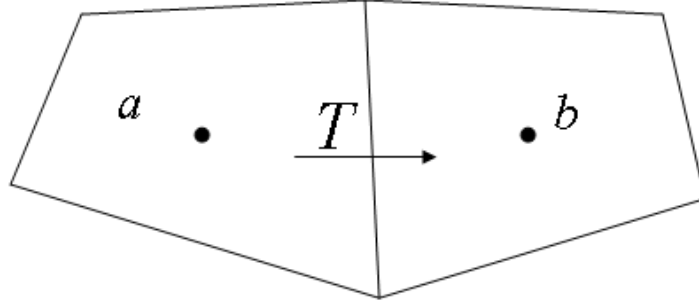


Figure 2.3: Illustration of one connection involving blocks a and b and one interface.

We now consider a single connection and describe how the reduction is accomplished. In the simulator, we loop through the connection list and perform the same reduction process for each connection. We first define twelve matrices:

$$\begin{aligned} \mathbf{A}_{11} &= \frac{\partial \mathbf{F}_p^a}{\partial \mathbf{x}_p^a}, & \mathbf{B}_{11} &= \frac{\partial \mathbf{F}_p^a}{\partial \mathbf{x}_s^a}, & \mathbf{C}_{11} &= \frac{\partial \mathbf{F}_s^a}{\partial \mathbf{x}_p^a}, & \mathbf{D}_{11} &= \frac{\partial \mathbf{F}_s^a}{\partial \mathbf{x}_s^a}, \\ \mathbf{A}_{22} &= \frac{\partial \mathbf{F}_p^b}{\partial \mathbf{x}_p^b}, & \mathbf{B}_{22} &= \frac{\partial \mathbf{F}_p^b}{\partial \mathbf{x}_s^b}, & \mathbf{C}_{22} &= \frac{\partial \mathbf{F}_s^b}{\partial \mathbf{x}_p^b}, & \mathbf{D}_{22} &= \frac{\partial \mathbf{F}_s^b}{\partial \mathbf{x}_s^b}, \\ \mathbf{A}_{12} &= \frac{\partial \mathbf{F}_p^a}{\partial \mathbf{x}_p^b}, & \mathbf{B}_{12} &= \frac{\partial \mathbf{F}_p^a}{\partial \mathbf{x}_s^b}, & \mathbf{A}_{21} &= \frac{\partial \mathbf{F}_p^b}{\partial \mathbf{x}_p^a}, & \mathbf{B}_{21} &= \frac{\partial \mathbf{F}_p^b}{\partial \mathbf{x}_s^a}, \end{aligned}$$

where \mathbf{F}_p^a are the primary equations written for block a , \mathbf{x}_p^a are the primary variables for block a , etc. With these matrices, we can write the portion of the Jacobian matrix

\mathbf{J} related to one connection as:

$$\begin{bmatrix} \mathbf{A}_{11} & \mathbf{B}_{11} & \mathbf{A}_{12} & \mathbf{B}_{12} \\ \mathbf{C}_{11} & \mathbf{D}_{11} & \mathbf{0} & \mathbf{0} \\ \mathbf{A}_{21} & \mathbf{B}_{21} & \mathbf{A}_{22} & \mathbf{B}_{22} \\ \mathbf{0} & \mathbf{0} & \mathbf{C}_{22} & \mathbf{D}_{22} \end{bmatrix} \begin{bmatrix} \delta \mathbf{x}_p^a \\ \delta \mathbf{x}_s^a \\ \delta \mathbf{x}_p^b \\ \delta \mathbf{x}_s^b \end{bmatrix} = - \begin{bmatrix} \mathbf{F}_p^a \\ \mathbf{F}_s^a \\ \mathbf{F}_p^b \\ \mathbf{F}_s^b \end{bmatrix}. \quad (2.62)$$

Note that $\mathbf{C}_{12} = \mathbf{D}_{12} = \mathbf{C}_{21} = \mathbf{D}_{21} = \mathbf{0}$ because the secondary equations for block a are only functions of variables in block a , so derivatives of \mathbf{F}_s^a with respect to \mathbf{x}_p^b and \mathbf{x}_s^b are zero (and similarly for block b).

Gaussian elimination can be applied in order to eliminate all of the \mathbf{B} matrices. This procedure has been documented in detail in [10]. The inverses of matrices \mathbf{D}_{11} and \mathbf{D}_{22} are calculated and a linear transformation is performed to the first and third rows in (2.62). Specifically,

$$\begin{aligned} \text{row}_1 &\leftarrow \text{row}_1 - \mathbf{B}_{11}\mathbf{D}_{11}^{-1} \cdot \text{row}_2 - \mathbf{B}_{12}\mathbf{D}_{22}^{-1} \cdot \text{row}_4, \\ \text{row}_3 &\leftarrow \text{row}_3 - \mathbf{B}_{21}\mathbf{D}_{11}^{-1} \cdot \text{row}_2 - \mathbf{B}_{22}\mathbf{D}_{22}^{-1} \cdot \text{row}_4. \end{aligned}$$

As a result, we obtain a linear system that is equivalent to (2.62):

$$\begin{bmatrix} \bar{\mathbf{A}}_{11} & \mathbf{0} & \bar{\mathbf{A}}_{12} & \mathbf{0} \\ \mathbf{C}_{11} & \mathbf{D}_{11} & \mathbf{0} & \mathbf{0} \\ \bar{\mathbf{A}}_{21} & \mathbf{0} & \bar{\mathbf{A}}_{22} & \mathbf{0} \\ \mathbf{0} & \mathbf{0} & \mathbf{C}_{22} & \mathbf{D}_{22} \end{bmatrix} \begin{bmatrix} \delta \mathbf{x}_p^a \\ \delta \mathbf{x}_s^a \\ \delta \mathbf{x}_p^b \\ \delta \mathbf{x}_s^b \end{bmatrix} = - \begin{bmatrix} \bar{\mathbf{F}}_p^a \\ \mathbf{F}_s^a \\ \bar{\mathbf{F}}_p^b \\ \mathbf{F}_s^b \end{bmatrix}, \quad (2.63)$$

where the new submatrices are given by:

$$\bar{\mathbf{A}}_{11} = \mathbf{A}_{11} - \mathbf{B}_{11}(\mathbf{D}_{11}^{-1}\mathbf{C}_{11}), \quad (2.64)$$

$$\bar{\mathbf{A}}_{12} = \mathbf{A}_{12} - \mathbf{B}_{12}(\mathbf{D}_{22}^{-1}\mathbf{C}_{22}), \quad (2.65)$$

$$\bar{\mathbf{A}}_{21} = \mathbf{A}_{21} - \mathbf{B}_{21}(\mathbf{D}_{11}^{-1}\mathbf{C}_{11}), \quad (2.66)$$

$$\bar{\mathbf{A}}_{22} = \mathbf{A}_{22} - \mathbf{B}_{22}(\mathbf{D}_{22}^{-1}\mathbf{C}_{22}), \quad (2.67)$$

and

$$\bar{\mathbf{F}}_p^a = \mathbf{F}_p^a - \mathbf{B}_{11}(\mathbf{D}_{11}^{-1}\mathbf{F}_s^a) - \mathbf{B}_{12}(\mathbf{D}_{22}^{-1}\mathbf{F}_s^b), \quad (2.68)$$

$$\bar{\mathbf{F}}_p^b = \mathbf{F}_p^b - \mathbf{B}_{22}(\mathbf{D}_{22}^{-1}\mathbf{F}_s^b) - \mathbf{B}_{21}(\mathbf{D}_{11}^{-1}\mathbf{F}_s^a). \quad (2.69)$$

It is evident that, after Gaussian elimination, the primary equations are decoupled from the secondary equations. Thus we can first solve for the primary variables via:

$$\begin{bmatrix} \bar{\mathbf{A}}_{11} & \bar{\mathbf{A}}_{12} \\ \bar{\mathbf{A}}_{21} & \bar{\mathbf{A}}_{22} \end{bmatrix} \begin{bmatrix} \delta \mathbf{x}_p^a \\ \delta \mathbf{x}_p^b \end{bmatrix} = - \begin{bmatrix} \bar{\mathbf{F}}_p^a \\ \bar{\mathbf{F}}_p^b \end{bmatrix}. \quad (2.70)$$

The procedure above is performed for each block and each connection. If a block has multiple connections (which is typically the case), the procedure is performed for each of its connections. The resulting Jacobian matrix, consisting of only primary equations and variables, is a Schur complement to the original full Jacobian matrix \mathbf{J} shown in (2.58). We denote this Schur complement as $\bar{\mathbf{J}}$. The linear solver now only

needs to solve:

$$\bar{\mathbf{J}}\delta\mathbf{x}_p = -\bar{\mathbf{F}}_p(\mathbf{x}_p^v). \quad (2.71)$$

Once $\delta\mathbf{x}_p$ is obtained, the secondary variables can be updated block by block:

$$\delta\mathbf{x}_s^a = \mathbf{D}_{11}^{-1}(\mathbf{F}_s^a - \mathbf{C}_{11}\delta\mathbf{x}_p^a), \quad (2.72)$$

$$\delta\mathbf{x}_s^b = \mathbf{D}_{22}^{-1}(\mathbf{F}_s^b - \mathbf{C}_{22}\delta\mathbf{x}_p^b). \quad (2.73)$$

Illustration of reduction procedure

We now use a simple example to illustrate the reduction process. We have five species, O_2 , H_2O , H_2 , CO_2 , and CO , and two independent reactions, $2\text{CO} + \text{O}_2 \longleftrightarrow 2\text{CO}_2$ and $\text{CO} + \text{H}_2\text{O} \longleftrightarrow \text{CO}_2 + \text{H}_2$. We assume the first reaction is a kinetic reaction and the second reaction is an equilibrium reaction. The kinetic rate of the first reaction is denoted as r , and the equilibrium constant for the second reaction is Q . For the sake of simplicity, we use subscript numbers 1 through 5 to represent each species, ordered as above. The full set of equations described by (2.19)-(2.28) for this case becomes:

$$\frac{\partial(N_4 + N_5)}{\partial t} + (L_4 + L_5) = 0, \quad (2.74)$$

$$\frac{\partial(2N_2 + 2N_3)}{\partial t} + (2L_2 + 2L_3) = 0, \quad (2.75)$$

$$\frac{\partial(2N_1 + N_2 + 2N_4 + N_5)}{\partial t} + (2L_1 + L_2 + 2L_4 + L_5) = 0, \quad (2.76)$$

$$\frac{\partial N_1}{\partial t} + L_1 - r = 0, \quad (2.77)$$

$$\frac{C_3 C_4}{C_2 C_5} - Q = 0, \quad (2.78)$$

and

$$f_1^g - f_1^l = f_2^g - f_2^l = f_3^g - f_3^l = f_4^g - f_4^l = f_5^g - f_5^l = 0, \quad (2.79)$$

$$X_{1g} + X_{2g} + X_{3g} + X_{4g} + X_{5g} - 1 = 0, \quad (2.80)$$

$$X_{1l} + X_{2l} + X_{3l} + X_{4l} + X_{5l} - 1 = 0. \quad (2.81)$$

Here (2.74)-(2.76) are element conservation equations for C, H and O, (2.77) is the reaction relation for the first reaction, (2.78) is the reaction relation for the second reaction, (2.79) are phase equilibrium relations, and (2.80)-(2.81) are phase constraint equations. There are thus 12 equations for each block. The number of unknowns for each block is also 12:

$$\mathbf{x} = (p, S_g, X_{1g}, X_{2g}, X_{3g}, X_{4g}, X_{5g}, X_{1l}, X_{2l}, X_{3l}, X_{4l}, X_{5l})^T.$$

If the “reactions coupled” method is applied, equations (2.74)-(2.78) are treated as primary equations. Correspondingly, the primary variables are selected as the first five unknowns, p , S_g , X_{1g} , X_{2g} , and X_{3g} . If the “local reactions decoupled” method is used, we can further decouple the equilibrium reaction relation, which means we shift (2.78) to the secondary equations. There are now only four primary variables: p , S_g , X_{1g} , and X_{2g} . We note that if the gas phase disappears, these primary variables will be adjusted accordingly (see [10] for details).

2.3.3 Solution strategies

The performance of the simulator when modeling chemical reactions is strongly affected by the convergence of Newton’s method and the linear solver. In our discussion below, we consider the convergence performance of the linear solver as the linear aspect of the problem. By contrast, we consider the convergence performance of Newton’s method as the nonlinear aspect of the problem.

We now first consider the linear aspect of the solution strategy. As the problem size grows, the size of the linear system grows proportionally. Iterative solvers must be applied for large problems. The generalized minimum residual solver (GMRES) has been widely used in reservoir simulation [55]. It guarantees convergence within a limited number of iterations. Our numerical experiments show that the blockwise GMRES solver provides a reliable and efficient solution technique for general multiphase reactive-transport problems. Furthermore, for large linear systems, preconditioning is essential for iterative solvers. In GPRS, a number of preconditioners are available. Full documentation of the available preconditioners is provided in [26]. We chose two of the preconditioners compatible with blockwise GMRES for testing. The first preconditioner is blockwise incomplete lower-upper factorization (BILU(0)). The BILU(0) preconditioner was implemented with the same algorithm used for incomplete lower-upper factorization (ILU), which has been used effectively with many iterative solvers [54]. The second preconditioner is based on the two-stage, constrained pressure residual (CPR) approach [63]. We will present comparisons of the performance of these two preconditioners in Section 2.4.

The nonlinear aspect of the solution is due to the convergence performance of Newton’s method. The convergence criteria for Newton iterations in multiphase

reactive-transport simulations are mostly the same as those used in compositional reservoir simulation. In general compositional simulation without chemical reactions, the simulator checks the relative change of the mass of any species in each block over a time step. With chemical reactions, by contrast, we perform mass balance check for elements. When the mass change of any element in any block over a time step is less than a prescribed limit, we consider it converged. To ensure stable modeling, we also check the relative changes of all of the unknowns, including pressure, saturations, and mole fractions. This is consistent with standard practice in compositional reservoir simulation.

2.3.4 Computational complexity of coupled and decoupled formulations

We now consider the computational complexity of the coupled and decoupled formulations. The total CPU cost τ for either approach per Newton iteration consists of three major components, the time to calculate properties τ_{prop} , the time to construct and reduce the Jacobian matrix τ_{Jac} , and the time to solve the resulting linear system τ_{solver} :

$$\tau = \tau_{prop} + \tau_{Jac} + \tau_{solver}. \quad (2.82)$$

We do not include overhead (e.g., input and output, initialization) in this discussion, as the associated CPU cost is small. The Jacobian construction time can be further

decomposed to:

$$\tau_{Jac} = \tau_{full} + \tau_{dec}^A + \tau_{dec}^B, \quad (2.83)$$

where τ_{full} is the time to construct the full Jacobian matrix, τ_{dec}^A is the time to decouple the phase equilibrium relations, and τ_{dec}^B is the time to decouple the localized reactions. Note that τ_{dec}^B is equal to zero in the reaction coupled approach. Thus, we have:

$$\tau = \tau_{prop} + (\tau_{full} + \tau_{dec}^A + \tau_{dec}^B) + \tau_{solver}. \quad (2.84)$$

If we solve a given problem with both the coupled and decoupled approaches described in Section 2.3.2, the values for τ_{prop} , τ_{full} , τ_{dec}^A are essentially the same for the two approaches. Thus, the difference in timing for the two methods $\Delta\tau$ involves only τ_{dec}^B and τ_{solver} :

$$\Delta\tau = (\tau_{solver})_{rc} - (\tau_{dec}^B + \tau_{solver})_{rd}, \quad (2.85)$$

where the subscript ‘rc’ designates reaction coupled, and ‘rd’ indicates reaction decoupled. We consistently observe $\Delta\tau$ to be positive; i.e., the decoupled formulation runs faster than the coupled method. This can be explained as follows.

First, the size of the linear system in the decoupled method is smaller than that in the coupled method. Specifically, $N_{rc} = n_b n_c$, and $N_{rd} = n_b(n_c - n_{kf} - n_q)$, where N is the number of linear equations solved at each iteration, and n_b is the number of blocks. Given that τ_{solver} is generally proportional to N^θ , where θ is a value typically between 1.1 and 2, it is evident that $(\tau_{solver})_{rd}$ will be much less than $(\tau_{solver})_{rc}$. Some

of this advantage is lost, however, because of τ_{dec}^B in the reactions decoupled approach. It is important to note that $\tau_{dec}^B \sim N_{rd}$; i.e., these operations are linear in N . Thus, the reactions decoupled procedure replaces some amount of computation that scales super-linearly with problem size with computation that scales linearly.

In addition, the linear solution in the reactions decoupled procedure is more robust, which results in fewer convergence problems and, as a result, fewer time step cuts. Consistent with these calculations, the reactions decoupled approach will be shown to require less computation time in the examples in Section 2.4.2.

2.4 Numerical examples

We now present two numerical examples. The first example shows that the solution of a kinetic system converges to an equilibrium system as the kinetic rate increases to a sufficiently large value. The second example demonstrates the application of the formulation described above to CO_2 mineralization processes in deep saline aquifers. For this example, we test various combinations of the numerical treatments.

2.4.1 Kinetic versus equilibrium reactions

Every reaction is essentially a reversible kinetic reaction. Thus it is conceptually allowable to model every reaction as a kinetic reaction. However, such an approach requires all of the data for every reaction mechanism, which is commonly very complex and frequently unavailable. In practice, depending on the time scale of interest, reactions are divided into two groups, equilibrium and kinetic reactions. When modeling reactive-transport problems, it is very useful for the modeler to have sufficient

prior knowledge to enable the classification of all of the reactions. Often, but not always, such a classification is clear to the modeler. We now present an example that illustrates the effects of classification of kinetic reactions and equilibrium reactions on the results.

We consider a batch reactor (modeled using a single grid block) containing two species, CO_2 and N_2 , in the gas phase. There is a sufficient amount of solid in the batch system to selectively adsorb or desorb CO_2 . We model the process of adsorption and desorption as a reversible reaction:



where $\text{CO}_2(\text{g})$ represents free CO_2 in the gas phase, $\text{CO}_2(\text{s})$ represents adsorbed CO_2 in the solid, and the reaction rate is defined as:

$$r = K \left(C_{\text{CO}_2(\text{g})} - C_{\text{CO}_2(\text{s})} \right). \quad (2.87)$$

This reaction in effect drives the concentrations of $\text{CO}_2(\text{g})$ and $\text{CO}_2(\text{s})$ to be the same. When there is more CO_2 in the gas phase, the reaction rate is positive and more $\text{CO}_2(\text{g})$ will convert to $\text{CO}_2(\text{s})$. Similarly, when there is more CO_2 in the solid phase, the reaction rate is negative, and the excessive $\text{CO}_2(\text{s})$ will convert to $\text{CO}_2(\text{g})$. Eventually, the rate approaches zero and the concentrations of $\text{CO}_2(\text{g})$ and $\text{CO}_2(\text{s})$ will be equal. The reaction in (2.86) can also be modeled as an equilibrium reaction, which forces the concentrations of $\text{CO}_2(\text{g})$ and $\text{CO}_2(\text{s})$ to be the same:

$$\frac{C_{\text{CO}_2(\text{g})}}{C_{\text{CO}_2(\text{s})}} = 1. \quad (2.88)$$

We now model (2.86) as both an equilibrium and a kinetic reaction at various kinetic rates. The initial condition is an equilibrium state between $\text{CO}_2(\text{g})$ and $\text{CO}_2(\text{s})$, both of which contain 2.7 moles of CO_2 . We then inject $\text{CO}_2(\text{g})$ at a constant rate of 5 mol/hr for 2.4 hours, after which the total CO_2 in the batch reactor is 17.4 moles. After injection stops, we allow the reversible reaction to occur for a sufficiently long time.

Figures 2.4(a) and 2.4(b) show the evolution of $\text{CO}_2(\text{g})$ and $\text{CO}_2(\text{s})$ with time. The lines with symbols represent the case in which we model the reaction as an equilibrium reaction, and the lines without symbols are the results at different kinetic rates. If the reaction is modeled as an equilibrium reaction, we observe that the amount of $\text{CO}_2(\text{g})$ and $\text{CO}_2(\text{s})$ are identical throughout the entire simulation. If the reaction is modeled as a kinetic reaction, some amount of time is required for the system to return to equilibrium. As expected, the smaller the reaction constant, the more time it takes for $\text{CO}_2(\text{g})$ and $\text{CO}_2(\text{s})$ to reach equilibrium. When the kinetic rate constant is $10^{-2}/\text{s}$, the results are indistinguishable from those in the equilibrium case.

From the results, it is evident that the reaction can be treated as equilibrium if $K \geq 10^{-2}/\text{s}$. The benefit of treating a fast reaction as an equilibrium reaction is that we no longer need to track the reaction rate at each iteration. In addition, because equilibrium reactions are considered as local reactions, they can be decoupled from the conservation equations, as described in Section 2.3.2. However, if the modeler chooses to classify the reaction as an equilibrium reaction, it is clear that it can still be safely treated as a kinetic reaction.

The time step sizes and the number of Newton iterations are shown in Figure 2.5. Figure 2.5(a) shows that the time stepping is essentially the same for the various cases.

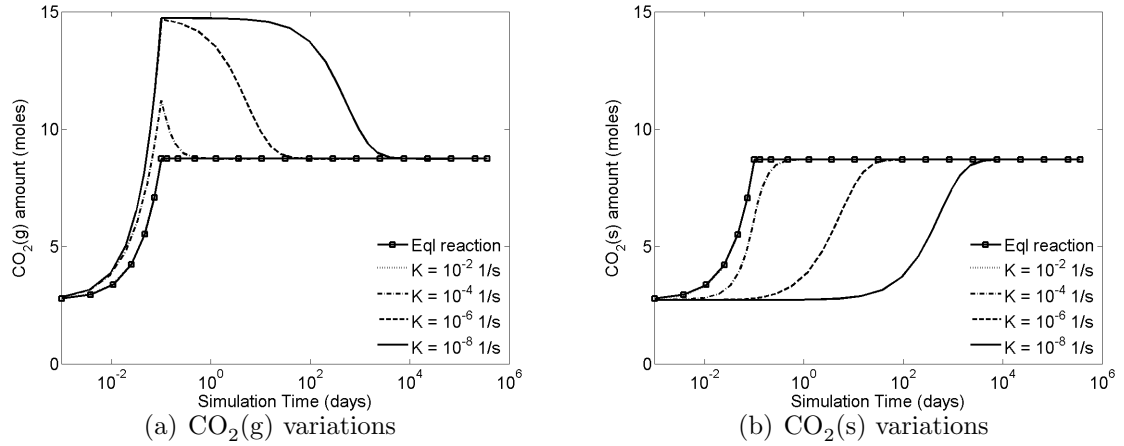


Figure 2.4: $\text{CO}_2(\text{g})$ and $\text{CO}_2(\text{s})$ variation with time for different runs. Lines with symbols are results if the reaction (2.86) is modeled as an equilibrium reaction. Lines without symbols are the cases when (2.86) is modeled as a kinetic reaction.

Figure 2.5(b) shows that the number of total Newton iterations varies over only about a factor of two, even though K varies by six orders of magnitudes. It is important to note, however, that the relation between the number of Newton iterations and the magnitude of kinetic rates is case dependent. Finally, it is also of interest to note that if the modeler chooses to represent this reaction as a kinetic reaction with $K = 10^{-2}/\text{s}$, correct results will be obtained with only a small increase in the number of Newton iterations.

2.4.2 Application to carbon mineralization

This example is designed to model geochemical trapping of CO_2 following CO_2 injection into saline aquifers. Geochemical trapping of CO_2 in mineral form is considered to be the most stable long-term storage mechanism for geologically sequestered CO_2 [46]. The CO_2 mineralization process in saline aquifers involves a large number of species and chemical reactions. The resulting Jacobian matrix is generally more

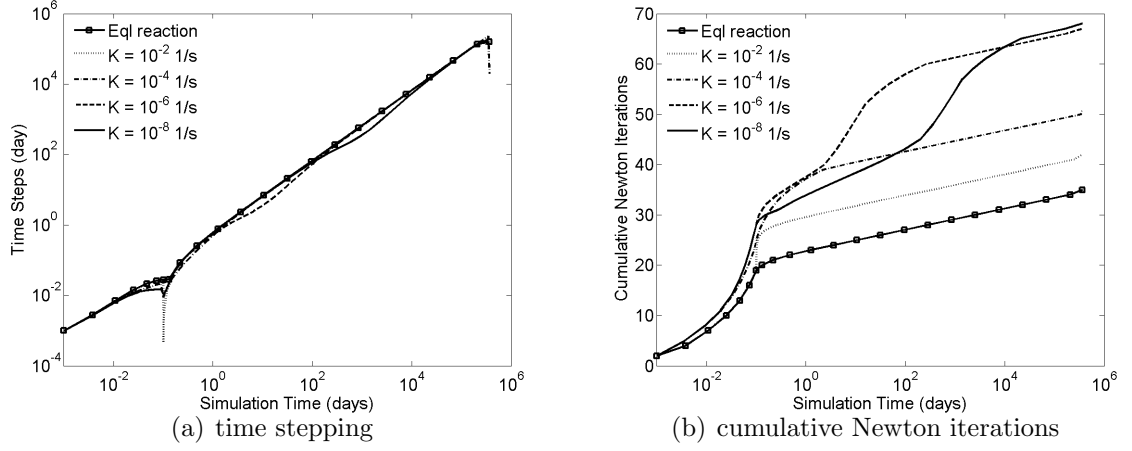


Figure 2.5: Time step sizes and cumulative Newton iterations for various runs.

complex than that for compositional simulations. To observe effective CO_2 mineralization, the modeling time must typically be on the order of 10^3 years. Therefore, computational efficiency is essential. In this section, we first describe the example base case. Then we will demonstrate the importance of a fast preconditioner, and present the long-term CO_2 mineralization results. Finally, we discuss the effect of mineral selection on model performance.

Model description

We developed a 2D rectangular cross-sectional (x - z) model to simulate CO_2 injection into saline aquifers. The model represents a saline aquifer that is 1 km in the x direction, 10 m in y , and 100 m in z . The model contains 100 grid blocks in x and 50 in z . We apply no-flow boundary conditions. The model contains one injection well perforated in a single grid block located 25 m from the top of the aquifer (see Figure 2.8(a)). A pure CO_2 stream is injected at a constant bottom hole pressure of 24.5 MPa (3553 psi) for one year. Under reservoir conditions, the injected CO_2 forms a

supercritical phase, which we refer to as the gas phase. The aquifer is initially filled with saline water, which constitutes the liquid phase. During the injection period, as the gas phase displaces the liquid phase near the injector, a small amount of CO_2 dissolves into the liquid phase, though most of the CO_2 remains in the gas phase. After injection stops, the CO_2 migrates to the top of the reservoir to form a thin gas phase layer, where it gradually dissolves into the liquid phase. Because the water with dissolved CO_2 is more dense than that without CO_2 , the water with dissolved CO_2 begins to settle under gravity. This process occurs very slowly, so the simulation must be run out to long times.

Geochemical reactions, which occur between the dissolved CO_2 , water, ions and minerals, were determined based on [61]. In the first set of runs (base case), we model 21 species, specifically CO_2 and H_2O , 11 ions and eight minerals. There are nine elements involved in these reactions. All of the reactions included in the simulation are summarized in Table 2.3. The chemical formulas for the minerals are provided in Table 2.4. According to [42], we treat the reactions involving only aqueous species as equilibrium reactions and those involving minerals as kinetic reactions. With reference to Table 2.3, reactions (1), (2), (3) and (4) are treated as equilibrium reactions, while the remainder are treated as kinetic reactions. The activities of ions, used in both equilibrium and kinetic reactions, are calculated using the B-dot model, as described in (2.50). The mineral precipitation and dissolution rates are calculated based on the kinetic laws in [42]. The parameters required for mineral reactions, shown in Table 2.4, are taken from [61].

We perform the simulation under isothermal conditions. The temperature of the reservoir is 50°C . Initial pressure at the top of the reservoir is 11.8 MPa. The aquifer

Table 2.3: Chemical reactions for CO₂ mineralization

No.	Reaction
(1)	$\text{CO}_2(\text{aq}) + \text{H}_2\text{O} = \text{H}^+ + \text{HCO}_3^-$
(2)	$\text{CO}_3^{--} + \text{H}^+ = \text{HCO}_3^-$
(3)	$\text{OH}^- + \text{H}^+ = \text{H}_2\text{O}$
(4)	$\text{Al}(\text{OH})_2^+ + 2 \text{H}^+ = \text{Al}^{+++} + 2 \text{H}_2\text{O}$
(5)	$\text{Annite} + 10 \text{H}^+ = 3 \text{Fe}^{++} + 3 \text{SiO}_2(\text{aq}) + \text{Al}^{+++} + 6 \text{H}_2\text{O} + \text{K}^+$
(6)	$\text{Anorthite} + 8 \text{H}^+ = 4 \text{H}_2\text{O} + \text{Ca}^{++} + 2 \text{Al}^{+++} + 2 \text{SiO}_2(\text{aq})$
(7)	$\text{Calcite} + \text{H}^+ = \text{Ca}^{++} + \text{HCO}_3^-$
(8)	$\text{Chalcedony} = \text{SiO}_2(\text{aq})$
(9)	$\text{Dolomite} + 2 \text{H}^+ = \text{Ca}^{++} + \text{Mg}^{++} + 2 \text{HCO}_3^-$
(10)	$\text{Illite} + 8 \text{H}^+ = 5 \text{H}_2\text{O} + 0.6 \text{K}^+ + 0.25 \text{Mg}^{++} + 2.3 \text{Al}^{+++} + 3.5 \text{SiO}_2(\text{aq})$
(11)	$\text{Kaolinite} + 6 \text{H}^+ = 5 \text{H}_2\text{O} + 2 \text{Al}^{+++} + 2 \text{SiO}_2(\text{aq})$
(12)	$\text{Siderite} + \text{H}^+ = \text{HCO}_3^- + \text{Fe}^{++}$

Table 2.4: Mineral formula, precipitation and dissolution parameters

Mineral	Formula	$\log_{10}(K)$ (mol/m ² /s)	Surf. Area (m ² /m ³)	$\log_{10}(K_{\text{eq}})$
Annite	$\text{AlKFe}_3\text{Si}_3\text{O}_{10}(\text{OH})_2$	-14.0	4400	28.61
Anorthite	$\text{CaAl}_2\text{Si}_2\text{O}_8$	-12.0	88	25.82
Calcite	CaCO_3	-8.80	88	1.60
Chalcedony	SiO_2	-13.9	7128	-3.62
Dolomite	$\text{CaMg}(\text{CO}_3)_2$	-9.22	88	2.25
Illite	$\text{Mg}_{0.25}\text{K}_{0.6}\text{Al}_{2.3}\text{Si}_{3.5}\text{O}_{12}\text{H}_2$	-14.0	26400	9.07
Kaolinite	$\text{Al}_2\text{Si}_2\text{O}_5(\text{OH})_4$	-13.0	17600	6.82
Siderite	FeCO_3	-9.22	88	-0.37

is modeled as a homogeneous porous medium with constant porosity of 0.18 and constant isotropic permeability of 100 md. The phase equilibrium between the gas and liquid phases is represented using the Peng-Robinson equation of state. After one year of injection at a bottom hole pressure of 24.5 MPa, the well injected a total of 1389.6 metric tons of CO_2 . For our first study, we simulate for five years (including four years of post-injection period) with different combinations of preconditioners and coupling methods. Next we use the most efficient procedure to simulate this model for 500 years (one year of injection and 499 years of post-injection period).

Assessment of solution methods

The full set of governing equations contains nine element conservation equations, 12 reaction relations, 2 phase equilibrium relations for both CO_2 and H_2O , and two phase constraints for gas and liquid phases. As discussed in Section 2.3, there are two methods we can use to reduce the size of the resulting linear system. In the “reactions coupled” method, all of the reaction relations are coupled with element conservation equations. The number of primary equations (and variables) is 21. In the “local reactions decoupled” method, we can decouple the localized reactions. In our model, because all reactions are equilibrium and mineral kinetic reactions, we can decouple them from the conservation equations. Therefore, the number of primary equations (and variables) is the same as the number of elements, which is nine in this case.

The blockwise GMRES iterative solver with different preconditioners is used to solve the linear system. We tested both the BILU(0) and CPR preconditioners for both the “reactions coupled” and “local reaction decoupled” methods. Figure 2.6

compares the CPU cost for each combination versus simulation time. In our results, the total CPU time is the sum of the linear solver time, Jacobian construction time (time to build the Jacobian matrix \mathbf{J} and to reduce it to $\bar{\mathbf{J}}$) and property calculation time (time to calculate phase and species properties). The overhead due to input and output are not included, because these typically account for less than 1% of the total simulation time in large problems.

Figure 2.6 clearly shows that the CPR preconditioner outperforms the BILU(0) preconditioner for both methods. This is consistent with observations for multiphase compositional simulations without chemical reactions [26]. With the BILU(0) preconditioner, at the end of the simulation, the solver time accounts for 88% of the total CPU cost in the “reactions coupled” method and 73% in the “local reactions decoupled” method. With the CPR preconditioner, the solver time only accounts for approximately one third of the total simulation time. Table 2.5 lists the performance data for the various runs. We can see that the BILU(0) preconditioning requires many more Newton iterations and linear solver iterations than the CPR preconditioned runs. The increase in Newton iterations occurs because the BILU(0) preconditioned GMRES solver fails from time to time, which forces the simulator to cut the time step. As a result, the number of time steps for BILU(0) is larger than that for CPR. Thus, the linear solver times for BILU(0) are much larger than those for CPR, regardless of whether or not the reaction relations are coupled.

We also note that the CPU cost of the decoupled runs is always less than that of coupled runs. As shown in Table 2.5, when the same preconditioner is used, the number of Newton iterations and solver iterations are very similar for the two methods. The major difference is in the linear solution time. If all of the reactions are

solved coupled with the conservation equations, each linear solution entails a matrix system of size $21n_b \times 21n_b$ in size, where n_b is the number of blocks. If the local reactions are decoupled from the conservation equations, the matrix is only $9n_b \times 9n_b$. Therefore, the linear solution of the decoupled Jacobian matrix requires less time. Because the amount of time required by the reduction procedure is less than the savings in the linear solution, decoupled approach is overall faster.

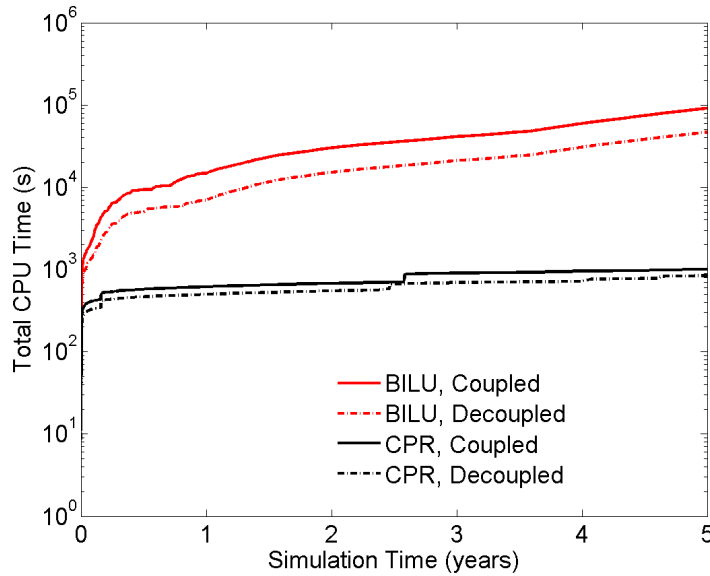


Figure 2.6: Total CPU time for various runs with BILU(0) preconditioners. Total CPU time plotted is the sum of linear solver time, Jacobian construction time, and property calculation time. Actual total CPU time includes overhead due to input and output.

We now simulate this model for a 500 year time frame. Based on the findings above, we apply the CPR preconditioner. Figure 2.7 shows the total CPU cost and its three major components—the solver time, Jacobian construction time, and the property calculation time. The decoupled method outperforms the coupled method, with the difference increasing with simulation time. The major gain is in the linear

solver time. At the end of 500 years, the linear solver time for the decoupled run is 67% less than that for the coupled run. As expected, Jacobian construction time for the decoupled case is more than that for the coupled run because of the extra CPU cost required to decouple the local reactions. Overall, the decoupled method is more appealing, as the Jacobian construction and property calculation are easier to parallelize than the linear solver for very large problems.

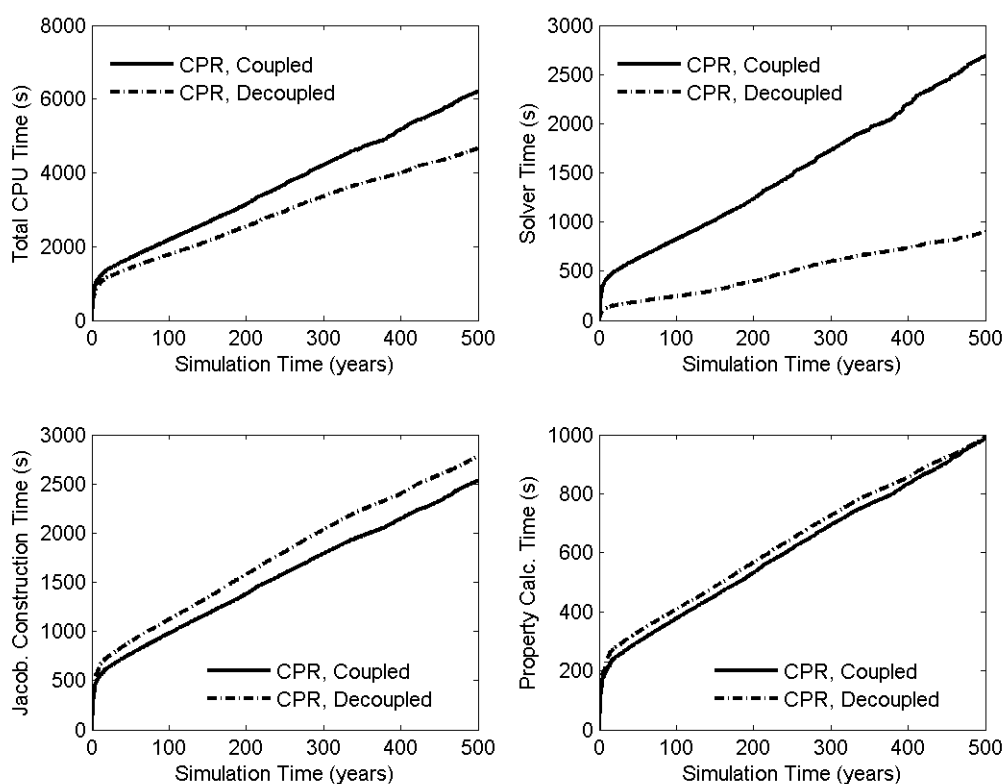


Figure 2.7: CPU time breakdown for 500 year runs with CPR preconditioner. Total CPU time plotted is the sum of solver time, Jacobian construction time, and property calculation time. Actual total CPU time includes overhead due to input and output.

Table 2.5: Performance summary for carbon mineralization base case runs

	Simulated Time (yrs)	Newton Iterations	Solver Iterations	Solver Time (s)	Total Time (s)
BILU, coupled	5	1550	154165	80005.3	91260
BILU, decoupled	5	1520	152116	33981.7	46726
CPR, coupled	5	319	914	360	1006
CPR, decoupled	5	319	914	104	839
CPR, coupled	500	1962	12990	2688	6288
CPR, decoupled	500	1886	13268	897	4687

CO₂ mineralization results

We now present the CO₂ mineralization results for the 500 year simulation. Figure 2.8 shows the gas saturation and the mole fraction of dissolved CO₂ in the water phase at 5 years and 500 years. At 5 years, the injected CO₂ forms a plume as the gas phase rises to the top of the reservoir. The water is saturated with CO₂ in the blocks containing a free gas phase, as shown in Figure 2.8(c). At 500 years, most of the CO₂ has dissolved into water at the interface between the gas and water phases at the top of the reservoir. Figure 2.8(d) shows the saturated water with dissolved CO₂ slowly sinking toward the bottom of the reservoir.

Most mineral changes occur as the saturated water phase moves downward. At 500 years, noticeable precipitation or dissolution is observed for the eight simulated minerals. Annite, anorthite and illite dissolve into the liquid phase, and dolomite, calcite, kaolinite and siderite precipitate as a result of CO₂ injection. Chalcedony also changes because of silicate dissolution. Figure 2.9 shows the molar density changes of four representative minerals at 500 years.

Figure 2.10(a) shows the net changes of each mineral in the reservoir. We can

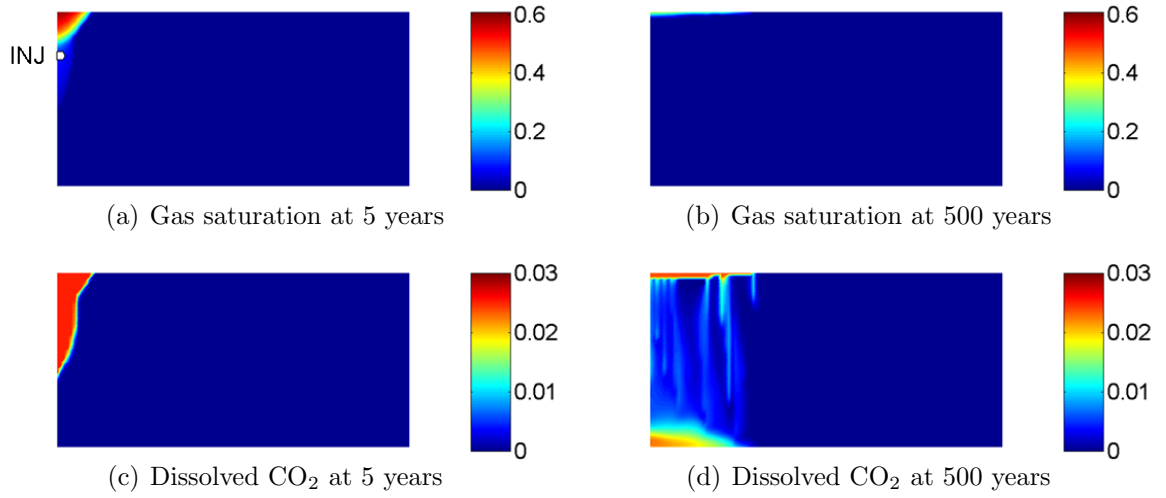


Figure 2.8: Gas saturations and dissolved CO_2 mole fractions in aqueous phase at 5 and 500 years.

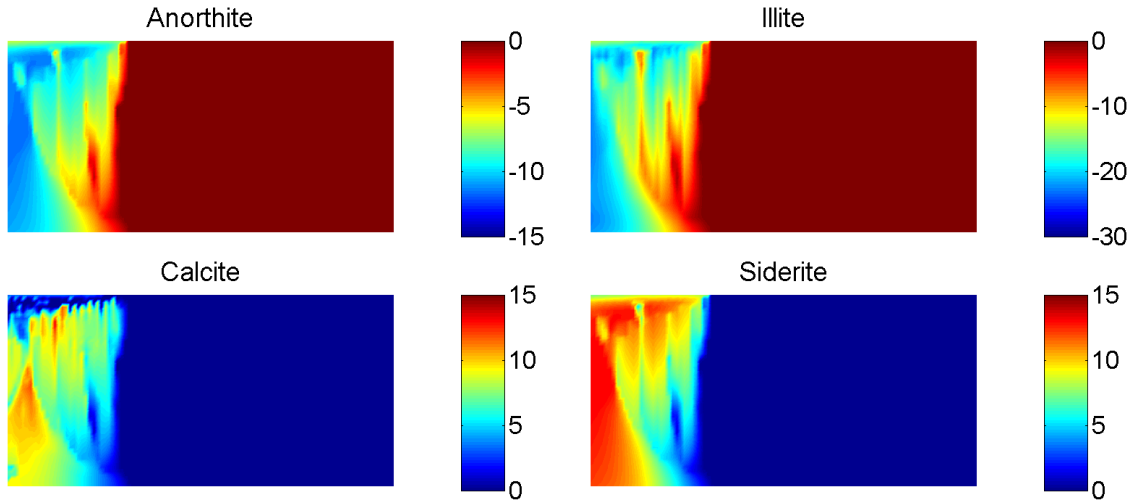


Figure 2.9: Selected mineral molar density changes at 500 years (mol/m^3). Positive values indicate precipitation, and negative values indicate dissolution.

see that the changes in the various minerals increase slowly at first, though they increase nearly linearly with time after about 250 years. It may not be appropriate to extrapolate these results out to later times, because continuous dissolution of silicates may result in the disappearance of specific minerals in some blocks. When

the mineralogy changes, the reaction pathway will also change.

Figure 2.10(b) shows the distribution of carbon over time. The amount of CO_2 in the gas phase decreases with time as CO_2 dissolves into water and reacts with ions and minerals. In the water phase, most of carbon remains in the molecular form of $\text{CO}_2(\text{l})$. At the end of 500 years, about 7.3% of the carbon is stored in ionic forms, HCO_3^- and CO_3^{--} . Mineralized carbon accounts for 22.4% of the injected CO_2 . This large percentage of mineralized CO_2 may be due to the enhanced reactive surface areas of the clay minerals (our data is from [61]). Accurate quantification of the reactive surface areas of minerals remains a challenge for geochemists, and the values used for these parameters in simulations can strongly impact mineralization results.

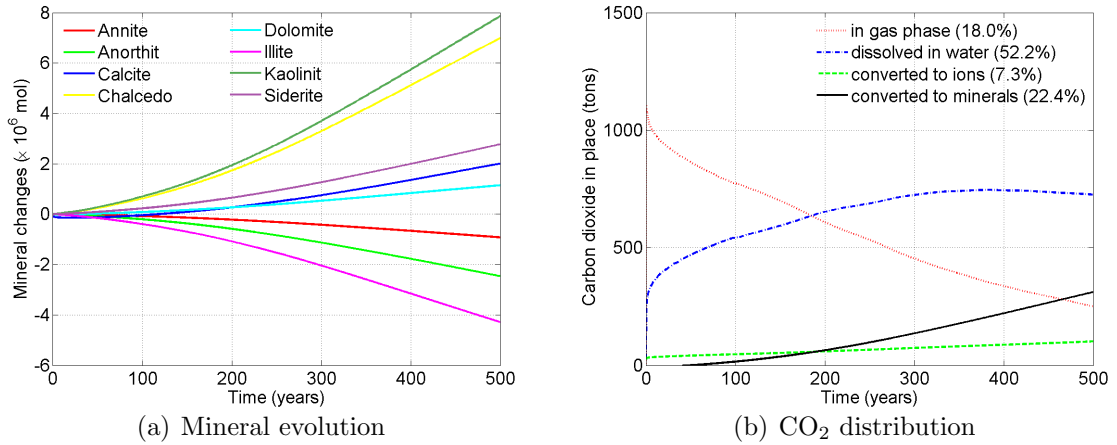


Figure 2.10: Mineral net molar changes and evolution of CO_2 in time.

Effect of mineral selection

We now assess the impact of mineral selection on simulation results and simulator performance. In the base case described above, we considered eight minerals. In practice, depending on the rock type, one might include more or fewer minerals. It

is of course desirable to include as few minerals as possible, as this will reduce both the number of ions and the number of reactions, which will lead to a reduction in computation time.

We now consider two additional cases. The first case contains three minerals, anorthite, calcite, and kaolinite. There are then six reactions (reactions (1), (2), (3), (6), (7) and (11) in Table 2.3). In the second case, we take calcite to be representative of a typical carbonate reservoir and consider only it. The reactions required for this model are further reduced to (1), (2), (3) and (7). The number of ions involved in these cases are seven and five, respectively. The total number of unknowns is 25 for the base case, 16 for the three-mineral case and 12 for the one-mineral case. The other model parameters are the same as those used in the base case.

Figure 2.11 and Table 2.6 present the carbon distribution over time for the three-mineral and one-mineral cases. In both cases, the trendlines of the gaseous CO_2 and dissolved CO_2 are similar to the base case. At 500 years, the mineralized carbon in the three-mineral case is 6.07%, which is significantly less than that in the base case (22.4%). The aqueous phase carbon is higher than the base case. In the one-mineral case, more CO_2 dissolves into the water phase than in the other cases. At 500 years, -1.85% for carbon uptake by calcite indicates that the injection of CO_2 actually promotes calcite dissolution. At 500 days, only 7.88% of the injected carbon is in the gas phase.

Table 2.7 presents the performance data for these cases together with the base case. We observe that the total CPU time is quite sensitive to the number of minerals modeled. For all cases, the decoupled method is consistently faster than the coupled method. Similar to the base case, the major gain is from the solver time. These allow

us to estimate values for the θ parameter described in Section 2.3.4. Specifically, the solver time per Newton iteration is proportional to $N_{rc}^{1.77}$ in the coupled approach, and to $N_{rd}^{1.27}$ in the decoupled approach. Note that these scaling include the effect of lack of convergence by the linear solver. These scalings explain the advantage of the decoupled method for more large and complex models.

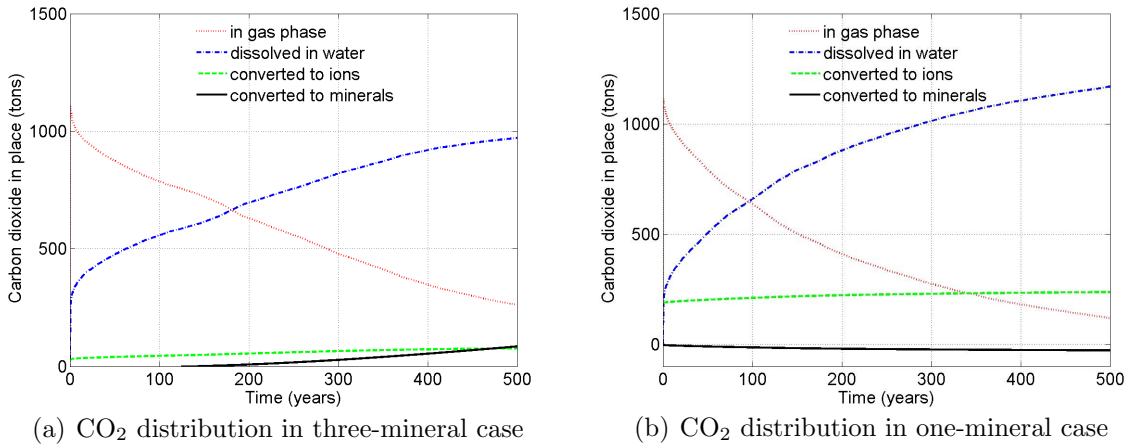
Figure 2.11: CO₂ evolution in time.

Table 2.6: Final carbon distribution in various phases at 500 years

	C in CO ₂ (g)	C in CO ₂ (aq)	C in Ions	C in Minerals
Base case	18.05 %	52.22 %	7.32 %	22.41%
Three-mineral case	18.68 %	69.77 %	5.48 %	6.07 %
One-mineral case	7.88 %	78.14 %	15.83 %	-1.85 %

2.5 Concluding remarks

In this chapter, we developed an element-based formulation to model general chemical reactions coupled with subsurface flow. The conservation equations are written

Table 2.7: Impact of mineral selection on simulator performance

Cases	No. of Pri. Var.	Newton Iterations	Solver Iterations	Solver Time (s)	Total Time(s)
Base case, coupled	21	2160	13845	2689	6211
Base case, decoupled	9	2072	14104	856	4663
Three-mineral, coupled	12	1915	10590	667	1805
Three-mineral, decoupled	6	1882	11333	383	1554
One-mineral, coupled	8	1860	11056	432	1198
One-mineral, decoupled	4	1849	12275	271	1025

for each element, and thus the reaction terms do not appear in these equations. The implementation of chemical reactions is accomplished in a novel and generic manner that can be readily extended to a wide range of reaction mechanisms. The current modeling capability includes both homogeneous and heterogeneous reactions, equilibrium and kinetic reactions, and concentration and activity-based reactions. The reaction modeling modules have been built within the context of Stanford's General Purpose Research Simulator. The advanced features of GPRS (e.g., unstructured grids, multisegment wells, and CPR preconditioned blockwise GMRES solver) are compatible with the chemical reaction modeling capabilities.

We applied the formulation to model CO_2 mineralization problems. The BILU(0) preconditioned blockwise GMRES solver appears to be impractical for large-scale problems with a large number of species and reactions. Use of the CPR preconditioner provides a much faster solution method. By decoupling local reactions from the global conservation equations, we can achieve further reduction in the linear solution time and overall simulation time. The results presented here indicate that the benefits of this decoupling increase as more reactions are included.

Chapter 3

Modeling the In-situ Upgrading of Oil Shale

Oil shale is a highly abundant energy resource, though commercial production has yet to be realized. In this chapter we present detailed numerical simulations of the in-situ upgrading process. The key physical effects that must be represented in models of in-situ upgrading include strongly temperature-dependent kinetic reactions, fully-compositional flow and transport, and downhole heating. We apply a species-based formulation for this problem, because the elements in the reactions considered here are not balanced. After a relatively modest degree of parameter adjustment (with parameters restricted to physically realistic ranges), our results for oil and gas production will be shown to be in reasonable agreement with available field data. We then demonstrate how production is impacted by heater temperature and location. The ability to model these effects will be essential for the eventual design and optimization of in-situ upgrading operations.

3.1 Modeling techniques

The simulation of in-situ upgrading involves (primarily) the modeling of chemical kinetics, phase equilibrium between the gas and liquid phases, mass transport, and heat conduction. The chemical kinetics are highly temperature-dependent and thus are strongly coupled with both the mass and energy balance equations. The actual in-situ upgrading process is very complicated and there are some physical effects not incorporated in our model. These include geomechanical effects and porosity and permeability evolution (which occur as the kerogen decomposes). Rather than simulate these effects in detail, our model applies ‘average’ or ‘effective’ values for porosity and permeability. It may be useful to develop more sophisticated treatments for these effects in future work. We now describe the specific treatments included in the in-situ upgrading model.

3.1.1 Mass and energy balance equations

In Chapter 2, we presented the species mass balance equations for both fluid and solid species (2.4) and (2.5). The reactions involved in the in-situ upgrading processes are typically all kinetic reactions. We now rewrite (2.4), dropping the equilibrium reaction rates and also neglecting diffusion and dispersion (which are not included in the in-situ upgrading model):

$$F_i = \frac{\partial}{\partial t} \left[\phi \sum_j (S_j \rho_j X_{ij}) \right] + \nabla \cdot \sum_j (\rho_j X_{ij} \mathbf{u}_j) + q_i^W - \sum_k \nu_{i,k} r_k = 0, \quad (3.1)$$

where F_i represents the residual of the mass balance equation for fluid species i , ϕ is the porosity, S_j is the saturation of phase j , X_{ij} is the mole fraction of fluid species

i in phase j , k is the kinetic reaction index, $\nu_{i,k}$ is the total stoichiometric coefficient for component i in reaction k , r_k is the reaction rate of reaction k , \mathbf{u}_j is the Darcy velocity for phase j , ρ_j is the density of phase j , and q_i^W is the well rate of species i . These and the following variables are as defined in Chapter 2; the definitions are repeated here for completeness.

The Darcy velocity is given by:

$$\mathbf{u}_j = -\mathbf{K} \frac{k_{rj}}{\mu_j} (\nabla p_j - \gamma_j \nabla D), \quad (3.2)$$

where \mathbf{K} is the permeability tensor, k_{rj} is the relative permeability for phase j , μ_j is the viscosity of phase j , p_j is the pressure of phase j , $\gamma_j = \rho_j g / g_c$ (g is gravitational acceleration and g_c converts from lbm to lbf) and D is depth.

Similarly, we rewrite (2.5) without equilibrium reaction rates as:

$$F_s = \frac{\partial C_s}{\partial t} - \sum_k \bar{\nu}_{s,k} r_k = 0, \quad (3.3)$$

where C_s is the molar concentration of solid s and $\bar{\nu}_{s,k}$ is the total stoichiometric coefficient of solid s in reaction k . When modeling in-situ upgrading processes, kerogens are treated as solid components governed by (3.3). Some oil shale formations contain multiple types of kerogens and thus may require more than one solid mass balance equation. The simulator can treat chemical reactions involving multiple solid components, though for simplicity only one type of kerogen is modeled in this work.

In order to account for the effects of thermal convection and heat conduction, the energy balance equation for the system is required. The energy equation is given by

(adapted from [30]):

$$F_e = \frac{\partial}{\partial t} \left[\phi \left(\sum_j U_j \rho_j S_j \right) + (1 - \phi) U_R \right] - \nabla \cdot \left(\sum_j H_j \rho_j \mathbf{u}_j \right) - \nabla \cdot (\kappa \nabla T) + \sum_j H_j \rho_j q_j^W + q^H = 0, \quad (3.4)$$

where U_j is the internal energy for phase j , U_R is the internal energy of the rock, $H_j = \sum_i X_{ij} H_i$ is the enthalpy of phase j , κ is the thermal conductivity of oil shale, and q^H is the rate of energy input from downhole heaters. We do not include heat of reaction terms in (3.4), as these effects are very small relative to heat input [47].

3.1.2 Phase equilibrium and properties

Upon heating, the kerogen decomposes to a multi-component mixture. The mixture may contain non-condensable gases, hydrocarbons, water, and prechar. These components constitute at least four phases – a gas phase, an oil phase, a water phase and a solid prechar phase. In general, each phase is a mixture of multiple components, with the partitioning of the components between the phases described by thermodynamic relationships.

In this work, we assume that the prechar phase is created and retained in the solid phase. Therefore, the prechar phase is assumed not to occupy the pore space. Under this assumption, we do not need to consider the prechar in the transport equations. Although the water and oil phases are immiscible, water vapor and hydrocarbon gases are miscible. These assumptions together require that three-phase flash calculations be performed. Such flash calculations require significant computational effort and will impact the performance of our simulator. In typical in-situ upgrading processes,

however, the reactions of interest occur mostly above the boiling point of water. Also, if possible, water in the formation is produced prior to heating in order to avoid expending energy to heat and vaporize water. For these reasons, only gas-oil phase equilibrium is considered here. The gas phase may contain non-condensable gases and hydrocarbons while the oil phase may contain condensable gases and hydrocarbons. This treatment is reasonable when the amount of water produced during the in-situ upgrading process is small. If this is not the case, then the water phase (and three-phase calculations) must be included in the model.

Thermodynamic equilibrium requires the equality of component fugacities in the gas and oil phases determined by (2.27). The phase densities are calculated by the Peng-Robinson equation of state. The viscosity of the gas phase is modeled using a standard mixing rule for EOS calculation due to [28]. The viscosity of the oil phase is determined using the representation given by [40]:

$$\log_{10} \mu_o(T) = b \left(1 + \frac{T - 30}{303.15} \right)^{-s} + c, \quad (3.5)$$

where b , c and s are parameters evaluated from measurements for the oil under study. Note that T is here temperature in °C. In the simulations presented in this chapter, we use $b = 4.1228$, $s = 3.5640$ and $c = -3.002$.

3.1.3 Kinetic reactions

In this chapter, the reaction rate r_k in (3.1) is characterized by species concentrations. Considering reactions in which reactants can be either fluid components or solid components, and assuming that all reactions follow the elementary rate law, the

reaction rate (given previously in (2.37)) is

$$r_k = K_k \prod_{i,j} C_{ij}^{\nu_{ij,k}} \prod_s C_s^{\nu_{s,k}}. \quad (3.6)$$

The rate constant K_k is given by:

$$K_k = A_k \exp\left(-\frac{E_k}{k_B T}\right), \quad (3.7)$$

where E_k is the activation energy for reaction k , k_B is the Boltzmann constant, T is absolute temperature and A_k is the frequency factor for reaction k . The concentration of fluid component C_{ij} is given by $C_{ij} = \rho_j \phi S_j X_{ij}$.

In the in-situ upgrading process, the kinetic reactions and transport equations are coupled and solved within the Newton (nonlinear) iterations. Since the fluid component concentrations are expressed in terms of other variables in (2.39), when (3.1) is discretized, the fluid component concentrations are not represented directly. Nonetheless, at each Newton iteration, fluid component concentrations are updated, as are their derivatives with respect to the unknowns. In this way the kinetic reactions are fully coupled to the rest of the governing equations. The derivatives required to build the Jacobian matrix are presented in Section 2.2.2.

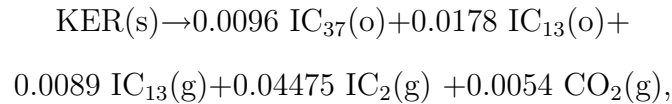
3.1.4 Reaction stoichiometry

Chemical reactions have been implemented in a generalized form in the simulator. Reactions can occur between components within a phase (gas, oil or solid) or between components in different phases. Because of this generality, our implementation requires a larger number of stoichiometric coefficients to be input than are required by

traditional treatments (e.g., STARS [37]). The advantage of our approach, however, is that it allows us to define reactions as occurring between particular components within specified phases.

Kerogen is a complex mixture of large carbon-number components. Following common practice, we represent it here in a ‘normalized’ form; i.e., in terms of a single carbon atom, with the number of atoms of other elements scaled appropriately. The specific formula applied here is $\text{CH}_{1.5}\text{N}_{0.026}\text{O}_{0.05}$, which was used by [7] to represent Green River oil shale kerogen. The model developed here can treat multiple types of kerogen and the initial richness of kerogen can vary in space. For simplicity, we considered just one type of kerogen in this work.

We now consider a decomposition reaction from kerogen (designated KER) to other fluid components:



where IC indicates lumped components (explained below). In this reaction, the total number of reactive fluid components is four and the number of reactive solid components is one. Note that $\text{IC}_{13}(\text{o})$ and $\text{IC}_{13}(\text{g})$ are treated separately for purposes of reaction modeling, though they are treated as the same fluid component in the transport equations. The stoichiometric coefficients corresponding to this reaction are listed in Table 3.1. We note that the maximum number of coefficients that can be specified for any reaction is $n_p n_f + n_s$. Recall that n_p is the number of fluid phases, n_f is the number of fluid species, and n_s is the number of solid species.

Table 3.1: Example of stoichiometric coefficient input

KER(s)	IC ₃₇ (o)	IC ₁₃ (o)	IC ₂ (o)	CO ₂ (o)	IC ₃₇ (g)	IC ₁₃ (g)	IC ₂ (g)	CO ₂ (g)
-1	0.0096	0.0178	0	0	0	0.0089	0.04475	0.0054

3.1.5 Heat injection

Heat injection is the key driving force for in-situ upgrading. In this work, consistent with the actual process, we specify that the downhole heaters operate at constant temperature. In practice, accurate control of downhole temperature is essential as the upgrading reactions are very sensitive to temperature. The constant temperature heaters are approximated here by specifying the initial temperature of grid blocks containing heaters to be the target heater temperature T_h . These blocks are also assigned very large specific heat capacities (e.g., 10^8 Btu/ft³/°F). Our results show that this is a reasonable approach for modeling constant temperature heaters, as the heater-block temperatures stay well within 1°F of T_h . A limitation of this treatment of heat injection is that we do not differentiate between heater temperature and heater block temperature (though grid blocks in our model are quite small, typically ~ 1 ft or less in areal dimension). In reality the heater temperature will be higher than the block temperature. Therefore, the appropriate value for T_h in our model may not coincide exactly with the value used in an actual field case. A more comprehensive treatment of heat injection will be required to model more complex heaters that can operate under a variety of settings.

To simulate heat convection and heat conduction, the model requires representations for thermal diffusivity and component enthalpy. The rate of heat conduction is

primarily determined by thermal diffusivity α , where $\alpha = \kappa/(\rho_R c_p)$. Here ρ_R is rock density and c_p is the specific heat capacity of the rock. Thermal conductivity κ is in general a function of oil shale grade and temperature, and ρ_R and c_p are functions of kerogen content. The values of both rock density ρ_R and the rock specific heat c_p decrease slightly when the formation is heated and kerogen decomposes to hydrocarbons [33]. For Green River oil shale that is rich in organic matter, the thermal conductivity was reported to vary between 3.5 and 8.7 Btu/ft/day/°F over the temperature range 170°F to 720°F [45]. In this work, we treat ρ_R and c_p as constants though we treat κ as a history-matching parameter which we allow to vary over the range 3.5-8.7 Btu/ft/day/°F. Thus our value for κ should be viewed as an average or ‘effective’ value. The data we are attempting to match is that reported for Shell’s pilot test, as discussed in the next section.

The enthalpy of each fluid component is represented as a function of temperature [48]:

$$H_i = H_{ai} + H_{bi}T + H_{ci}T^2 + H_{di}T^3 + H_{ei}T^4 + H_{fi}T^5, \quad (3.8)$$

where H_i is the enthalpy of component i and H_{ai} through H_{fi} are enthalpy coefficients for component i , with the enthalpy in Btu/lb and temperature in °R.

3.1.6 Solution method

In the species-based formulation applied in this chapter, (3.1), (3.3), (3.4) and (2.27) are discretized and solved fully implicitly. The unknowns to be computed are pressure, temperature, mole fractions of each fluid component, and solid concentrations.

We apply Newton’s method to solve the coupled equations (see Figure 2.2). After

the Jacobian matrix is formed at each Newton iteration, we reduce the number of equations and variables to a set that is solved simultaneously. This reduced set of variables are the primary variables. We note that we do not decouple localized reactions. Thus the number of primary variables is n_c . The remaining (secondary) variables are recovered from the primary variables after each Newton iteration.

The new time step is prescribed based on changes in the unknowns over the previous time step as follows:

$$\Delta t^{n+1} = \Delta t^n \min \left[\frac{(1 + \omega)\eta_v}{\delta_v + \omega\eta_v} \right], \quad (3.9)$$

where Δt^{n+1} is the next time step, Δt^n is the current time step, ω is a tuning factor between 0 and 1, δ_v is a parameter for each variable v , η_v is the desired change for each variable, and the minimum is over all grid blocks [10]. The key parameter affecting simulator performance is the parameter η_v . Our numerical experiments show that the desired variable change in in-situ upgrading simulations should be specified to be much smaller than in compositional simulations without reactions. This is because, when the concentration of a specific component is small, for example 10^{-3} lbmol/ft³, a desired change of 5×10^{-4} lbmol/ft³ corresponds to a 50% change, and this may hinder convergence. Suggested parameter values for the in-situ upgrading simulations are listed in Table 3.2.

3.2 Modeling the MDP-S project

In this section we describe the Mahogany Demonstration Project-South and then present our detailed modeling procedure and simulation results for this project.

Table 3.2: Suggested values for time step control parameters

Parameter	Value (no reactions)	Value (with reactions)
δ	0	0
ω	0.5	0.5
η for pressure	200 psi	10 psi
η for saturations	0.02	0.01
η for molar fractions	0.02	0.001

3.2.1 Mahogany Demonstration Project-South

Mahogany Demonstration Project-South (MDP-S) is a pilot in-situ conversion project conducted by Shell in the Green River formation from 2003 to 2005 [18]. MDP-S is a follow-up to the original Mahogany Demonstration Project. Sixteen vertical heaters were drilled in three rings, and two producers were placed in the center of the heating pattern. One additional perimeter producer hole was drilled outside the pattern [18]. Heating was conducted over a 113 ft interval. The top of this interval was at a depth of 280 ft.

3.2.2 Description of MDP-S model

In order to validate our in-situ upgrading modeling capability, we developed a 3D model of MDP-S based, to the extent possible, on the information provided in [18] and [62]. Because much of the necessary data is proprietary, some parameters are estimated based on available publications and some are determined through history matching.

The model area is shown in Figure 3.1. The model contains two regions, a central flow region and a surrounding heat loss region. The central region, designated by AA'

in Figure 3.1(a) and 3.1(b), is approximately 47 ft in diameter and 113 ft in depth. This is the heated interval. Because heat loss is a key concern in in-situ upgrading processes, a much larger heat loss region is also included in the model. This region allows us to capture both peripheral heat loss and heat loss to the overburden and underburden. The heat loss region is designated by CC' in Figure 3.1(a) and 3.1(b). The overall model (central flow and heat loss regions) is approximately 202 ft in diameter and 273 ft in depth.

The initial porosity and permeability of the oil shale formation are very low [33], though as the kerogen decomposes both porosity and permeability increase. Reasonable values for the initial porosity and horizontal permeability are 0.0001 and 1 md, which are rounded from the data reported in [64]. An appropriate value for initial vertical permeability would therefore be about 0.1 md, which accounts for a typical degree of anisotropy.

In the central flow region, we expect the porosity and permeability to be much higher than these initial values because of kerogen decomposition. As indicated above, we do not model porosity and permeability evolution, so ‘effective’ values must be assigned for these parameters in the central flow region. For a typical (rich) oil shale formation with 15 weight percent kerogen, we estimate that the porosity generated by kerogen decomposition is approximately 0.10. However, a significant fraction of the decomposition products are solids (e.g., prechar and char), and these can refill half or more of the pore space generated by kerogen decomposition. In this work we therefore use 0.05 as the effective porosity for the central flow region. We assign the permeability for this region to be 300 md, which we calculate using the Carman-Kozeny formula presented in [64] with a value of 0.05 for porosity. Because this

permeability value is of course just an estimate, we performed a sensitivity study to assess the impact of permeability on simulation results. We observed relatively small changes in oil and gas production for permeability over the range of 80 md - 600 md. Therefore, our general findings can be expected to hold under the reasonable assumption that the true effective permeability is indeed within this range.

Since very little kerogen decomposes in the heat loss region, we assign the initial porosity and permeability to the blocks in this region. Because there is very little fluid flow in the heat loss region, the major physical process there is heat conduction. Our simulation results clearly demonstrate that the heat loss region is sufficiently large to capture the key heat loss effects. More specifically, as will be shown below, the region boundaries remain at essentially the initial formation temperature over the course of the entire simulation, indicating that they are not affected by the downhole heaters.

We note finally that the authors of [18] refer to the presence of pre-existing fractures in the formation. However, in the absence of quantitative data (e.g., fracture length, density and aperture distributions, etc.), it is impossible to gauge the effects of these fractures on porosity and permeability, either before or after kerogen decomposition. Thus we have not attempted to account for these fractures in our model of MDP-S.

Within the central flow region, we place the 16 heaters and three producers as described in [18]. As shown in Figure 3.2(a), the heaters are placed in three rings. The outer two rings form hexagon patterns, with heater spacing of 14 ft and 19.5 ft, respectively. The spacing of the four heaters in the inner ring is taken to be 10 ft. This spacing was estimated from Figure 8 in [18]. The heater temperature (or specifics

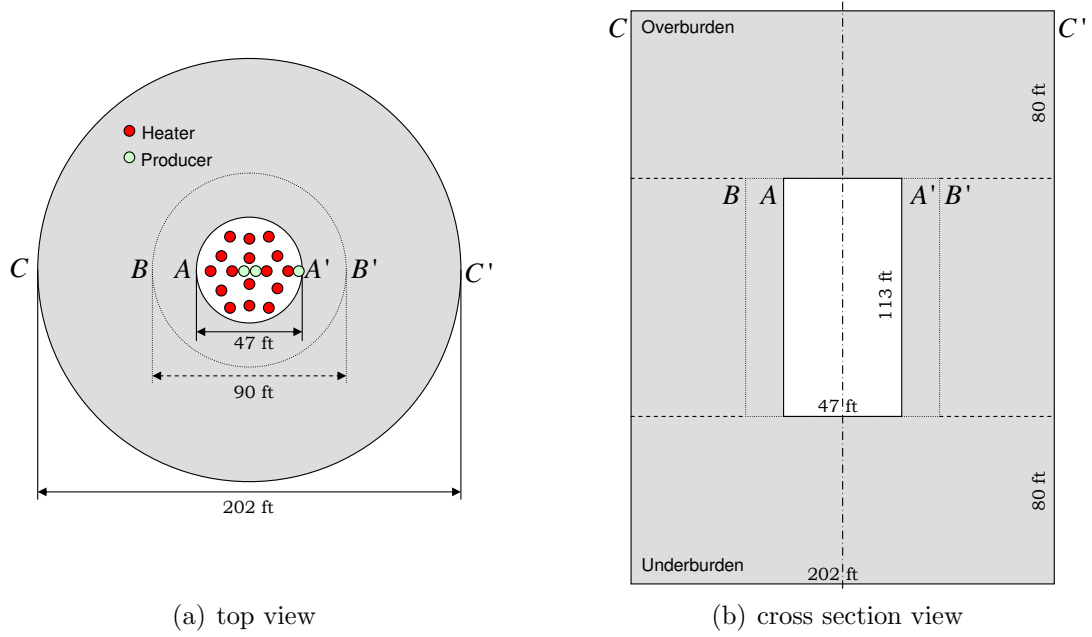


Figure 3.1: Model area for Mahogany Demonstration Project-South.

regarding power input) for MDP-S are not specified in [18]. In our simulation we apply constant temperature heating with $T_h = 700^\circ\text{F}$. This value is within the range for target formation temperatures for in-situ upgrading processes [5]. The central producers are placed 5 ft apart and the perimeter producer is located 4 ft south of the southern-most heater. All producers are specified to operate with a bottomhole pressure of 30 psi. We represent the system using a polar grid, shown in Figure 3.2(b). Because of symmetry, we model only half of the region and then multiply the total production data by two to obtain full-field results. A limited grid refinement study demonstrated that the general level of grid resolution used here is sufficient.

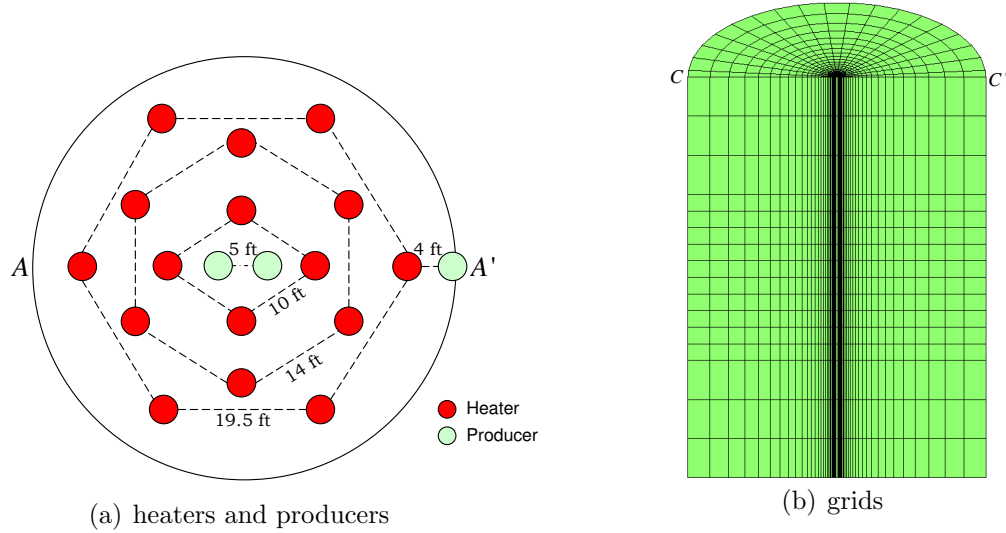


Figure 3.2: Heater positions and gridding of the simulation model for Mahogany Demonstration Project-South.

3.2.3 Model components, reactions and other parameters

Modeling of the in-situ upgrading process for MDP-S requires phase component data, chemical kinetics data, initial formation conditions, and thermal properties of the rock. We now describe our models for these data.

The reactions included in the model were determined based on the data provided by [64]. Because these reactions are defined in terms of generic components (e.g., heavy oil, light oil, hydrocarbon gas), whose properties are not defined, we must relate these ‘pseudo-components’ to actual components and then apply lumping procedures to determine properties. We proceed as follows.

The reactions included in the model and the associated kinetic data are listed in Table 3.3. We use pseudo-species IC_{37} to represent heavy oil, IC_{13} to represent light oil, and IC_2 to represent the hydrocarbon gas referred to in [64]. The reactions in Table 3.3 were modified slightly from those presented in [64]. Specifically, we

eliminated water and prechar from the reactions (water is not included in our model and prechar is assumed to stay in the solid phase, as discussed above). In addition, we combined the two parallel kerogen decomposition reactions in [64] to one reaction (Reaction 1 in Table 3.3). Our numerical results show that this combination reduces computation time and does not affect hydrocarbon production rates. The reactions in Table 3.3 are not in exact element balance because we do not include the prechar and char products, which are not considered in the transport equations. This imbalance is not a problem for our species-based formulation because this mass originates from the solid phase, which is treated as the hydrocarbon source.

Table 3.3: Kinetic reactions in MDP-S case (adapted from [64])

No.	Reactions and Parameters
1	$\text{KER(s)} \rightarrow 0.0096 \text{ IC}_{37} + 0.0178 \text{ IC}_{13} + 0.04475 \text{ IC}_2 + 0.00541 \text{ CO}_2$ $A = 3.74 \times 10^{12}, E_a = 161.600 \text{ kJ/mol}$
2	$\text{IC}_{37}(\text{g}) \rightarrow 1.853 \text{ IC}_{13} + 0.045 \text{ IC}_2$ $A = 2.65 \times 10^{20}, E_a = 206.034 \text{ kJ/mol}$
3	$\text{IC}_{37}(\text{o}) \rightarrow 0.2063 \text{ IC}_{13} + 2.365 \text{ IC}_2$ $A = 6.25 \times 10^{16}, E_a = 206.034 \text{ kJ/mol}$
4	$\text{IC}_{13}(\text{g}) \rightarrow 5.73 \text{ IC}_2$ $A = 3.82 \times 10^{20}, E_a = 219.328 \text{ kJ/mol}$
5	$\text{IC}_{13}(\text{o}) \rightarrow 0.573 \text{ IC}_2$ $A = 9.85 \times 10^{16}, E_a = 219.328 \text{ kJ/mol}$

The components used in our model are taken from the pyrolysis analysis of Green River oil shale in [7]. These experiments identified 31 components, consisting of 22 oil species and nine gas species. As a simplification, we consider only the 11 most abundant oil species and the four most abundant gas species. Because the available set of kinetics data (Table 3.3) is in terms of only three hydrocarbon species, we performed

a component lumping process to map the 13 hydrocarbon species to the three pseudo-components appearing in Table 3.3. The original components and the lumped pseudo-components used in the model are listed in Table 3.4 and Table 3.5. The gas species CH_4 and CH_x were lumped to one component and mapped to pseudo-species IC_2 , the oil species Oil-1 to Oil-6 were lumped and mapped to IC_{13} , and the oil species Oil-7 to Oil-11 were lumped and mapped to IC_{37} . The interaction coefficients for these lumped components, for use in the equation of state, are provided in Table 3.6. The enthalpy coefficients for the individual oil and gas species are determined from [48]. Enthalpy coefficients for the lumped components are listed in Table 3.7. The lumping process was accomplished using the software package WinProp [38]. The other parameters used in the MDP-S simulation are given in Table 3.8 (two of these parameters are established through history matching, as described below).

The pore space of oil shale formations can initially be saturated with brine or gases. Here we specify the pore space to be initially saturated with nitrogen and carbon dioxide. These gases are produced from the central producer at early time. As the kerogen decomposes, the pore space becomes saturated with hydrocarbons. As discussed above, we do not include porosity and permeability evolution in our model.

The parameters described above are treated as fixed. Two other parameters in the model, initial kerogen concentration and thermal conductivity, are treated as adjustable parameters because they are not reported. Data are available, however, which prescribe reasonable physical ranges for these quantities. Commercially feasible oil shale deposits contain between about 10 and 20 weight percent kerogen [15]. The

Table 3.4: Compositions and properties – Green River oil shale pyrolysis components (from [7])

Species Name	Molar Weight (g/mol)	Critical Pressure (psi)	Critical Temperature (R)	Accentric Factor
CO ₂	44.01	1070.40	547.53	0.239
N ₂	28.01	491.68	227.13	0.039
CH ₄	16.04	667.18	342.33	0.011
CH _x	44.10	616.42	666.33	0.153
Oil-1	86	493.14	979.53	0.227
Oil-2	114	426.42	1103.73	0.300
Oil-3	142	374.20	1218.93	0.307
Oil-4	177	333.59	1323.33	0.379
Oil-5	212	292.98	1413.33	0.426
Oil-6	261	253.82	1506.93	0.511
Oil-7	317	213.21	1595.13	0.594
Oil-8	380	174.05	1674.33	0.664
Oil-9	464	133.44	1751.73	0.762
Oil-10	562	92.82	1793.13	0.941
Oil-11	703	92.82	1830.93	1.31

Table 3.5: Green River oil shale pyrolysis components and lumped components

Species Name	Molar Weight (g/mol)	Critical Pressure (psi)	Critical Temperature (R)	Accentric Factor
CO ₂	44.01	1070.40	547.53	0.239
N ₂	28.01	491.68	227.13	0.039
IC ₂	30.07	668.48	519.74	0.008
IC ₁₃	169.52	348.82	1287.65	0.365
IC ₃₇	465.83	135.69	1732.11	0.818

Table 3.6: Interaction coefficients for components

	CO ₂	N ₂	IC ₂	IC ₁₃	IC ₃₇
CO ₂	0	0.00003	0.00411	0.04309	0.1006
N ₂	0.00003	0	0.0035	0.04561	0.10602
IC ₂	0.00411	0.0035	0	0.02462	0.07449
IC ₁₃	0.04309	0.04561	0.02462	0	0.0150
IC ₃₇	0.1006	0.10602	0.07449	0.0150	0

Table 3.7: Enthalpy coefficients for components

	CO ₂	N ₂	IC ₂	IC ₁₃	IC ₃₇
H_{ai} , Btu·lb ⁻¹	4.78E+00	-6.89E-01	-3.40E+00	0.00E+00	0.00E+00
H_{bi} , Btu·lb ⁻¹ ·(°R) ⁻¹	1.14E-01	2.54E-01	3.73E-01	-5.97E-02	-1.56E-02
H_{ci} , Btu·lb ⁻¹ ·(°R) ⁻²	1.01E-04	-1.45E-05	-1.08E-04	4.01E-04	3.90E-04
H_{di} , Btu·lb ⁻¹ ·(°R) ⁻³	-2.65E-08	1.25E-08	3.34E-07	-6.22E-08	-5.56E-08
H_{ei} , Btu·lb ⁻¹ ·(°R) ⁻⁴	3.47E-12	-1.71E-12	-1.39E-10	0.00E+00	0.00E+00
H_{fi} , Btu·lb ⁻¹ ·(°R) ⁻⁵	-1.31E-16	-8.24E-17	1.93E-14	0.00E+00	0.00E+00

Table 3.8: Summary of input parameters used in MDP-S model

Parameter	Value
grid (n_r, n_θ, n_z)	(33, 19, 16)
overburden thickness	80 ft
heated interval	113 ft
underburden thickness	80 ft
initial temperature	70 °F
initial pressure	101 psi
initial kerogen	1.3 lbmol/ft ³
rock compressibility	3×10^{-6} /psi
rock volumetric heat capacity	25 Btu/ft ³ /°F
porosity (heat loss region)	0.0001
permeability (heat loss region)	$k_r=k_\theta=10k_z=1$ md
porosity (central flow region)	0.05
permeability (central flow region)	$k_r=k_\theta=k_z=300$ md
thermal conductivity	7 Btu/ft/day/°F
heater temperature	700 °F
producer BHP	30 psi

density of oil shale is about 2 g/cm^3 , so the kerogen content should be about 0.2-0.4 g kerogen/ cm^3 oil shale. Given that we represent kerogen as $\text{CH}_{1.5}\text{N}_{0.026}\text{O}_{0.05}$, this range corresponds to 0.85-1.7 lbmol/ ft^3 . As indicated above, thermal conductivity was reported to vary from 3.5-8.7 Btu/ $\text{ft}/\text{day}/^\circ\text{F}$ for organic-rich oil shale formations [45].

We varied the initial kerogen concentration and thermal conductivity over these physical ranges in order to establish a reasonable level of agreement between our simulation results and the MDP-S pilot data. The parameter values thus determined are 1.3 lbmol/ ft^3 for the initial kerogen concentration and 7 Btu/ $\text{ft}/\text{day}/^\circ\text{F}$ for the rock thermal conductivity. Using these parameters, the model predicts total oil production of 1,834 bbl and total hydrocarbon production of 2,529 bbl of oil equivalent (boe) after 500 days of production (in computing boe, we take 5.478 mcf of gas to be equivalent to one barrel of oil). The reported field test results are 1,813 bbl of oil and 2,659 boe, respectively [62]. The simulation predictions for total production are within 5% of the field test results. The cumulative oil and total productions as a function of time are shown in Figure 3.3(b). It is evident that there is a reasonable agreement between the MDP-S results and our simulation over the entire production period.

Although these MDP-S model parameters are physically realistic, this ‘history match’ is of course nonunique, and it is likely that other sets of parameters would provide comparable agreement with the field data. We further expect that the level of agreement could be improved by treating more parameters as adjustable (e.g., effective porosity and permeability). Nonetheless, the fact that we are able to achieve acceptable agreement with the test results, using realistic parameter values, provides

a degree of validation for our implementation.

3.2.4 Simulation results

The oil and gas production results for the MDP-S case are shown in Figure 3.3(a) and Figure 3.3(b). Figure 3.3(a) illustrates some characteristics of the in-situ upgrading process. The initial high gas production rate is due to the decomposition of the kerogen in the heater blocks – this kerogen breaks down quickly after the simulation starts (the heaters are operated at a temperature of 700 °F). The reservoir temperature then gradually increases, and both gas and oil production ramp up approximately 50 days after heat injection is initiated. Peak hydrocarbon production is reached at about 220 days. Then, as the kerogen is consumed, oil and gas production rates decrease.

As discussed earlier, the porosity was set to 0.0001 in the heat loss regions. Because this very low value for porosity necessitates small time steps and thus leads to high computation times, we investigated the impact of deactivating the cells in the heat loss regions with respect to flow by setting permeability to zero (these cells are still active in terms of heat conduction). Simulation results for this case are very similar to those for the previous case; e.g., kerogen concentration maps are essentially identical and there is only a difference of 0.2% in total hydrocarbon production between the two cases. By deactivating these cells, however, we achieved a speedup factor of two relative to the previous case. Therefore, in all of the following simulations, we consistently set permeability to zero in the heat loss regions.

Figure 3.4 shows a cross-sectional view of the temperature in the MDP-S model after 500 days of heat injection. Most of the central flow region is above 600 °F except for the portion adjacent to the surrounding heat loss region. The simulation results

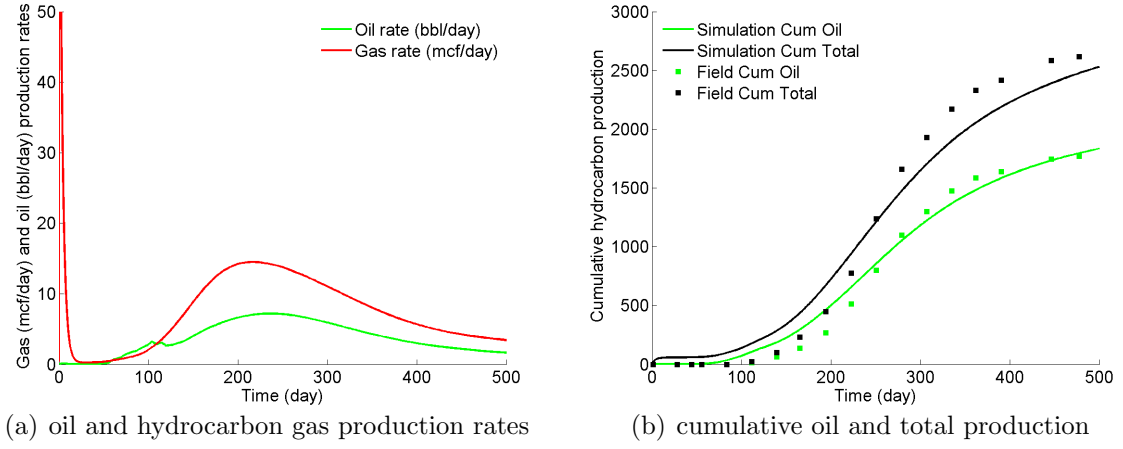


Figure 3.3: Hydrocarbon production results for the MDP-S project. Solid lines are simulation results from our model. Symbols are MDP-S field test results from [62].

indicate that the temperature change far from the heaters is not significant. In the figures that follow, we therefore show only the central flow region and a small portion of the heat loss region. This region is designated as BB' in Figure 3.1(a).

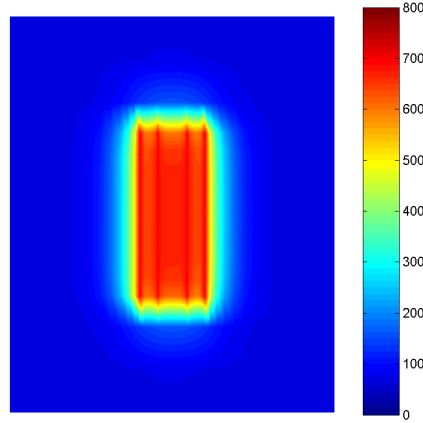


Figure 3.4: Cross-sectional view of temperature ($^{\circ}\text{F}$) at 500 days (region between CC' in Figure 3.1(b) shown).

Figures 3.5-3.7 depict the formation temperature, kerogen concentration and oil saturation at various times during the in-situ upgrading process. The heating of the

central flow region is evident from Figure 3.5. From Figure 3.6 we see that kerogen first decomposes near the heaters and eventually throughout the entire heated region. After 500 days, the kerogen is almost fully depleted. At 60 days, the oil saturation map (Figure 3.7) is more or less the inverse of the kerogen map, except that the oil is impacted by gravity. The producers are completed at the bottom of the heated interval, so it is from here that oil and gas are produced. Figure 3.7 also shows that the oil within the heating pattern is completely produced at 500 days. However, some oil just outside the heating pattern has not yet been produced. This is because the viscosity of this oil is higher due to the lower temperature in this region.

Overall oil and gas production rates are shown in Figures 3.3(a) and 3.3(b). It is, however, also of interest to consider the composition of the produced oil and gas. These compositions are presented in Figure 3.8. Here we see that the largest gas component is IC_2 and the largest oil component is IC_{13} . The production rate of the heavy oil species IC_{37} in both the gas and oil phases is close to zero due to the fact that this component decomposes very quickly once it is generated. The overall produced oil can be classified as high-quality light oil, with an average API gravity of 45. This value is of course strongly dependent on the components lumped into IC_{13} . It is of interest to note that the API gravity of the MDP-S oil is also reported to be 45 [62].

3.3 Sensitivity analysis

We now assess the sensitivity of the in-situ upgrading procedure to key engineering parameters, specifically heater temperature, heater pattern and heater spacing effects. For this assessment, we model infinite systems containing repeated patterns of heaters and producers. For such models, we need only simulate a single symmetry element

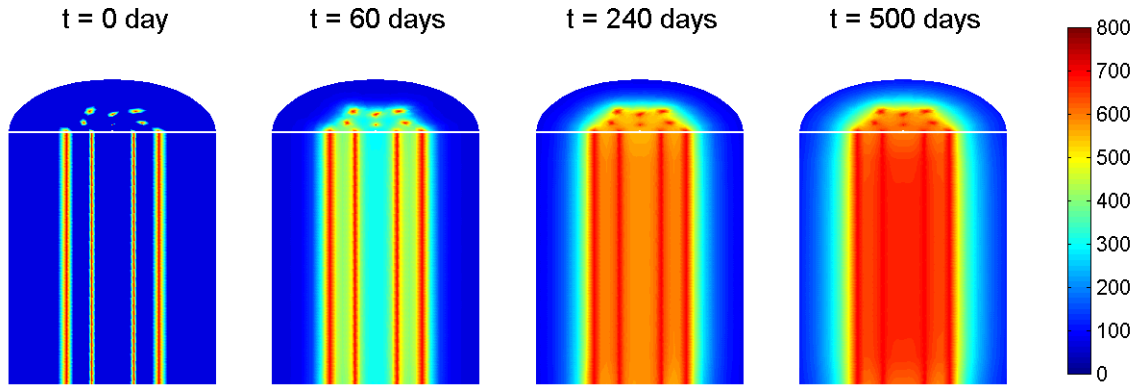


Figure 3.5: Temperature ($^{\circ}\text{F}$) for MDP-S simulation over region BB' (shown in Figure 3.1(b)).

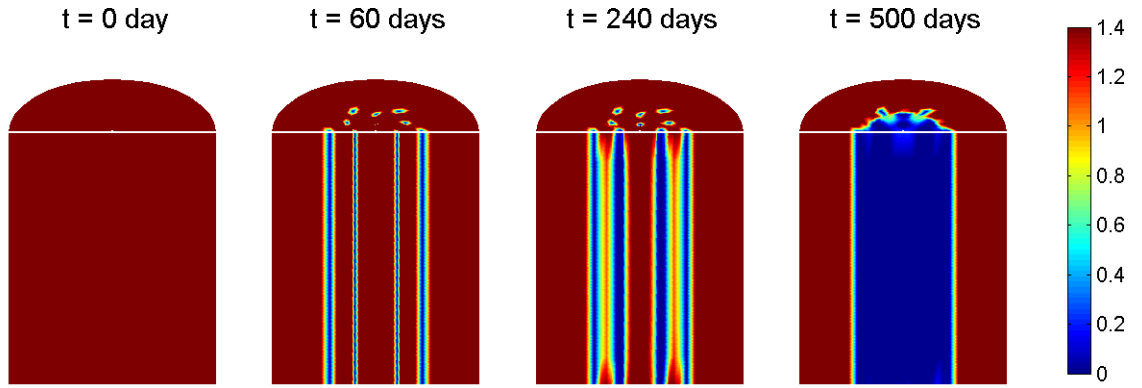


Figure 3.6: Remaining kerogen (lbmol/ft³) for MDP-S simulation over region BB' .

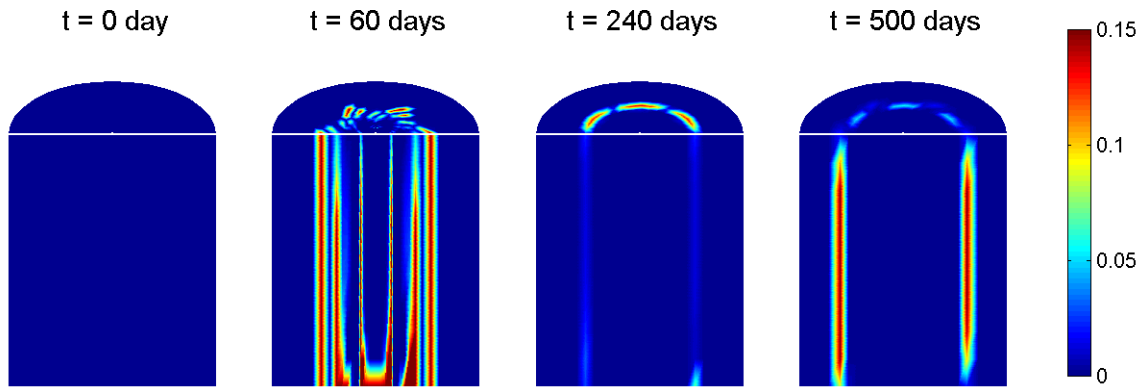


Figure 3.7: Oil saturation for MDP-S simulation over region BB' .

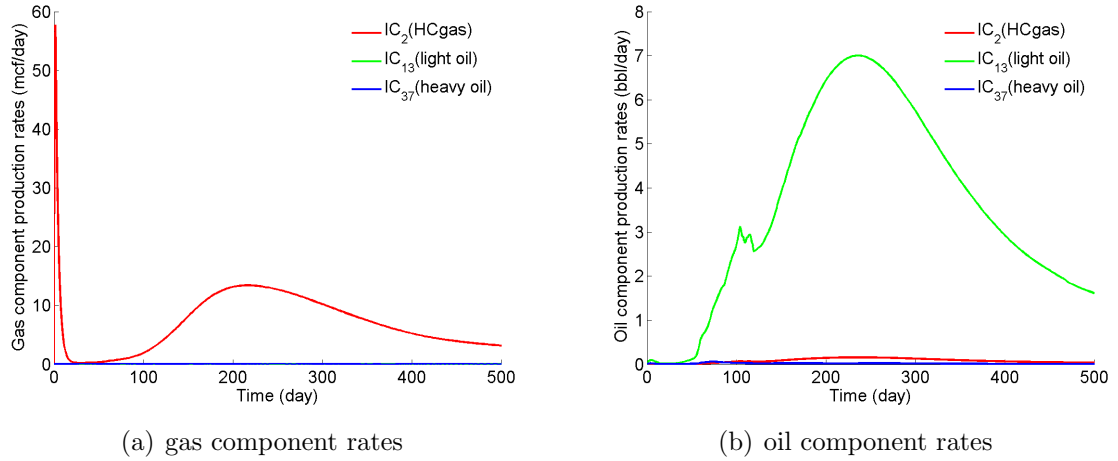


Figure 3.8: Hydrocarbon component production rates from MDP-S model.

(or a portion of a symmetry element).

The patterns considered are shown in Figures 3.9(a) - 3.9(c). The base case here is the hexagonal heater arrangement (Figure 3.9(a)) with the heaters operated at a constant temperature of 700°F. The heater spacing is 8 ft. The simulation area within one hexagon pattern in the base case is approximately 183 ft². The thickness of the overburden and underburden are both 80 ft (these are included to account for heat loss). We use Cartesian grids with cell dimensions $\Delta x = \Delta y = 0.5$ ft and $\Delta z = 11.3$ ft in the heated interval and $\Delta z = 26.7$ ft in the overburden and underburden. A limited grid refinement study showed that production results are insensitive to further refinement. Peripheral heat loss does not occur in any of the sensitivity cases because the patterns are considered to be repeated indefinitely. Except where otherwise specified, the other model parameters are the same as those used in the MDP-S simulation discussed above.

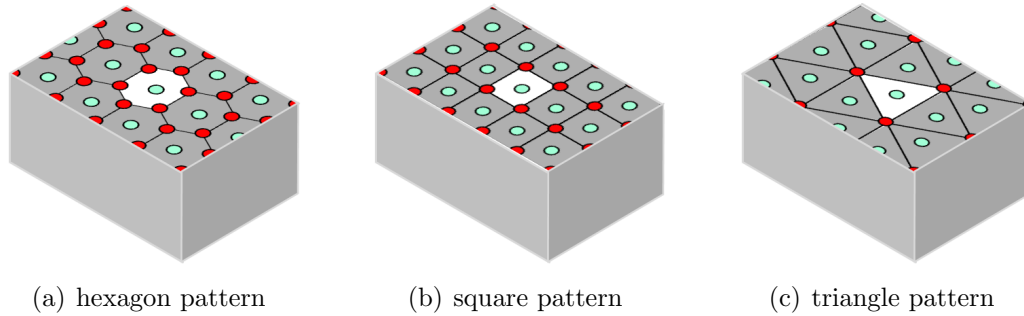


Figure 3.9: Top view of heaters and producers for sensitivity analysis.

3.3.1 Temperature effect

We first consider the effect of heater temperature on the in-situ upgrading process. For these results we consider only the hexagon pattern. Due to symmetry, we simulate half of the pattern and then reconstruct results for the full pattern (in all cases we report results for the full pattern). Temperature results for the base case ($T_h = 700^\circ\text{F}$) are shown in Figure 3.10. We also considered $T_h = 650^\circ\text{F}$ and $T_h = 600^\circ\text{F}$. Results for these cases appear in Figure 3.11 and Figure 3.12. As expected, formation temperatures are consistently lower for the $T_h = 600^\circ\text{F}$ case.

Results for gas and oil rates and cumulative production for the three cases are presented in Figure 3.13. We observe that the hydrocarbon production is very sensitive to temperature – with these decreases in T_h , the peak oil and gas rates decrease significantly. The peak production times are also delayed, and the peaks are not as sharp, as the heater temperature decreases. This is due to the strong dependency of the reaction rates on temperature. In addition, at lower T_h the cumulative hydrocarbon production is consistently below that for the base case over the entire simulation. This is again due to the slower kinetics. The ultimate production for all three cases is expected to be the same if the simulations were run for very long times.

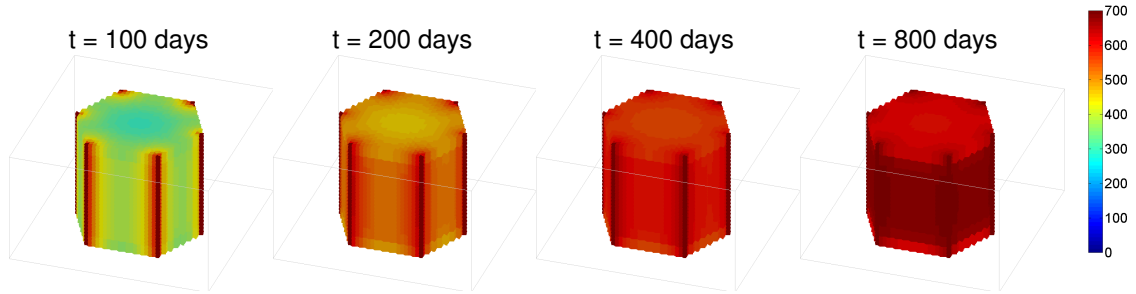


Figure 3.10: Temperature variation for repeated hexagon pattern (heater temperature is 700 °F, heater spacing is 8 ft). This model represents the base case.

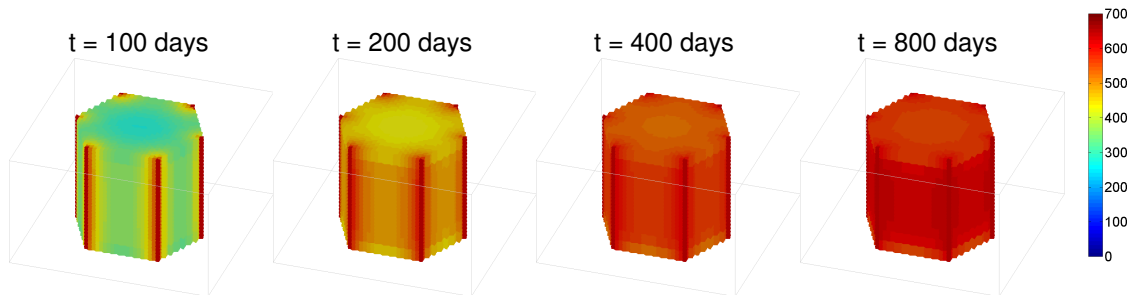


Figure 3.11: Temperature variation for repeated hexagon pattern (heater temperature is 650 °F, heater spacing is 8 ft).

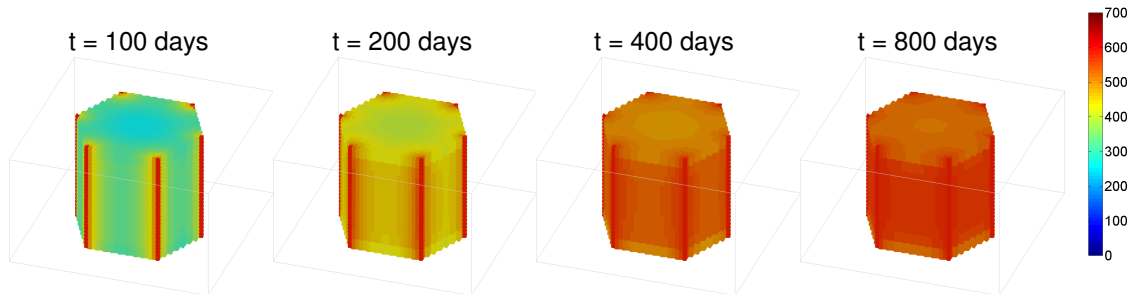


Figure 3.12: Temperature variation for repeated hexagon pattern (heater temperature is 600 °F, heater spacing is 8 ft).

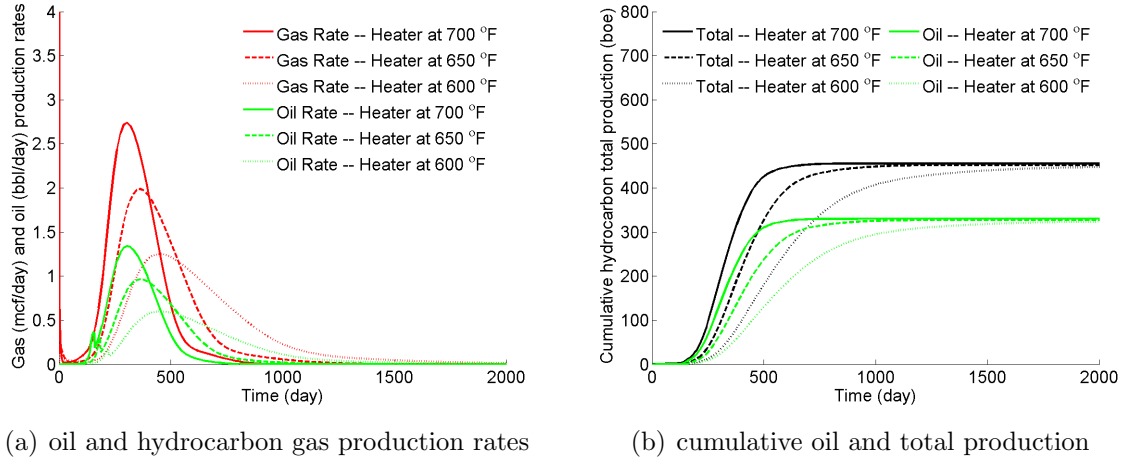


Figure 3.13: Effect of heater temperature on hydrocarbon production.

3.3.2 Heater pattern effect

We now evaluate the effect of heater pattern by considering two additional cases – a square heater pattern and a triangular heater pattern, as shown in Figures 3.9(b) and 3.9(c). All parameters are otherwise the same as in the base case (e.g., $T_h = 700^\circ\text{F}$). These patterns contain fewer heaters than the base case, but the total areas of all three patterns are essentially the same (within a few percent). The heater spacing is 13 ft in the square pattern and 20 ft in the triangular pattern.

Temperature results for the square and triangle patterns are shown in Figures 3.14 and 3.15. Production results for these patterns, along with those of the base case, are presented in Figure 3.16. As would be expected, with fewer heaters per volume of oil shale, more time is required for the formation temperature to approach T_h (compare Figures 3.10, 3.14 and 3.15), and the peak production times for both oil and gas are correspondingly delayed. It is also evident that, over the 2000 days of simulation, the cumulative hydrocarbon production for the square and triangle patterns is always

lower than that for the hexagon pattern.

These results are of interest as they illustrate the sorts of tradeoffs that must be considered in designing a field-scale in-situ upgrading process. Specifically, the triangle pattern entails fewer heaters so it will be less expensive to implement. The oil and gas produced from this pattern are delayed considerably, however, relative to that produced from the more expensive hexagon pattern – thus the value of the hydrocarbons produced from the triangle pattern must be discounted. The relative advantages and disadvantages of these and other patterns can best be assessed through a systematic study. It will also be useful to apply formal optimization strategies to this problem.

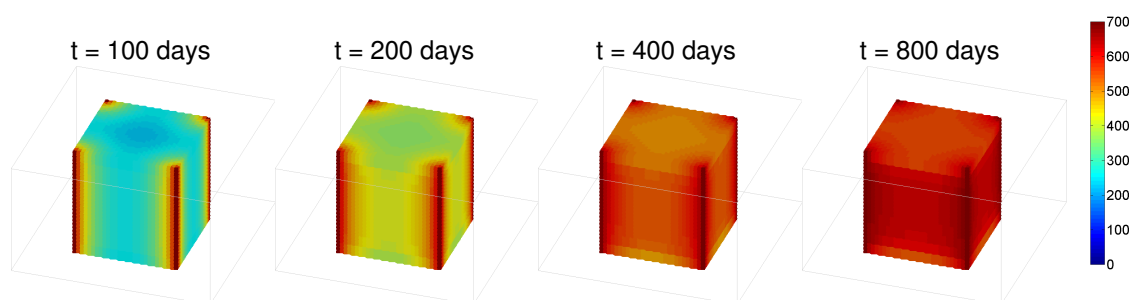


Figure 3.14: Temperature variation for repeated square pattern (heater temperature is 700 °F, heater spacing is 13 ft).

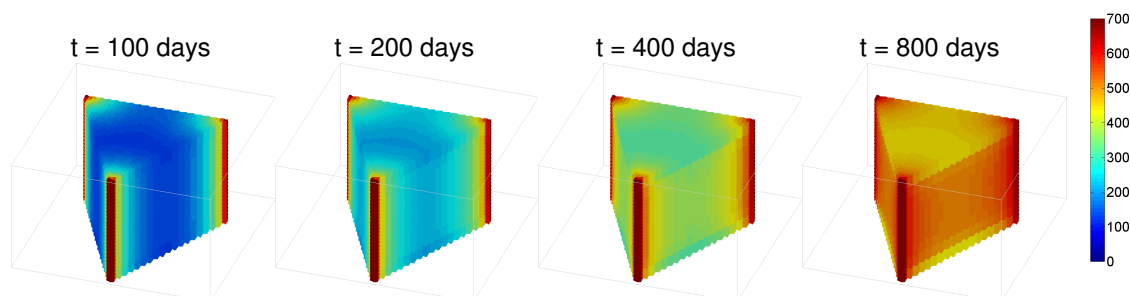


Figure 3.15: Temperature variation for repeated triangle pattern (heater temperature is 700 °F, heater spacing is 20 ft).

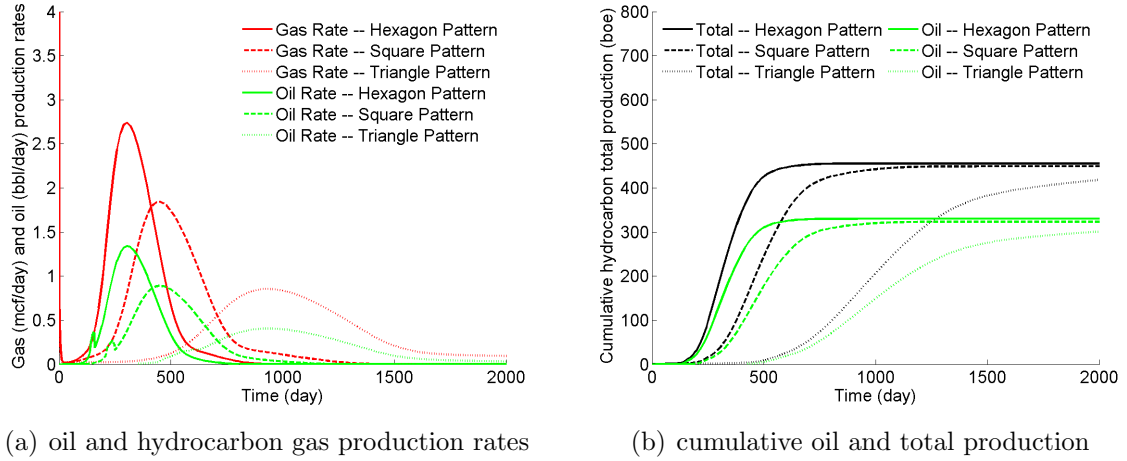


Figure 3.16: Effect of heating pattern on hydrocarbon production.

3.3.3 Heater spacing effect

The effect of the distance between adjacent heater wells is now studied by considering two additional cases for the hexagon pattern. The heater spacings in these cases are 10 ft and 12 ft. We note that the simulation areas increase when the heater spacing is increased. All other system parameters are the same as in the base case. The temperature variation for the cases with 10 ft and 12 ft spacings is shown in Figure 3.17 and Figure 3.18. Results for hydrocarbon production are shown in Figure 3.19. We observe that increases in heater spacing have a noticeable impact on reservoir temperature. Peak oil and gas production occurs later, and the peaks are less sharp, than in the base case (similar effects were observed above for the square and triangle patterns). With larger heater patterns, more total kerogen is available, though the decomposition requires more time. The ultimate cumulative hydrocarbon production in these cases is proportional to the pattern area. However, because of heat loss to the underburden and overburden, larger heater spacing requires more total energy

input (per energy produced) than smaller spacings. We quantify this effect in the next section.

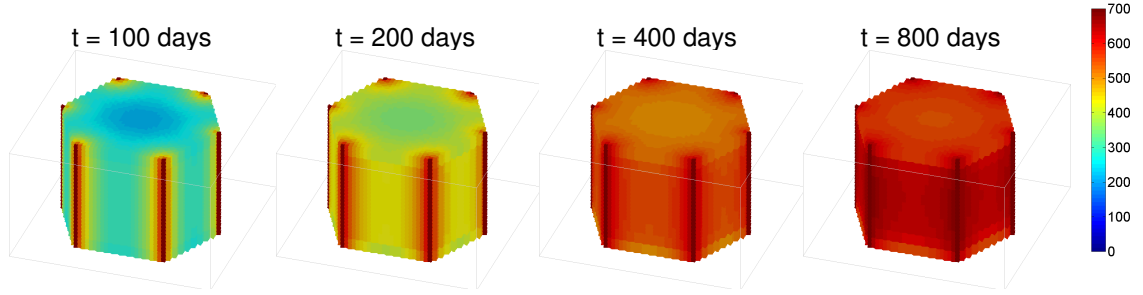


Figure 3.17: Temperature variation for repeated hexagon pattern (heater temperature is 700 °F, heater spacing is 10 ft).

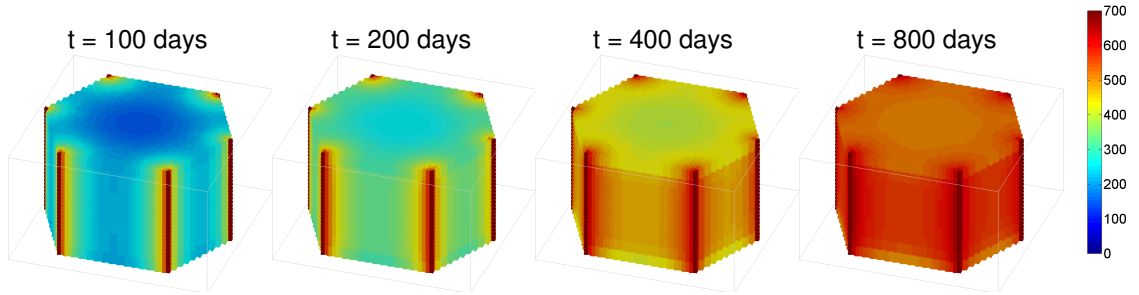


Figure 3.18: Temperature variation for repeated hexagon pattern (heater temperature is 700 °F, heater spacing is 12 ft).

3.3.4 Energy ratios for the various scenarios

A key efficiency measure for the in-situ upgrading process (or for any production operation that requires very substantial energy input) is the ratio of energy produced to energy expended. This ratio, which we refer to as E_{out}/E_{in} , should be significantly larger than unity for a cost-effective operation. Here we measure energy output as the

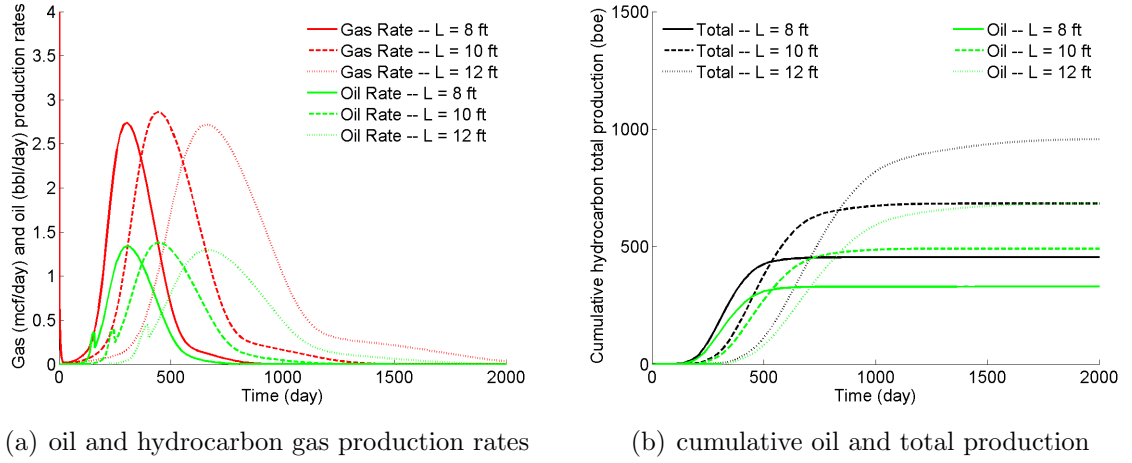


Figure 3.19: Effect of heater spacing on hydrocarbon production.

chemical energy content of the cumulative hydrocarbon production, with each barrel of oil equivalent yielding 5.6×10^6 Btu. The energy input considered here includes only thermal energy – we do not account for energy losses associated with, e.g., generating the electricity required to power the heaters. Since we use very large specific heat capacities for the heater blocks, the internal energy in the heater blocks at initial time is very large. Over the course of the simulation, thermal energy diffuses from heater blocks to the formation. The thermal energy introduced into the formation is computed from the total energy decrease in the heater blocks:

$$E_{in} = \sum_{h=1}^{n_h} (E_h^0 - E_h), \quad (3.10)$$

where h is heater block index, n_h is the number of heater blocks, E_h is the total internal energy in heater block h , and E_h^0 is the initial heater block energy.

In practice, it will not be economic to operate an in-situ upgrading process once

hydrocarbon production falls below some threshold. Here we assume that production proceeds until 90% of the hydrocarbons are produced. The total hydrocarbon production is computed based on a Fischer Assay of the kerogen. This means that different scenarios will operate for different periods of time. This procedure for computing E_{out}/E_{in} will generally benefit scenarios in which hydrocarbon production occurs quickly and shows sharp (rather than diffused) peaks.

Results for E_{out}/E_{in} are presented in Table 3.9. These energy ratios fall within a range of 6.2-6.9. The highest energy ratio is obtained for the base case and for the hexagon pattern with 8 ft heater spacing and $T_h = 650^\circ\text{F}$. The results in Table 3.9 indicate that the energy ratio decreases when the heater spacing increases. This can be explained in terms of heat loss to the overburden and underburden, as prolonged operating time results in increased energy loss.

It is of interest to compare these values with those computed in Brandt *et al.* [6], where a high-level (system) analysis of the in-situ upgrading process was performed. In his paper, Brandt considered a number of effects not included here, such as energy losses associated with electricity generation, so his values for E_{out}/E_{in} are much lower than those in Table 3.9. Considering only thermal energy inputs, as in the energy ratio results presented here, Brandt (personal communication) arrived at values for E_{out}/E_{in} of 6.1-7.4, which are in close agreement with the results presented in Table 3.9. This lends further credence to our in-situ upgrading modeling capability. We note finally that the existence of significant amounts of in-situ water will act to reduce E_{out}/E_{in} , as energy must be expended to heat and vaporize this water. This effect is not included in our model.

Table 3.9: Energy ratios for the sensitivity study cases (at 90% recovery efficiency)

Pattern	Heater Temperature	Heater Spacing	Thermal Energy Input (Btu)	Chemical Energy Output (Btu)	E_{out}/E_{in}
Hexagon	700 °F	8 ft	3.346E+08	2.296E+09	6.9
Hexagon	650 °F	8 ft	3.345E+08	2.296E+09	6.9
Hexagon	600 °F	8 ft	3.367E+08	2.296E+09	6.8
Square	700 °F	13 ft	3.396E+08	2.283E+09	6.7
Triangle	700 °F	20 ft	3.646E+08	2.261E+09	6.2
Hexagon	700 °F	10 ft	5.175E+08	3.480E+09	6.7
Hexagon	700 °F	12 ft	7.560E+08	4.914E+09	6.5

3.4 Concluding remarks

In this chapter, we applied the species-based chemical reaction formulation to model the in-situ upgrading of oil shale. In our model, chemical kinetics is fully coupled with a thermal-compositional formulation. We applied this modeling capability to simulate a system based on Shell's in-situ upgrading pilot test, the Mahogany Demonstration Project-South. These simulations used Green River oil shale data, 16 heaters and three producers. The downhole heaters were simulated as constant temperature heat sources. After modest tuning of some uncertain system parameters, the results from our model demonstrated reasonable agreement with data reported for the field test. This provides a degree of validation for the in-situ upgrading simulation capability.

A sensitivity analysis showed that the oil and gas production are highly dependent on the heater temperature. Over the range 600 °F to 700 °F, higher heater temperature was shown to provide faster overall hydrocarbon production. Heater pattern can also affect oil and gas production rates and cumulative production. The hydrocarbon yield is additionally impacted by the distance between adjacent wells. The

ratio of energy output to energy input was found to be in the range of 6.2-6.9 for all sensitivity cases considered. This ratio is impacted by heat loss to the overburden and underburden. In total, we believe that the simulation procedure developed here may, after further validation and extension, find use in the design and optimization of in-situ upgrading processes.

Chapter 4

Modeling Carbon Storage in Deep Saline Aquifers

The IPCC Special Report on Carbon Dioxide Capture and Storage [23] states that carbon dioxide constitutes the largest contribution to atmospheric greenhouse gases from human activities. Subsequent studies provide further evidence that carbon dioxide is a dominant cause of global climate change, particularly temperature increases [24]. Large-scale carbon capture and storage (CCS) in deep saline aquifers is being considered as an option for reducing anthropogenic CO₂ emissions to the atmosphere [3, 24]. Engineering models will be essential to all phases of the sequestration operation. In this chapter, we present a compositional simulator that models all of the known trapping mechanisms associated with CO₂ sequestration in deep saline aquifers, namely, structural, residual, solubility, and mineral trapping. The modeling of mineralization is achieved using the element-based nonlinear chemical reaction formulation described in Chapter 2.

4.1 Modeling techniques

Numerical simulation of the CO_2 sequestration process in deep saline aquifers involves modeling the complex interactions between the injected CO_2 , the resident fluid, and the rock. The transport involves gaseous species (e.g., $\text{CO}_2(\text{g})$, $\text{H}_2\text{O}(\text{g})$), electrically neutral species in the aqueous phase (e.g., $\text{CO}_2(\text{aq})$, $\text{SiO}_2(\text{aq})$), and electrically charged ions (e.g., H^+ , HCO_3^-). Geochemical reactions occur among these species. The actual physical and chemical processes that occur during CO_2 injection and migration are quite complex, and some effects are not incorporated in our model. Specifically, we do not include an energy balance to account for dynamic thermal effects, though we account for the presence of a geothermal gradient. Moreover, geomechanical effects are not included, and we assume that changes in the porosity due to mineral reactions are small [20]. We now describe our model in detail.

4.1.1 EOS based compositional simulation

Before CO_2 injection, the pore space in the aquifer is assumed to be fully saturated with brine, which consists of H_2O and a number of ions. The salinity of the brine is due to high concentrations of dissolved salts. Because the injected CO_2 and the resident brine are not completely miscible at typical reservoir conditions, two separate phases are formed, a gaseous phase (which is typically a supercritical fluid) consisting of CO_2 and vaporized H_2O and an aqueous phase consisting of H_2O , dissolved CO_2 , ions, and mineral compounds dissolved from rocks. We assume the ions do not partition into the gaseous phase.

In this work, we extended GPRS to simultaneously model systems with four phases, namely, gas, oil, water, and solid. Because the water phase in the current

version of GPRS is treated as an immiscible single-component phase in GPRS, for convenience we label the aqueous phase as the ‘oil’ phase in the simulator in order to model the transport of various ions.

Local phase equilibrium is assumed for each grid block. The species that can partition into both the gas and aqueous phases are CO_2 and H_2O . The phase equilibrium described by (2.27) can be written as:

$$f_i^g = f_i^{aq}, \quad (i = \text{CO}_2, \text{H}_2\text{O}), \quad (4.1)$$

where f denotes fugacity. We use the Peng-Robinson equation of state (EOS) [49] to model the phase equilibrium and to calculate the densities for both phases. The viscosities of the gaseous and liquid phases are modeled using a standard mixing rule for EOS calculations [28]. The parameters for EOS calculations involving CO_2 and H_2O are summarized in Table 4.1. These parameters are given in both SI and field units.

Table 4.1: Properties of CO_2 and H_2O for equation of state (EOS) calculations

	CO_2		H_2O	
	SI	field units	SI	field units
Crit. Temp.	304.13 K	547.43 R	647.09 K	1164.77 R
Crit. Pres.	7.38 MPa	1071.33 psi	22.06 MPa	3200 psi
Crit. Vol.	0.094 m ³ /kmol	1.506 ft ³ /lbmol	0.056 m ³ /kmol	0.898 ft ³ /lbmol
Acc. Factor	0.22394	0.22394	0.344	0.344
Molar weight	44.01 kg/kmol	44.01 lb/lbmol	18.02 kg/kmol	18.02 lb/lbmol

In addition to the parameters listed in Table 4.1, the EOS calculations also require the so-called volume shift parameter V_s for CO_2 and H_2O , and the binary interaction coefficient Ψ for the CO_2 - H_2O pair. We take $V_{s,\text{CO}_2} = 0.024668$ and treat $V_{s,\text{H}_2\text{O}}$ and

Ψ as adjustable parameters to fit the field (or experimental) data of the aqueous phase density and CO_2 solubility for specific injection sites. If field data are not available, $V_{s,\text{H}_2\text{O}}$ and Ψ can be estimated from the average reservoir temperature and salinity using the following expressions [29]:

$$V_{s,\text{H}_2\text{O}} = 0.179 + 2.22 \times 10^{-4}(T - 113) + 4.9867 \times 10^{-7}S_{\text{NaCl}}, \quad (4.2)$$

$$\Psi_{\text{CO}_2-\text{H}_2\text{O}} = -0.093625 + 4.861 \times 10^{-4}(T - 113) + 2.29 \times 10^{-7}S_{\text{NaCl}}, \quad (4.3)$$

where T is temperature in $^\circ\text{F}$ and S_{NaCl} is salinity in ppm of NaCl.

4.1.2 Hysteresis models

Residual trapping of CO_2 takes place when the brine (assumed to be the wetting phase in the presence of a supercritical CO_2 phase) imbibes into regions previously invaded by CO_2 . In order to properly represent the dynamics of residual trapping, a hysteresis model for the relative permeability is required. Various hysteresis models have been implemented and verified in GPRS [16]. Specifically, these models are the Land [31], Carlson [11] and Jerauld models [25]. We now discuss these hysteresis models.

Figure 4.1 illustrates a set of relative permeability curves for a gas-brine system. We assume that the maximum relative permeabilities of both the gas and aqueous phases are unity. The independent variable in the figure is the normalized gas phase saturation S_g^* , where

$$S_g^* = \frac{S_g}{1 - S_{wr}}. \quad (4.4)$$

Here S_g is gas saturation and S_{wr} is the irreducible aqueous phase saturation. In Figure 4.1, AB is the primary drainage curve for the gas phase. The curve BC is one of the scanning imbibition curves. If the CO_2 is injected near the bottom of the aquifer, the gas saturation in regions close to or above the injection location typically follows a process that can be described by the path A - B - E in Figure 4.1. At point E , the gas saturation $S_{g,E}^*$ consists of a residually trapped portion of gas due to capillary forces and free gas (the remaining mobile gas that is free to flow). The mobile gas saturation is determined by the effective relative permeability at E projected to the primary drainage curve (i.e., $S_{g,F}^*$). Therefore, the residually trapped CO_2 is $S_{g,E}^* - S_{g,F}^*$. We note that during the post-injection period, the amount of residually trapped CO_2 varies as a function of space and time.

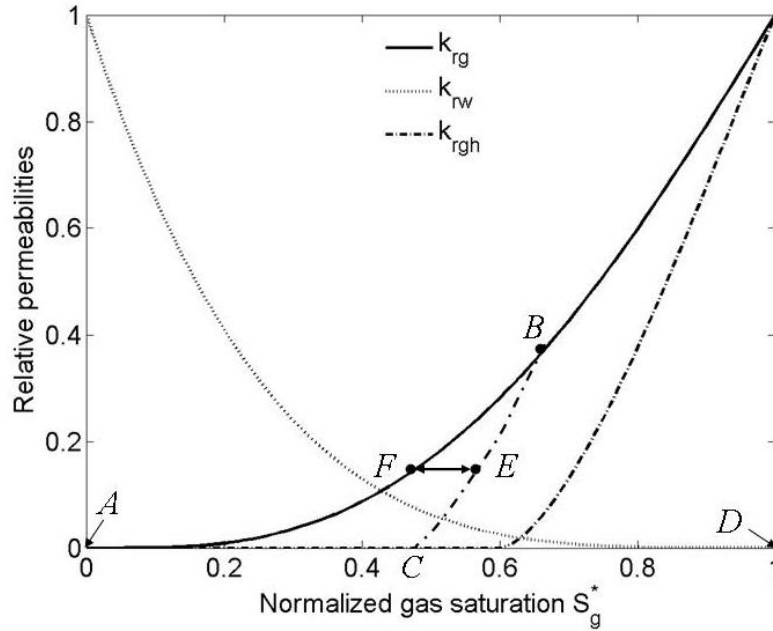


Figure 4.1: Illustration of gas-brine relative permeabilities and residual trapping.

4.1.3 Geochemical modeling

Geochemical simulation of CO₂ storage in saline aquifers entails modeling the transport of fluid species, the evolution of minerals, and chemical reactions between CO₂, H₂O, ions and minerals in the rock. The transport equations in GPRS are extended to handle the various fluid phases. The conservation equation for the solid is also a new development, as described in Chapter 2 (e.g., see Equation (2.5)).

The activity coefficients of electrically charged ions are calculated by the B-dot model (given earlier in (2.50)):

$$\log \gamma_{iw} = -\frac{Az_i^2\sqrt{I}}{1 + \hat{a}_i B\sqrt{I}} + \dot{B}I, \quad (4.5)$$

where the temperature-dependent constants A , B , and \dot{B} are given in Table 4.2. We interpolate these values for the temperature in each control volume (grid block) in our model. The ionic strength I is calculated by $I = 0.5 \sum_i m_i z_i^2$, where that m_i and z_i are the molality and electrical charge of each ion, respectively. The ionic size \hat{a}_i is taken from the EQ3/6 thermodynamic database [67].

Table 4.2: B-dot model parameters from the EQ3/6 database [67]

$T(^{\circ}\text{C})$	25	60	100	150	200
A	0.4939	0.5465	0.5995	0.6855	0.7994
B	0.3253	0.3346	0.3421	0.3525	0.3639
\dot{B}	0.041	0.0438	0.046	0.047	0.047

In this work, we take the activities of H₂O(aq) and of all minerals to be unity. Moreover, the activity coefficients of electrically neutral species (e.g., CO₂(aq), SiO₂(aq)) in the aqueous phase are also taken as unity. We note that, as indicated in Chapter 1,

the Pitzer activity model [51] may be required for systems with high salinity.

The geochemical reactions relevant to CO_2 mineralization include both equilibrium and kinetic reactions. The equilibrium reactions are characterized in terms of fluid and solid species activities. The reaction laws describing mineral precipitation, or dissolution, are taken from Nghiem *et al.* [42]. We apply the element-based formulation described in Chapter 2 to model the CO_2 mineralization processes. Newton's method is used to solve the resulting nonlinear system. Because the use of the GMRES solver preconditioned with CPR is the best solution strategy available in GPRS, we apply this approach for all simulations presented in this chapter.

4.2 Geochemical model verification

A verification case was carried out to compare the results from GPRS with GEM-GHG [36], a commercial simulator. This comparison case is designed to verify the various modules implemented in GPRS, including the B-dot activity model, chemical equilibrium calculations, mineral kinetic laws, and the numerical solution algorithm. We note that GEM-GHG uses a formulation equivalent to our species-based formulation, while we apply the element-based formulation here.

We consider a one-dimensional horizontal reservoir extending 306 m in the x direction and 3 m in both the y and z directions. The reservoir is discretized uniformly into 102 blocks. Initially, the reservoir is saturated with brine. We inject a pure CO_2 stream from the left-most block at constant bottomhole pressure (BHP). A producer under BHP control is located at the right-most block to maintain injectivity. The relevant parameters for this problem are given in Table 4.3.

This case involves eight minerals and 12 chemical reactions. The parameters

Table 4.3: Summary of input parameters for the verification case

Parameter	Value
grid (n_x, n_y, n_z)	(102, 1, 1)
grid block size	3 m \times 3 m \times 3 m
reservoir temperature	50 °C
initial pressure	3.46 MPa (502 psi)
porosity	0.10
permeability	$k_x=k_y=k_z=9.869 \times 10^{-14}$ m ² (100 md)
injector location	(1,1,1)
injector BHP	4.14 MPa (600 psi)
producer location	(102,1,1)
producer BHP	0.69 MPa (100 psi)

associated with the ions are listed in Table 4.4. The initial molalities of the ions are obtained by simulating a batch system (one grid block) for 5,000 years to ensure that chemical equilibrium is honored at initial conditions. The chemical reactions and mineral kinetic data were specified earlier in Tables 2.3 and 2.4.

Table 4.4: Input parameters for each ion for the verification case

Ion symbol	charge	size (Å)	initial molality (mol/kg)
H ⁺	1	9	5.71E-07
Al ⁺⁺⁺	3	9	3.13E-12
Fe ⁺⁺	2	6	2.73E-04
SiO ₂ (aq)	0	3	4.73E-04
K ⁺	1	3	9.89E-03
Ca ⁺⁺	2	6	2.52E-02
Mg ⁺⁺	2	8	2.62E-03
HCO ₃ ⁻	-1	4.5	2.14E-03
CO ₃ ⁻⁻	-2	4.5	4.23E-07
OH ⁻	-1	3.5	4.49E-08
Al(OH) ₂ ⁺	1	5	1.28E-09

Figures 4.2 and 4.3 present the ion molalities and mineral net changes after 50

days of injection. The symbols represent the results from GPRS and the lines represent the results from GEM-GHG. It is evident that the results from these two simulators are in very close agreement. We note that at 50 days, the injected CO_2 has flooded approximately 65% of the reservoir. The chemical system ahead of the CO_2 front is essentially not affected. This case provides a degree of verification of CO_2 mineralization modeling capabilities implemented in GPRS.

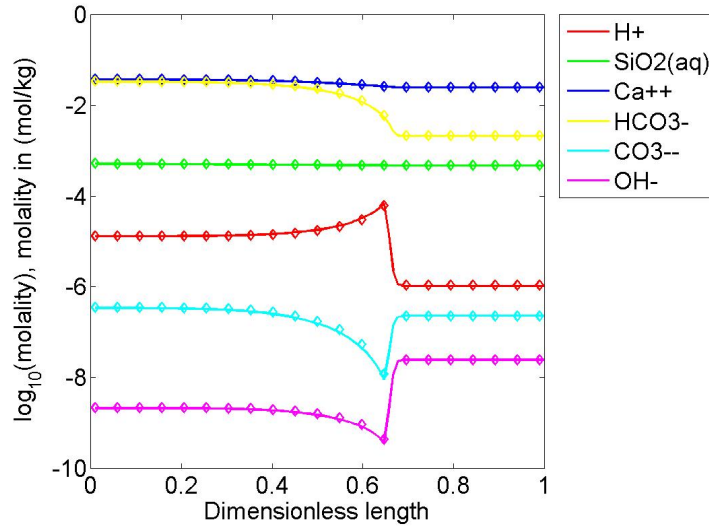


Figure 4.2: Comparison of ion molalities (mol/kg) from GPRS and GEM-GHG for 1-D case at 50 days. Symbols represent GPRS results, lines represent GEM-GHG results.

4.3 Simulation results of a benchmark case

We now present detailed results for a benchmark study of CO_2 injection into a large saline aquifer. For this study, we constructed two models: a fine-grid model with 300,000 grid blocks and a coarse-grid model with 1,500 blocks. We simulate the

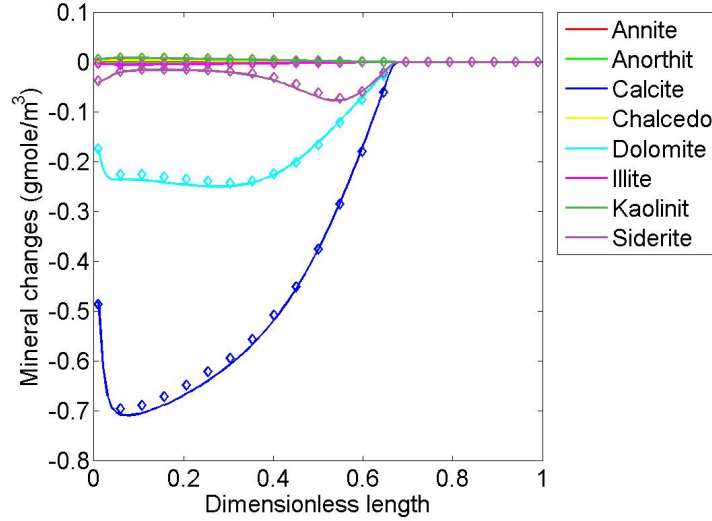


Figure 4.3: Comparison of mineral changes (mol/m^3) from GPRS and GEM-GHG for 1-D case at 50 days. Symbols represent GPRS results, lines represent GEM-GHG results.

CO_2 migration, dissolution, and residual trapping on the fine-grid model. On the coarse-grid model, we also consider geochemical reactions.

4.3.1 Model description

The basic benchmark study was proposed by Dahle *et al.* [14]. The original benchmark model is a homogeneous aquifer with 1% dip that extends for 200 km in the dip direction and 100 km in the direction perpendicular to the dip. The thickness of the aquifer is 50 m. The aquifer is confined by impermeable barriers from above and below. Constant-pressure conditions are applied on the horizontal boundaries. Our initial numerical tests show that it is not necessary to use the entire reservoir model. This is because the injected CO_2 is confined in the central area far from the boundaries for the time frame of interest (which is 20,000 years). Therefore, we model a

fraction of the aquifer, which is 15 km in the dip direction and 10 km in the direction perpendicular to the dip. The horizontal boundary conditions in the new model are also taken to be constant pressure conditions. The other model parameters, unless otherwise specified, are the same as those defined in [14].

Because of symmetry, we simulate only half of the domain; i.e., our model is 5 km in the y direction (shown in Figure 4.4). A horizontal well is perforated at the bottom of the aquifer, 5 km updip from the lowest point of the aquifer. The orientation of the well is perpendicular to the dip. The total length of the well completion zone is 1 km. Due to symmetry, we model only half of this total length. The well injects pure CO₂ at a rate of 1 Mt/yr for 20 years, after which the well is shut-in.

The relative permeabilities of the gas and aqueous phases are given by:

$$k_{rg} = 0.4[1 - (S_w^*)^2](1 - S_w^*)^2, \quad k_{rw} = (S_w^*)^4, \quad (4.6)$$

where S_w^* is the normalized aqueous phase saturation given by:

$$S_w^* = \frac{S_w - S_{wr}}{1 - S_{wr}}. \quad (4.7)$$

Here, the irreducible aqueous phase saturation S_{wr} is taken to be 0.20. Hysteresis is modeled using Land's relation, in which the irreducible gas saturation in the bounding (primary) imbibition curve is taken to be 0.20. The other parameters are summarized in Table 4.5.

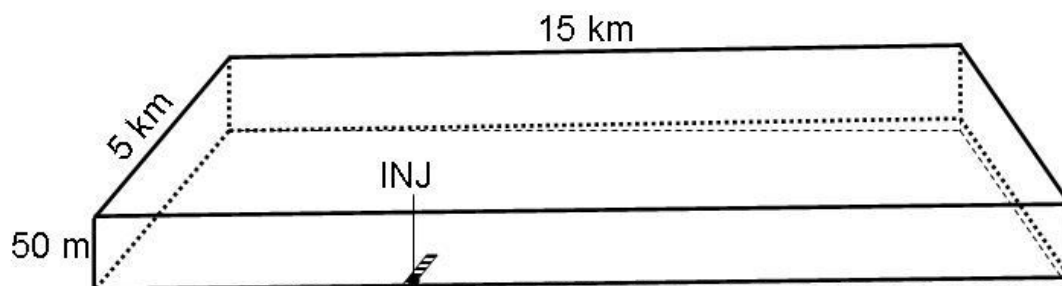


Figure 4.4: Schematic of model adapted from [14].

Table 4.5: Summary of input parameters for benchmark model

Parameter	Value
initial reference depth	2500 m
initial reference pressure	24.6 MPa (3568 psi)
initial reference temperature	72.5 °C (162.5 °F)
porosity	0.15
permeability	$k_x=k_y=k_z=10^{-13}$ m ² (101 md)
geothermal gradient	25 °C/km
rock thermal conductivity	3 W/m/K

4.3.2 Fine-grid results without geochemistry

We discretize the aquifer model shown in Figure 4.4 using 300,000 Cartesian grid blocks, specifically, 150 cells in the x direction, 50 cells in the y direction, and 40 cells in the z direction. The size of each grid block is $100 \text{ m} \times 100 \text{ m} \times 1.25 \text{ m}$. Figure 4.5 shows the evolution of gas phase saturation with time. We see that the gas (i.e., supercritical CO_2) migrates upwards, then slowly moves outwards in the updip direction due to buoyancy effects. During this migration, some amount of the gas phase is residually trapped by capillary forces. Figure 4.6 shows the residually trapped gas at four different times. In this case, residual trapping occurs mostly as the CO_2 plume moves from the bottom to the top of the aquifer. The difference between the saturation values in Figure 4.5 and those in Figure 4.6 represent the free gas saturation. At 20,000 years, there is essentially no free gas, because most of the CO_2 has either dissolved or is residually trapped.

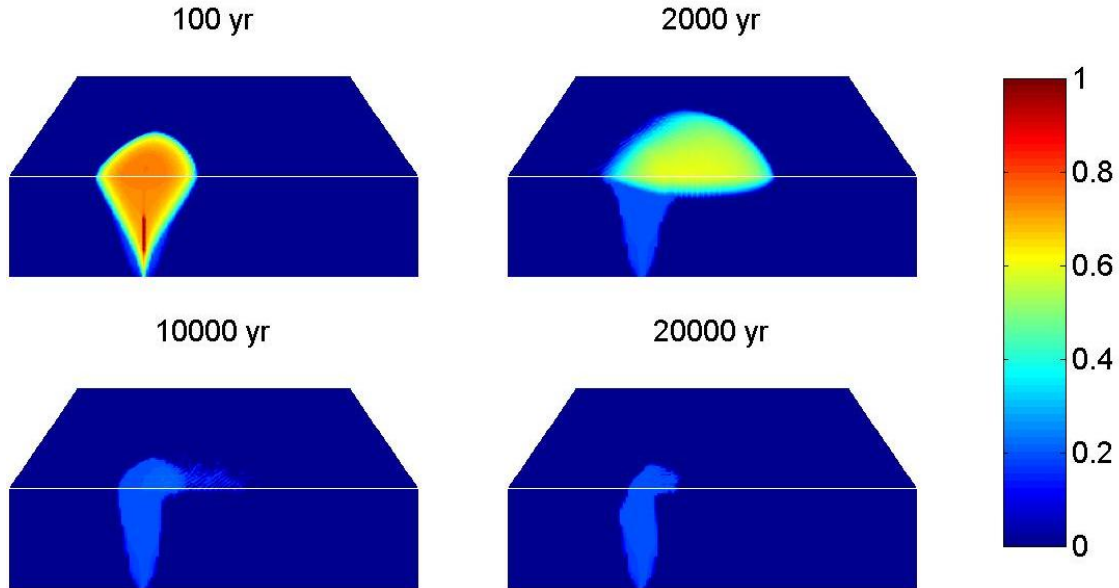


Figure 4.5: Gas phase saturation variation over time for the benchmark model.

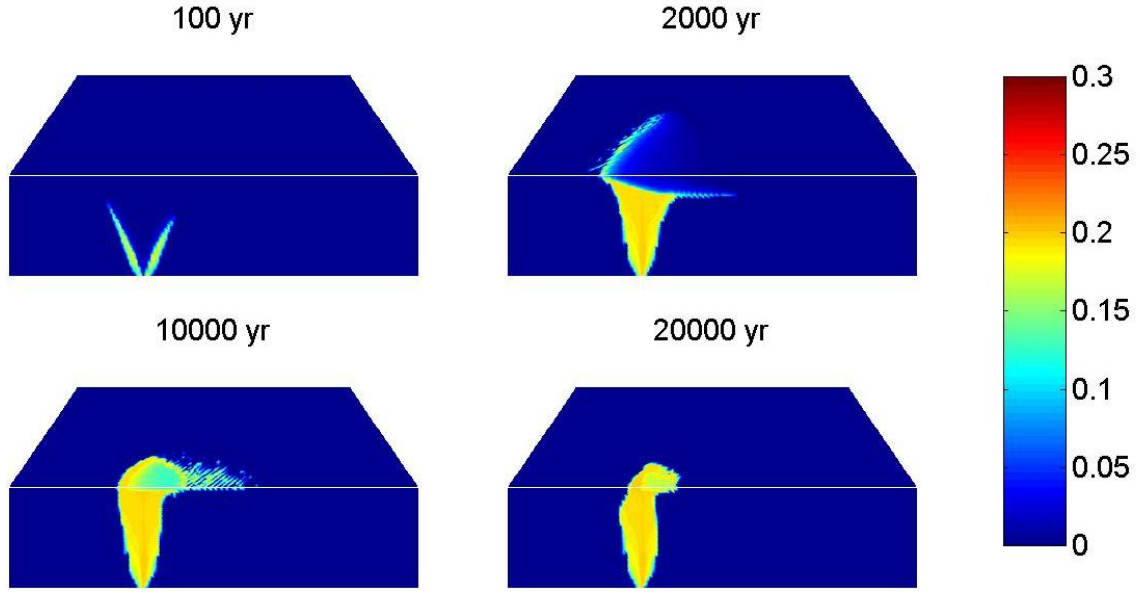


Figure 4.6: Residually trapped gas over time.

Figure 4.7 shows the dissolved CO_2 molar fraction in the aqueous phase. Because the supercritical CO_2 phase and the aqueous phase are immiscible, the dissolved CO_2 mole fractions varies from zero to approximately 0.05. In the first 100 years, CO_2 dissolves into the aqueous phase along the gas plume, and the aqueous phase becomes saturated with CO_2 in regions contacted by the gas. At later time, CO_2 dissolution occurs mostly at the interface of the gas plume, particularly into the underlying aqueous phase. Because the brine with dissolved CO_2 is more dense than that without CO_2 , the aqueous phase with dissolved CO_2 gradually settles under gravity [53]. At 20,000 years, all of the CO_2 in the gas plume is fully dissolved in the brine.

Figure 4.8 shows the evolution of the aqueous phase density during this process. It is evident that the density of the aqueous phase is closely related to the amount of dissolved CO_2 . Figure 4.8 also indicates that at later time, the water with dissolved

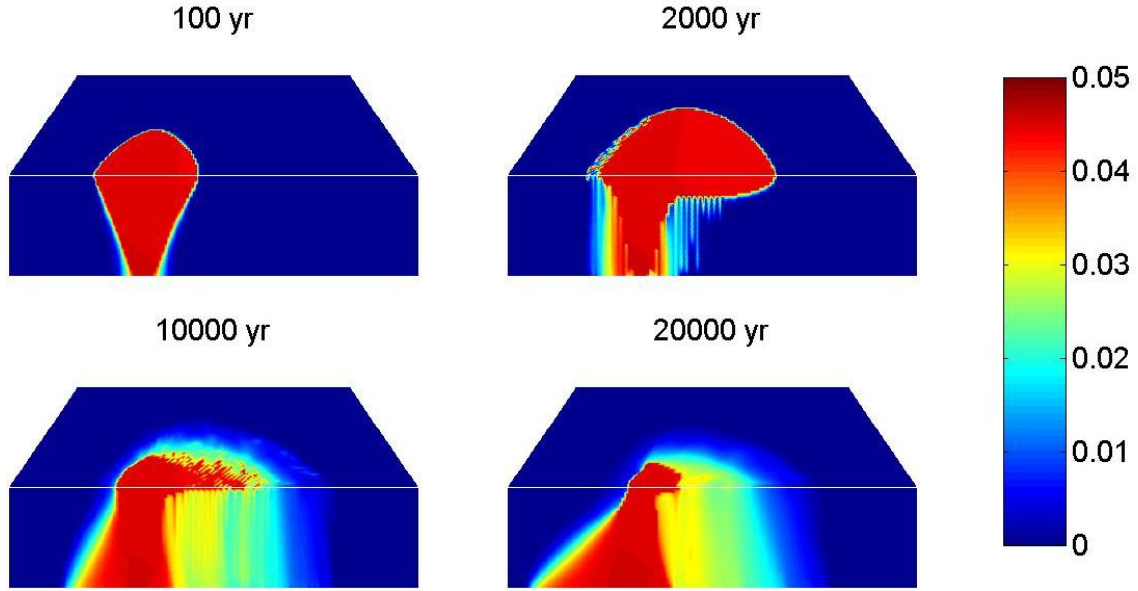


Figure 4.7: Solubility trapping of CO₂. Values shown are molar fraction of dissolved CO₂ in the aqueous phase.

CO₂ moves in the downdip direction, which effectively increases the storage security.

Figure 4.9 shows the distribution of the injected CO₂ over time. The CO₂ in the gas phase is the sum of the CO₂ in the free gas phase and the residually trapped gas. We can see that most of the system dynamics occurs in the first 10,000 years. The CO₂ in the aqueous phase increases as the CO₂ in the free gas phase decreases. The CO₂ in free gas phase approaches zero after approximately 8,000 years.

4.3.3 Coarse-grid results with carbon mineralization

Carbon mineralization entails the fixation of carbon as stable carbonate minerals. To form carbonate minerals, divalent cations (e.g., Ca⁺⁺, Fe⁺⁺) are generally required [46]. These cations can be provided by silicate minerals in the saline aquifer. Although carbonate phases are thermodynamically more favored than silicate minerals (e.g.,

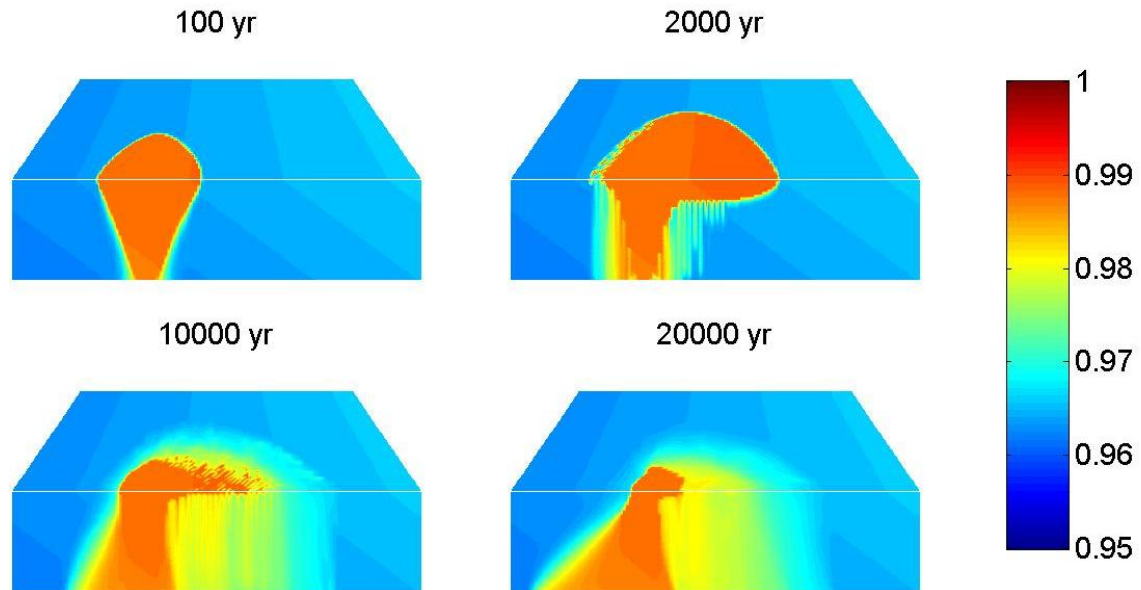


Figure 4.8: Aqueous phase density (g/cm^3) variation with time.

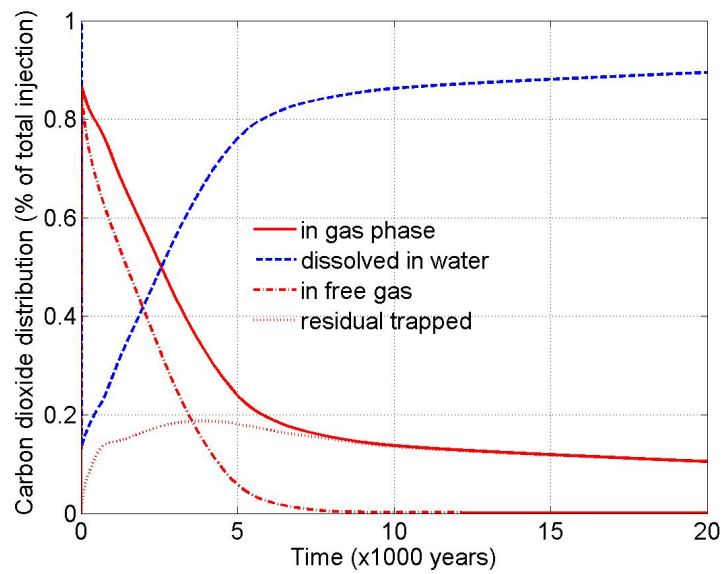


Figure 4.9: Carbon distribution in the fine-grid model of the benchmark study.

anorthite, forsterite), the dissolution of silicate minerals is very slow [20]. Thus the overall mineralization process occurs over very long time scales.

We constructed a coarse-grid model for the benchmark case described earlier. The model contains 30 grid blocks in the x direction, 10 in the y direction, and 5 in the z direction. Because we have mineral kinetic data available for a temperature of 50 °C, we specify this to be the reservoir temperature. The other parameters remain unchanged. The geochemical reactions included in this model are listed in Table 4.6. We consider three equilibrium reactions and three mineral reactions. Overall, the anorthite provides the Ca^{++} , which facilitates calcite precipitation during the CO_2 injection and migration processes. The kinetic data for anorthite, calcite, and kaolinite were given previously in Table 2.4.

Table 4.6: Chemical reactions for CO_2 mineralization in the benchmark study

No.	Reaction
(1)	$\text{CO}_2(\text{aq}) + \text{H}_2\text{O} = \text{H}^+ + \text{HCO}_3^-$
(2)	$\text{CO}_3^{--} + \text{H}^+ = \text{HCO}_3^-$
(3)	$\text{OH}^- + \text{H}^+ = \text{H}_2\text{O}$
(4)	$\text{Anorthite} + 8 \text{H}^+ = 4 \text{H}_2\text{O} + \text{Ca}^{++} + 2 \text{Al}^{+++} + 2 \text{SiO}_2(\text{aq})$
(5)	$\text{Calcite} + \text{H}^+ = \text{Ca}^{++} + \text{HCO}_3^-$
(6)	$\text{Kaolinite} + 6 \text{H}^+ = 5 \text{H}_2\text{O} + 2 \text{Al}^{+++} + 2 \text{SiO}_2(\text{aq})$

We simulate this case for 20,000 years. Figures 4.10 through 4.12 depict the evolution of anorthite, calcite and kaolinite. It is evident that the injection of CO_2 promotes anorthite dissolution. As a result, calcite and kaolinite precipitate.

We also performed a coarse-grid simulation without geochemistry. Figure 4.13(a) shows the evolution of injected CO_2 over time for this model. By comparing Figure 4.9 and Figure 4.13(a), we observe that in the coarse-grid model, the free gas

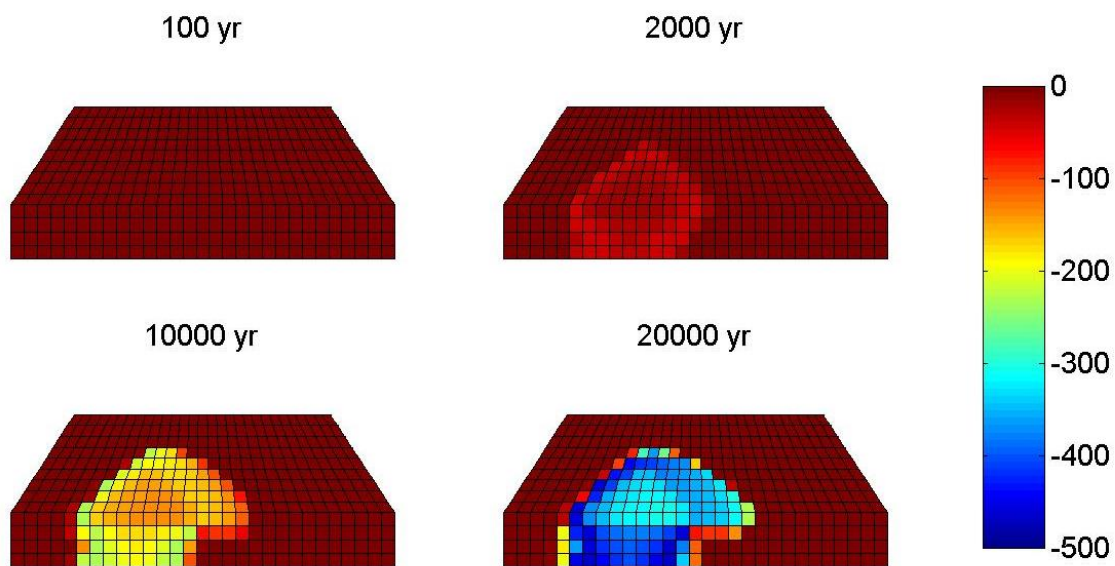


Figure 4.10: Evolution of the molar density change (mol/m^3) of anorthite in the coarse-grid model.

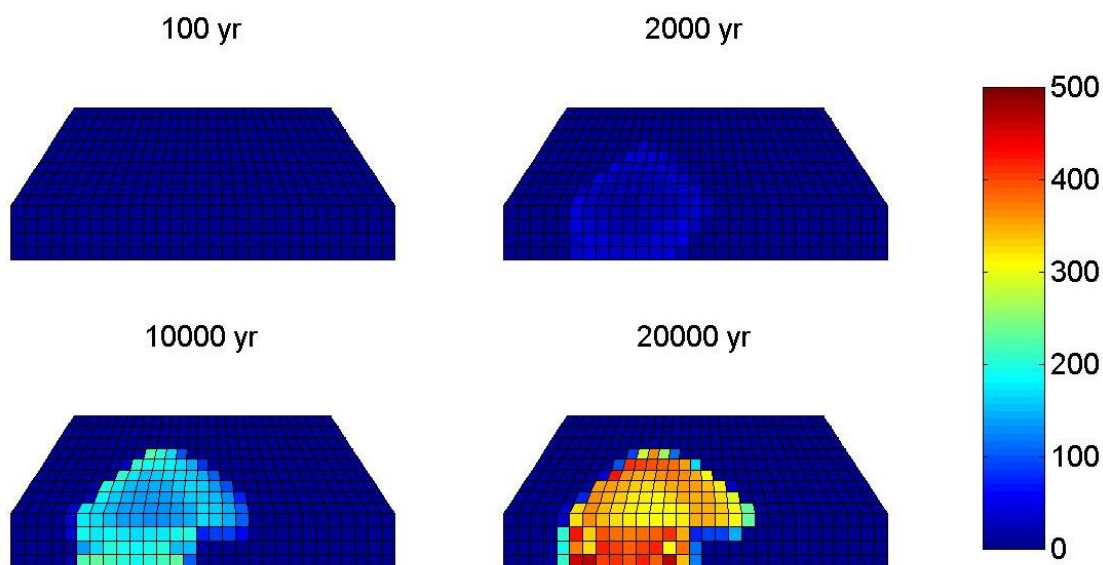


Figure 4.11: Evolution of the molar density change (mol/m^3) for calcite in the coarse-grid model.

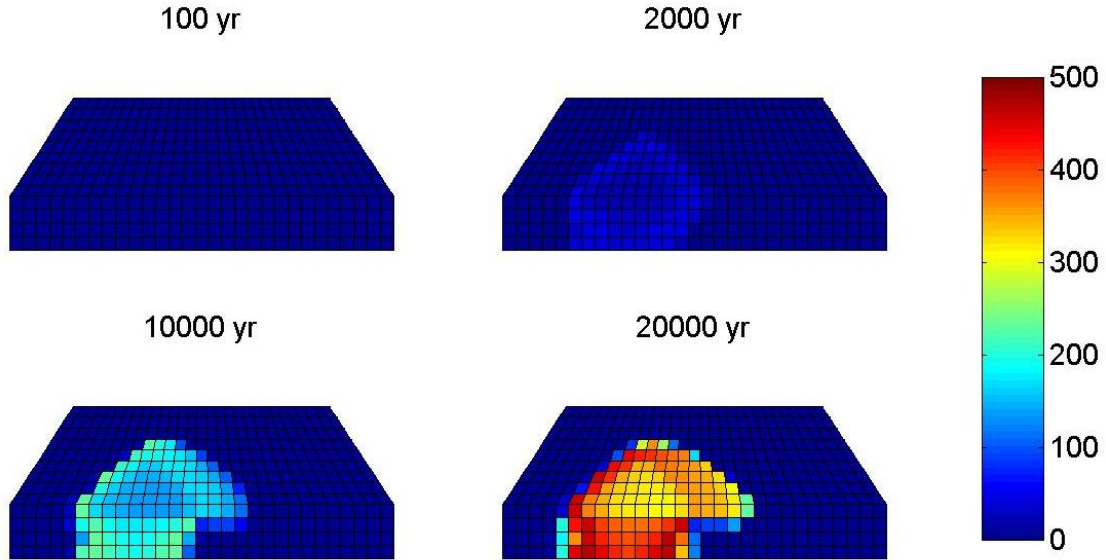


Figure 4.12: Evolution of the molar density change (mol/m^3) for kaolinite in the coarse-grid model.

saturation disappears much later in the coarse model. This is because the fine-grid model captures the gravity fingering evident in Figure 4.7, which expedites the dissolution of CO_2 in the aqueous phase. The coarse-model, however, is not able to capture this convective-driven dissolution.

Figure 4.13(b) shows the carbon distribution with time for the case with geochemical reactions. The free gas saturation is qualitatively similar to that in the case without geochemistry. However, there is much less dissolved CO_2 in Figure 4.13(b) than in Figure 4.13(a) due to mineral carbonization. The residually trapped CO_2 is also consumed by the mineralization process. At the end of 20,000 years, 17% of the CO_2 remains in the gas phase (mostly residually trapped), 23% of the CO_2 remains in the aqueous phase (solubility trapped), and 58% of the CO_2 is stored in mineral form (mineral trapped). These results indicate the potential importance of mineralization in CO_2 storage operations, although extensive fine-grid simulations will be

required to accurately quantify the impact of this mechanism.

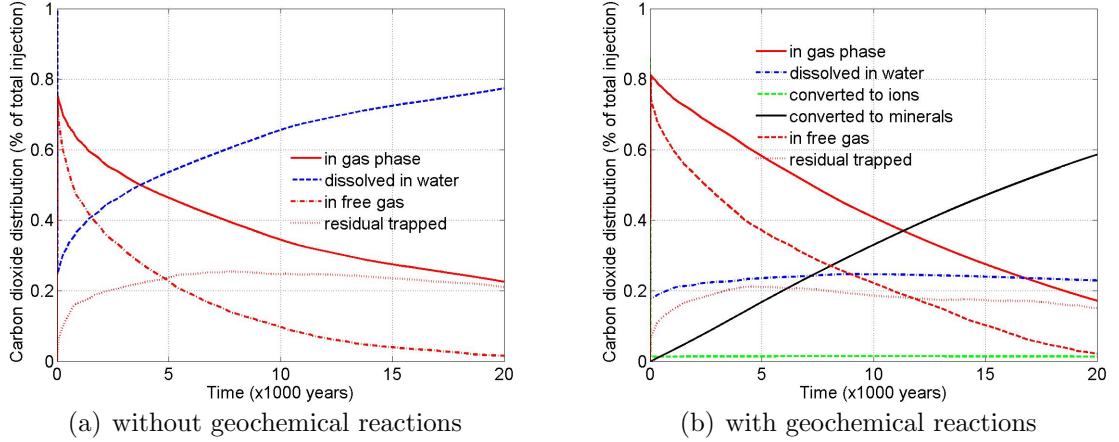


Figure 4.13: Distribution of injected carbon CO_2 over time.

We note that there remain many challenges in the modeling of coupled flow and CO_2 mineralization reactions. First, the mineral kinetic data are subject to significant uncertainty. Under reasonable assumptions, the estimated kinetic rates can vary by six orders of magnitude [20]. Numerical experiments show that the use of high kinetic values are more likely to cause numerical difficulties. In addition, the phase behavior, here determined by an equation of state, does not account for the effects of ions. Therefore, a modified equation of state accounting for ions is required.

Furthermore, numerical difficulties arise when a fine-grid model with geochemistry is simulated. This may be caused by the existence of small molar fractions, as we now illustrate with an example. The equilibrium relation describing the reaction $\text{H}^+ + \text{CO}_3^{--} = \text{HCO}_3^-$ is:

$$\frac{a_3}{a_1 a_2} - Q_q = 0, \quad (4.8)$$

where a denotes activity, Q_q is the equilibrium constant and the subscripts 1 through 3 represent H^+ , CO_3^{--} and HCO_3^- , respectively. Given that $a_i = 55.508\gamma_i X_i/X_w$ (where γ_i , X_i and X_w are activity coefficient, molar fraction for ion i and molar fraction for H_2O in the aqueous phase, respectively), as described in (2.49), the equilibrium relation becomes:

$$\frac{1}{55.508} \left(\frac{\gamma_3}{\gamma_1\gamma_2} \right) \left(\frac{X_3 X_w}{X_1 X_2} \right) - Q_q = 0. \quad (4.9)$$

Equation (4.9) enters as a constraint (secondary) equation for each block. We assume X_1 , X_2 , and X_w are among the primary variables computed from the linear solution at each Newton iteration. A local update is then performed to obtain X_3 . In the blocks where the converged molar fractions of H^+ or CO_3^{--} (X_1 or X_2) are very small (e.g., $O(10^{-15})$), the numerical error in the first term of (4.9) can be significant, as we are at the limit of machine precision. These errors then propagate to other unknowns (X_3) when performing local updates. When the errors become large, the program may cut the time step repeatedly. In fine-grid cases, numerical errors can accumulate rapidly and Newton's method may diverge. We note that these very low molar fractions cannot simply be set to zero as they are required to compute the reaction equilibrium states and kinetic rates.

The coarse-grid model considered in this section represents a typical size of problem for which GPRS shows some degree of robustness. The models with more than a few thousand grid blocks typically give rise to significant numerical difficulties, especially when the simulations are run out to long times (e.g., 1,000 years). A set of techniques is thus required to increase the simulation stability for cases in which the molar fractions of species can vary by many orders of magnitude. One of the

possible solutions is to impose different (nonlinear and linear) convergence criteria for ion species. Currently, the convergence criteria are the same for all species. Another technique entailing variable switching has been reported to be a possible way to increase numerical stability in geochemistry problems [4]. However, this approach will require a systematic treatment and thus will significantly impact the GPRS code.

4.4 Concluding remarks

In this chapter, we described the integration of geochemical modeling capabilities into the GPRS compositional simulation framework. The properties of the CO₂-brine system are determined using an equation of state. Several hysteresis models have been implemented in GPRS, which allows us to model residual trapping of CO₂. For geochemical modeling, we applied the element-based formulation developed in Chapter 2. The properties of ions are calculated by the B-dot model. Geochemical capabilities in GPRS were verified by a case involving eight minerals and 12 reactions. The results from GEM-GHG and GPRS for a one-dimensional example showed very close agreement.

A benchmark problem defined in [14], with some modifications, was used to simulate CO₂ storage. We constructed a fine-grid model and a coarse-grid model for this study. On the fine-grid model, we simulated the CO₂ injection and migration processes for 20,000 years. Chemical reactions were not included in this model. The results showed the distribution of the geologically stored carbon in time. We accounted for mineral trapping in the coarse-grid model. These simulation results showed that mineral trapping can be very significant over long time scales. Future work should be directed toward enhancing the stability and robustness of the geochemical modeling

procedure. This will enable the simulation of fine-grid models that include mineralization reactions.

Chapter 5

Conclusions and Future Work

This thesis developed chemical reaction modeling formulations within the context of a general subsurface flow simulator, GPRS. Applications in the areas of in-situ upgrading and carbon mineralization were also presented. We now summarize this work and offer recommendations for future research directions.

5.1 Summary and conclusions

In Chapter 2, we presented a formulation based on element conservation equations. This formulation treats equilibrium and kinetic reactions, and homogeneous and heterogeneous reactions, in a unified framework. The reaction terms (for both equilibrium and kinetic reactions) do not appear in the conservation equations. The system is then fully described by one additional reaction relation for each chemical reaction. If the reaction is localized (i.e., the reaction is either an equilibrium or a mineral kinetic reaction), then the associated reaction can be decoupled from the full set of equations. As a result, the linear solution time and overall simulation time can be

reduced compared to the formulation in which the reaction relations are included in the set of equations. Note that in both cases flow, reaction and phase behavior are fully coupled and a fully-implicit solution strategy is employed.

We also implemented a species-based formulation and applied it to model in-situ upgrading of oil shale. In the species-based formulation, the elements can be unbalanced. Because the driving force in the in-situ upgrading process is heat injection, the energy equation is also included. Based on available information, we applied GPRS to model Shell's Mahogany Demonstration Project-South. Following tuning of a few uncertain parameters, our results show reasonable agreement with field results. A sensitivity analysis showed that the oil and gas production are highly dependent on the heater temperature. The heater pattern can also affect the production profiles. The ratio of output chemical energy to input thermal energy was found to vary between 6.2 and 6.9 in the cases considered.

In Chapter 4, we modeled CO_2 storage in deep saline aquifers. We constructed two models, a fine-grid model and a coarse-grid model. With the fine-grid model, we presented detailed results for various CO_2 trapping mechanisms, including structural trapping, residual trapping and solubility trapping but not mineral trapping. We then applied the element-based formulation to model the geochemical reactions relevant to CO_2 mineralization. Using available chemistry data, we demonstrated the ability of our formulation to model long-term mineral trapping.

5.2 Recommendations for future work

The following directions should be considered for future work.

- In the element-based formulation, we assume the elements in the chemical reactions are balanced. If some elements are not balanced, extensions are required for the formulation. A mixed formulation in which the species containing unbalanced elements are described by species conservation equations and the remainder are described by the element-based formulation could be investigated.
- The element-based formulation has been implemented and verified with isothermal simulations. The energy equation may also need to be included in some cases. This is not expected to pose significant complications.
- As indicated in Chapter 3, we apply “average” or “effective” porosity and permeability in modeling the in-situ upgrading processes. A more complete geomechanical model is required for modeling the evolution of porosity and permeability during the in-situ upgrading of oil shale or similar processes.
- A complete treatment of heat injection wells is also needed. In our model, we designate the entire heater block as the “heater” and fix the temperature of the block. This approach is, however, approximate and is limited to constant-temperature heaters. A general heater well model is required to simulate both constant-temperature and constant-wattage heaters and to capture transient effects, which may be important in some problems.
- Using available values for CO_2 mineralization reactions, we observe significant numerical difficulty in modeling the reactions involving the disappearance of the aqueous phase and the ions in the aqueous phase. Variable switching could be a useful approach for improving performance. We note that this will require a systematic treatment and will have a significant impact on GPRS code.

- As indicated in Chapter 1, realistic modeling of CO_2 mineralization is not yet possible. This is in part because the required parameters (e.g., reaction rate constants and reactive area of minerals) are generally not accurately quantified. Experiments relevant to CO_2 mineralization should be performed to better quantify the parameters used in numerical modeling. For each mineral dissolution and precipitation reaction, the product of the reaction rate constant and reactive surface area should be measured at temperatures representative of subsurface conditions. In addition, a systematic reaction lumping procedure should be developed, as the computational demands will decrease if fewer reactions are modeled.
- The linear and nonlinear solution strategies used in this work have been developed especially for compositional reservoir simulation without chemical reaction modeling. Thus, a focused research effort on the details of nonlinear coupling of reactions to multiphase flow and transport in heterogeneous formations is necessary in order to model the behavior of large-scale subsurface systems.
- Finally, because the formulations in GPRS can be readily extended to other subsurface reactive flow problems, it will be useful to investigate other processes of interest such as enhanced coalbed methane recovery.

Nomenclature

a	=	activity
\hat{a}	=	ionic size
A_k	=	frequency factor in kinetic reactions
b	=	viscosity coefficient
c	=	viscosity coefficient
c_p	=	rock specific heat capacity, Btu/lb/°F
C	=	concentration, lbmol/ft ³ [mol/m ³]
\mathbf{D}	=	diffusion and dispersion tensor
D	=	depth, ft
Da	=	dimensionless Damköhler number
\mathbf{E}	=	element stoichiometric matrix
E_k	=	activation energy, Btu/lbmol [kJ/mol]
E_{in}	=	thermal energy input, Btu
E_{out}	=	chemical energy output, Btu
f	=	fugacity

F	=	mass or energy balance equation residual
g	=	gravitational acceleration, ft/day ²
H	=	enthalpy, Btu/lbmol [Btu/lb]
I	=	ionic strength
\mathbf{J}	=	Jacobian matrix
k_{rg}	=	drainage gas relative permeability
k_{rgh}	=	imbibition gas relative permeability
k_{rw}	=	drainage water relative permeability
\mathbf{K}	=	permeability tensor, md
K	=	reaction constant
L	=	flux term
m	=	molality, mol/kg H ₂ O
M	=	chemical symbol
N_i	=	total mass of species i
n_c	=	number of fluid and solid components
n_f	=	number of fluid species
n_h	=	number of heater blocks
n_k	=	number of kinetic reactions
n_{kf}	=	number of fluid kinetic reactions
n_{ks}	=	number of mineral kinetic reactions
n_p	=	number of fluid phases
n_q	=	number of equilibrium reactions

n_s	=	number of solid components
p	=	pressure, psi [MPa]
P_c	=	capillary pressure, psi
Q	=	activity or concentration product
q^H	=	energy source term, Btu/day
q^W	=	well source term, ft ³ /day
\mathbf{r}_k	=	kinetic rates vector
\mathbf{r}_q	=	equilibrium rates vector
r	=	reaction rate, lbmol/ft ³ /day
\mathbf{R}	=	reaction term vector
s	=	viscosity coefficient
\mathbf{S}	=	stoichiometric matrix
\mathbf{S}_k	=	kinetic reactions stoichiometric matrix
$\bar{\mathbf{S}}_k$	=	canonical kinetic stoichiometric matrix
\mathbf{S}_q	=	equilibrium reactions stoichiometric matrix
S	=	saturation
S_g^*	=	normalized gas saturation
S_w^*	=	normalized water saturation
S_{wr}	=	irreducible water saturation
t	=	time, day
T	=	temperature, °F[°C, °R]
\mathbf{u}	=	Darcy velocity, ft/day

- U = internal energy, Btu
- V_s = volume shift parameter
- \mathbf{x} = unknown variable set
- X = fluid component molar fraction
- z = ion electrical charge

Greek

- α = thermal diffusivity, ft²/day
- δ = tuning factor for time step control
- γ = activity coefficient
- ϕ = porosity
- η = desired variable change
- κ = thermal conductivity, Btu/ft/day/°F
- μ = viscosity, cp
- ν = stoichiometric coefficient
- ρ = density, lbmol/ft³[lb/ft³]
- σ = activity or concentration
- τ = CPU time
- ω = tuning factor for time step control
- Ψ = binary interaction coefficient

Superscripts

aq = aqueous phase

g = gas phase

n = time step

o = oil phase

W = well

Subscripts

c = variable index

e = element index

h = heater block index

i = fluid component index

j = fluid phase index

k = kinetic reaction index

q = equilibrium reaction index

r = relative permeability

R = rock

s = solid component index

v = unknown variable index

α = target fluid component index

β = target fluid phase index

χ = target solid component index

ς = species index in canonical stoichiometric matrix

ξ = species index in canonical stoichiometric matrix

Constants

k_B = Boltzmann constant, $1.3806503 \times 10^{-23}$ m²kg/s²/K

Bibliography

- [1] A. Assteerawatt, P. Bastian, A. Bielinski, T. Breiting, H. Class, A. Ebigbo, H. Eichel, S. Freiboth, R. Helmig, A. Kopp, J. Niessner, S. O. Ochs, A. Papafotiou, M. Paul, H. Sheta, D. Werner, and U. Ölmann. MUFTE-UG: structure, applications and numerical methods. *Newsletter*, International Groundwater Modeling Centre, Colorado School of Mines, 23(2), 2005.
- [2] P. Audigane, I. Gaus, I. Czernichowski-Lauriol, K. Pruess, and T. Xu. Two-dimensional reactive transport modeling of CO₂ injection in a saline aquifer at the Sleipner site, North Sea. *American Journal of Science*, 307:974–1008, 2007. doi:10.2475/07.2007.02.
- [3] S. Benson and D. R. Cole. CO₂ sequestration in deep sedimentary formations. *Elements*, 4:325–331, October 2008.
- [4] C. M. Bethke. *Geochemical and Biogeochemical Reaction Modeling*. Cambridge University Press, Cambridge, 2008.
- [5] K. Biglarbigi, A. Dammer, J. Cusimano, and H. Mohan. Potential for oil shale in the United States. SPE paper 110590 presented at the SPE Annual Technical Conference and Exhibition, Anaheim, California, 11-14 November, 2007.

- [6] A. Brandt. Converting oil shale to liquid fuels: Energy inputs and greenhouse gas emissions of the Shell in Situ Conversion Process. *Environ. Sci. Technol.*, 42(19):7489–7495, 2008. doi:10.1021/es800531f.
- [7] R. L. Braun and A. K. Burnham. Mathematical model of oil generation, degradation, and expulsion. *Energy & Fuels*, 4:132–146, 1990.
- [8] A. K. Burnham and R. L. Braun. General kinetic model of oil shale pyrolysis. Lawrence Livermore National Laboratory Report UCRL-89805, 1984.
- [9] A. K. Burnham and R. L. Braun. Chemical reaction model for oil and gas generation from type I and type II kerogen. Lawrence Livermore National Laboratory Report UCRL-ID-114143, 1993.
- [10] H. Cao. Development of techniques for general purpose simulators. Ph.D dissertation, Stanford University, Stanford, California, 2002.
- [11] F. M. Carlson. Simulation of relative permeability hysteresis to the non-wetting phase. SPE paper 10157 presented at the SPE Annual Technical Conference and Exhibition, San Antonio, Texas, 5-7 October, 1981.
- [12] H. Class, A. Ebigbo, R. Helmig, H. Dahle, J. Nordbotten, M. Celia, P. Audigane, M. Darcis, J. Ennis-King, Y. Fan, B. Flemisch, S. Gasda, M. Jin, S. Krug, D. Labregere, A. Naderi Beni, R. Pawar, A. Sbai, S. Thomas, L. Trenty, and L. Wei. A benchmark study on problems related to CO₂ storage in geologic formations. *Computational Geoscience*, 13(4):409–434, 2009. doi:10.1007/s10596-009-9146-x.

- [13] P. M. Crawford, K. Biglarbigi, A. R. Dammer, and E. Knaus. Advances of world oil shale technologies. SPE paper 116570 presented at the SPE Annual Technical Conference and Exhibition, Denver, Colorado, 21-24 September, 2008.
- [14] H. K. Dahle, G. T. Eigestad, J. M. Nordbotten, and K. Pruess. A model-oriented benchmark problem for CO₂ storage. http://org.uib.no/cipr/Workshop/2009/CO2/benchmark_definition.pdf, downloaded 20 July, 2009, 2009.
- [15] J. R. Dyni. Geology and resources of some world oil-shale deposits. U.S. Geological Survey Scientific Investigations Report 2005-5294, 2005.
- [16] Y. Fan. Development of CO₂ sequestration modeling capabilities in Stanford General Purpose Research Simulator. M.S. thesis, Department of Energy Resources Engineering, Stanford University, Stanford, California, 2006.
- [17] Y. Fang, G. T. Yeh, and W. D. Burgos. A general paradigm to model reaction-based biogeochemical processes in batch systems. *Water Resources Research*, 39(4):1083, 2003. doi:10.1029/2002WR001694.
- [18] T. D. Fowler and H. J. Vinegar. Oil shale ICP–Colorado field pilots. SPE paper 121164 presented at the SPE Western Regional Meeting, San Jose, California, 24-26 March, 2009.
- [19] S. E. Gasda, J. M. Nordbotten, and M. A. Celia. Vertical equilibrium with sub-scale analytical methods for geological CO₂ sequestration. *Computational Geoscience*, 13(4):469–481, 2009. doi:10.1007/s10596-009-9138-x.

- [20] I. Gaus, P. Audigane, L. Andre, J. Lions, N. Jacquement, P. Durst, I. Czernichowski-Lauriol, and M. Azaroual. Geochemical and solute transport modelling for CO₂ storage, what to expect from it? *International Journal of Greenhouse Gas Control*, 2:605–625, 2008.
- [21] GeoQuest. *Eclipse Technical Description*, Schlumberger Geoquest Manual, 2008.
- [22] H. C. Helgeson, D. H. Kirkham, and G. C. Flowers. Theoretical prediction of the thermodynamic behavior of aqueous electrolytes by high pressures and temperatures; IV, calculation of activity coefficients, osmotic coefficients, and apparent molal and standard and relative partial molal properties to 600 degrees C and 5kb. *American Journal of Science*, 281:1249–1516, 1981.
- [23] IPCC. IPCC special report on carbon dioxide capture and storage, prepared by working group III of the Intergovernmental Panel on Climate Change. Cambridge University Press, Cambridge, United Kingdom, 2005.
- [24] IPCC. Climate Change 2007: Synthesis Report, contribution of working groups I, II and III to the fourth assessment report of the Intergovernmental Panel on Climate Change [core writing team, Pachauri, R. K. and Reisinger, A. (eds.)]. IPCC, Geneva, Switzerland, 2007.
- [25] G. R. Jerauld. General three-phase relative permeability model for Prudhoe Bay. *SPE Reservoir Engineering*, 12(4):255–263, 1997.
- [26] Y. Jiang. Techniques for modeling complex reservoirs and advanced wells. Ph.D dissertation, Stanford University, Stanford, California, 2007.

- [27] A. John, C. Han, M. Delshade, G. A. Pope, and K. Sepehrnoori. A new generation chemical-flooding simulator. *SPE Journal*, 10(2):206–216, 2005.
- [28] J. A. Jossi, L. I. Stiel, and G. Thodos. The viscosity of pure substances in the dense gaseous and liquid phases. *AIChE Journal*, 8(1):59–63, 1962.
- [29] A. Kumar. A simulation study of carbon sequestration in deep saline aquifers. M.S. thesis, Center for Petroleum and Geosystems Engineering, The University of Texas at Austin, 2004.
- [30] L. W. Lake. *Enhanced Oil Recovery*. Prentice Hall, New Jersey, 1989.
- [31] C. S. Land. Calculation of imbibition relative permeability for two- and three-phase flow from rock properties. *SPE Journal*, 8(2):149–156, 1968.
- [32] Y. Le Gallo, L. Trenty, A. Michel, S. Vidal-Gilbert, T. Parra, and L. Jeanin. Long-term flow simulation of CO₂ storage in saline aquifer. Proceedings of GHGT-8, Trondheim, 19-23 June, 2006.
- [33] S. Lee, J. G. Speight, and S. K. Loyalka. *Handbook of Alternative Fuel Technologies*. CRC Press, Boca Raton, 2007.
- [34] P. C. Lichtner. Scaling properties of time-space kinetic mass transport equations and the local equilibrium limit. *American Journal of Science*, 293:257–296, 1993.
- [35] C. M. Mayer, E. O. Frind, and D. W. Blowes. Multicomponent reactive transport modeling in variably saturated media using a generalized formulation for kinetically controlled reactions. *Water Resources Research*, 38(9):1174, 2002. doi:10.1029/2001WR00862.

- [36] Computer Modelling Group. GEM user manual. 2008.
- [37] Computer Modelling Group. STARS user manual. 2008.
- [38] Computer Modelling Group. WinProp user manual. 2008.
- [39] The University of Texas at Austin. UTCHEM-9.0: A three-dimensional chemical flood simulator. Reservoir Engineering Research Program, Center for Petroleum and Geosystems Engineering, Technical Documentation, July, 2000.
- [40] A. Miadonye, B. Singh, and V. R. Puttagunta. Modeling the viscosity-temperature relationship of Alberta bitumen. *Petroleum Science and Technology*, 12(2):335–350, 1994.
- [41] S. Molins, J. Carrera, C. Ayora, and M. W. Saaltink. A formulation for decoupling components in reactive transport problems. *Water Resources Research*, 40, 2004. W10301, doi:10.1029/2003WR002970.
- [42] L. X. Nghiem, P. Sammon, J. Grabenstetter, and H. Ohkuma. Modeling CO₂ storage in aquifers with a fully-coupled geochemical EOS compositional simulator. SPE paper 89474 presented at the SPE/DOE Symposium on Improved Oil Recovery held in Tulsa, Oklahoma, 17-21 April, 2004.
- [43] L. X. Nghiem, P. H. Sammon, B. F. Kohse, and M. Hassam. Modeling CO₂ storage and CO₂ advanced recovery processes. GEM-GHG report by Computer Modelling Group Ltd., 2004.
- [44] J. J. Nitao. Reference manual for the NUFT flow and transport code. Version 2.0, UCRL-MA-130651, 1998.

- [45] R. Nottenburg, K. Rajeshwar, R. Rosenvold, and J. DuBow. Measurement of thermal conductivity of Green River oil shales by a thermal comparator technique. *Fuel*, 57:789–795, 1978.
- [46] E. H. Oelkers, S. R. Gislason, and J. Matter. Mineral carbonation of CO₂. *Elements*, 4:333–337, October 2008.
- [47] Z. Pan, H. Y. Feng, and J. M. Smith. Rates of pyrolysis of Colorado oil shale. *AIChE Journal*, 31(5):721–728, 1984.
- [48] C. A. Passut and R. P. Danner. Correlation of ideal gas enthalpy, heat capacity, and entropy. *Industrial & Engineering Chemistry Process Design and Development*, 11(4):543–546, 1972.
- [49] D. Y. Peng and D. B. Robinson. A new two-constant equation of state. *Ind. Eng. Chem. Fundamen.*, 15(1):59–64, 1976. doi: 10.1021/i160057a01.
- [50] K. E. Peters, C. C. Walters, and J. M. Moldowan. *The Biomarker Guide*. Cambridge University Press, Cambridge, 2005.
- [51] K. S. Pitzer. *Activity Coefficients in Electrolytes Solutions*. Edited by K. S. Pitzer, 2nd ed., CRC Press, 2005.
- [52] K. Pruess, C. Oldenburg, and G. Moridis. TOUGH2 user’s guide, version 2.0. Lawrence Berkeley National Laboratory Report LBNL-43134, November, 1999.
- [53] A. Riaz, M. Hesse, and H. A. Tchelepi. Onset of convection in a gravitationally unstable diffusive boundary layer in porous media. *J. Fluid Mech.*, 548:87–111, 2006. doi:10.1017/S0022112005007494.

- [54] Y. Saad. *Iterative Methods for Sparse Linear Systems*. PWS Publishing, 1996.
- [55] Y. Saad and M. H. Schultz. GMRES: A generalized minimal residual algorithm for solving nonsymmetric linear systems. *SIAM J. Sci. Stat. Comput.*, 7(3):856–869, 1986.
- [56] M.W. Saaltink, F. Batlle, C. Ayora, J. Carrera, and S. Olivella. RETRASO, a code for modeling reactive transport in saturated and unsaturated porous media. *Geologica Acta*, 2:235–251, 2004.
- [57] C. I. Steefel and A. C. Lasaga. A coupled model for transport of multiple chemical species and kinetic precipitation/dissolution reactions with application to reactive flow in single phase hydrothermal systems. *American Journal of Science*, 294:529–592, 1994.
- [58] C. I. Steefel and K. T. B. MacQuarrie. Approaches to modeling reactive transport in porous media, in: *Reactive transport in porous media* (P.C. Lichtner, C.I. Steefel, and E.H. Oelkers, eds.). *Reviews in Mineralogy*, 34:83–125, 1996.
- [59] C. I. Steefel and K. T. B. MacQuarrie. Crunchflow: Software for modeling multicomponent reactive flow and transport. User’s Manual, 2009.
- [60] C. Tebes-Stevens, A. J. Valocchi, J. M. VanBriesen, and B. E. Rittmann. Multicomponent transport with coupled geochemical and microbiological reactions: model description and example simulations. *Journal of Hydrology*, 209:8–26, 1998.

- [61] S. Thibeau, L. X. Nghiem, and H. Ohkuma. A modeling study of the role of selected minerals in enhancing CO₂ mineralization during CO₂ aquifer storage. SPE paper 109739 presented at the SPE Annual Technical Conference and Exhibition, Anaheim, California, 11–14 November, 2007.
- [62] H. Vinegar. Shell’s In-situ Conversion Process. Presented at 26th Oil Shale Symposium, Golden, Colorado, 16-18 October, 2006. <http://www.ceri-mines.org/documents/R05a-HaroldVinegar.pdf>, downloaded 31 October, 2008.
- [63] J. R. Wallis. Incomplete Gaussian elimination as a preconditioning for generalized conjugate gradient acceleration. SPE paper 12265 presented at the 7th SPE Symposium on Reservoir Simulation, San Francisco, California, 15-18 November, 1983.
- [64] S. L. Wellington, I. E. Berchenko, E. P. Rouffignac, T. D. Fowler, R. C. Ryan, G. T. Shahlin, G. L. Stegemeier, H. J. Vinegar, and E. Zhang. In situ thermal processing of an oil shale formation to produce a desired product. US Patent No. 6,880,633, 2005.
- [65] J. Wheeler and M. F. Wheeler. Integrated parallel and accurate reservoir simulator. Technical report, TICAM01-25, CSM, University of Texas at Austin, 2001.
- [66] S. P. White, R. G. Allis, J. Moore, T. Chidsey, C. Morgan, W. Gwynn, and M. Adams. Simulation of reactive transport of injected CO₂ on the Colorado Plateau, Utah, USA. *Chemical Geology*, 217:387–405, 2005.

- [67] T. J. Wolery. EQ3/6 software package for geochemical modeling of aqueous systems: Package overview and installation guide (version 8.0). Lawrence Livermore National Laboratory Report UCRL-MA-110662 PT I, 1992.
- [68] T. Xu, J. A. Apps, and K. Pruess. Reactive geochemical transport simulation to study mineral trapping for CO₂ disposal in deep arenaceous formations. *Journal of Geophysical Research*, 108(B2):2071, 2003. doi:10.1029/2002JB001979.
- [69] T. Xu, J. A. Apps, and K. Pruess. Mineral sequestration of carbon dioxide in a sandstone–shale system. *Chemical Geology*, 217:295–318, 2005.
- [70] T. Xu and K. Pruess. Coupled modeling of non-isothermal multiphase flow, solute transport and reactive chemistry in porous and fractured media: 1. Model development and validation. Lawrence Berkeley National Laboratory Report LBNL-42050, 1998.
- [71] T. Xu, N. Spycher, and K. Pruess. TOUGHREACT user’s guide: A simulation program for non-isothermal multiphase reactive geochemical transport in variably saturated geologic media. Lawrence Berkeley National Laboratory Report LBNL-55460, 2004.
- [72] G. T. Yeh, Y. Fang, J. Sun, Y. Li, M. H. Li, and M. D. Siegel. Numerical modeling of coupled fluid flow and thermal and reactive biogeochemical transport in porous and fractured media. *Computational Geoscience*, 14:147–170, 2010. doi:10.1007/s10596-009-9140-3.